Lawrence Berkeley National Laboratory
Recent Work

Title
DISSOCIATIVE IONIZATION OF LIQUID WATER INDUCED BY VIBRATIONAL OVERTONE EXCITATION

Permalink
https://escholarship.org/uc/item/3g23q1dc

Author
Natzle, W.C.

Publication Date
1983-03-01

eScholarship.org Powered by the California Digital Library
University of California

LBL-15786 c.2

Lawrence Berkeley Laboratory

UNIVERSITY OF CALIFORNIA

Materials & Molecular Research Division

RECEIVED
LAWRENCE
BERKELEY LABORATORY
MAY 17 1983
LIBRARY AND
DOCUMENTS SECTION

DISSOCIATIVE IONIZATION OF LIQUID WATER INDUCED BY VIBRATIONAL OVERTONE EXCITATION

Wesley Charles Natzle
(Ph.D. Thesis)

March 1983

TWO-WEEK LOAN COPY
This is a Library Circulating Copy
which may be borrowed for two weeks.
For a personal retention copy, call
Tech. Info. Division, Ext. 6782.

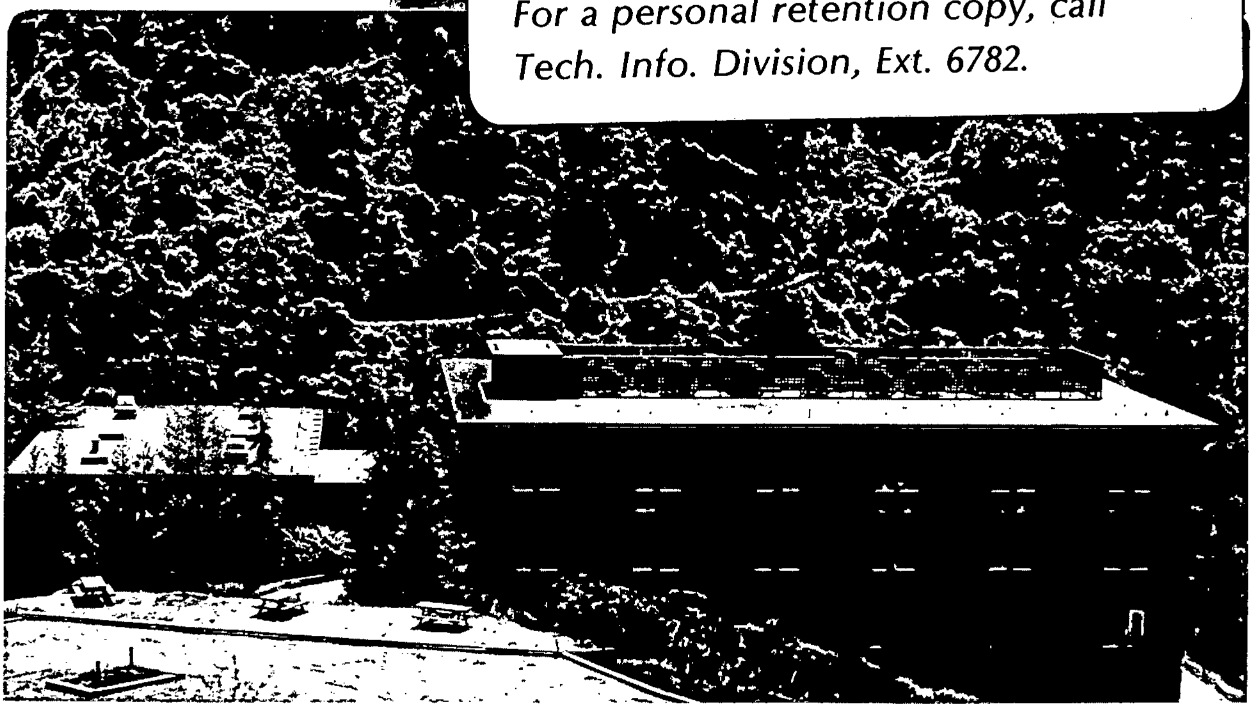

Prepared for the U.S. Department of Energy under Contract DE-AC03-76SF00098

LBL-15786 c.2

DISCLAIMER

This document was prepared as an account of work sponsored by the United States Government. While this document is believed to contain correct information, neither the United States Government nor any agency thereof, nor the Regents of the University of California, nor any of their employees, makes any warranty, express or implied, or assumes any legal responsibility for the accuracy, completeness, or usefulness of any information, apparatus, product, or process disclosed, or represents that its use would not infringe privately owned rights. Reference herein to any specific commercial product, process, or service by its trade name, trademark, manufacturer, or otherwise, does not necessarily constitute or imply its endorsement, recommendation, or favoring by the United States Government or any agency thereof, or the Regents of the University of California. The views and opinions of authors expressed herein do not necessarily state or reflect those of the United States Government or any agency thereof or the Regents of the University of California.

LBL-15786

DISSOCIATIVE IONIZATION OF LIQUID WATER INDUCED BY VIBRATIONAL OVERTONE EXCITATION

Wesley Charles Natzle
(Ph.D. Thesis)

Lawrence Berkeley Laboratory
University of California
Berkeley, California 94720

March 1983

This work was supported by the Director, Office of Energy Research, Office of Basic Energy Sciences, Chemical Sciences Division of the U.S. Department of Energy under Contract Number DE-AC03-76SF00098.

Dissociative Ionization of Liquid Water Induced by Vibrational Overtone Excitation

Wesley Charles Natzle

ABSTRACT

Photochemistry of vibrationally activated ground electronic state liquid water to produce H^+ and OH^- ions has been initiated by pulsed, single-photon excitation of overtone and combination transitions. Transient conductivity measurements were used to determine quantum yields as a function of photon energy, isotopic composition, and temperature. The equilibrium relaxation rate following perturbation by the vibrationally activated reaction was also measured as a function of temperature and isotopic composition.

In H_2O, the quantum yield at 283 ± 1 K varies from 2×10^{-9} to 4×10^{-5} for wave numbers between 7605 and 18140 cm^{-1}. A model is used to characterize the wavelength dependence. The model gives the quantum yield as the probability that photon absorption produces an ion pair times the probability of separation from the ion pair. The result is proportional to the ionic mobility, to the equilibrium constant of the ion pair and excited reactant and to the length of time the reactant remains activated. The quantum yield rises through the low frequency side of an absorption band and is relatively constant through

the band center and high frequency wing. This behavior shows the quantum yield is nearly independent of the physical process that broadens the absorption. The process is either structural differences or combination excitation of lattice motions. The increase in quantum yield with temperature is smaller with higher excitation energy.

In D_2O, the dependence of quantum yield on wavelength has the same qualitative shape as for H_2O, but is shifted to lower quantum yields. The hydrogen mole fraction dependence is not monotonic. The position of a minimum in the quantum yield versus hydrogen mole fraction curve is consistent with a lower quantum yield for excitation of HOD in D_2O than for excitation of D_2O. This behavior can be explained by an unfavorable flow of energy from an excited OH stretch of an HOD when surrounded by D_2O.

The ionic recombination distance of 5.8 ± 0.5 Å is calculated from the equilibrium relaxation rate. It is constant within experimental error with temperature in H_2O and with isotopic composition at 25 ± 1°C. The distance is consistent with recombination in a four-molecule hydrogen bonded linear chain.

C. Bradley Moore

I dedicate this thesis to the nineteenth century
philosopher/economist

John Stuart Mill

A man of genius, strength, and perseverance

ACKNOWLEDGEMENTS

Before writing my acknowledgements, I decided to leaf through the acknowledgements written by some of my predecessors. The authors had two major goals: (1) to thank those who helped with their development as scientists; and (2) to thank people who offered non-scientific support. My goals include these two and add a third--to express a few light-hearted, philosophical thoughts on the writing of acknowledgements.

I can begin to reach the first goal by thanking Brad Moore. The multitude of successful scientists he has advised will testify to his effectiveness. The astute will learn from his example, especially his drive to find and clearly describe the heart of any matter. Several professors, in addition to Brad, were helpful in guiding me to the completion and understanding of my thesis. Professor David Goodall offered considerable help with the water experiments from far off England. Professor Gabor Somorjai helped me understand the purpose of this work. Finally, two professors gave me early guidance and continuing inspiration. Professor Grover Willis gave me a nudge toward chemistry and Professor John Root intensified my interest in kinetics.

My thanks are not complete without mention of Jim Weisshaar. We had a good lab on the "hill" when he was the "senior member" of the hill group. I greatly appreciated our major scientific discussions, but did not fully appreciate the countless small but significant things Jim did to make the hill a fun and efficient place to work. Other group members also need to be included. When I as a beginner was lost or confused, Don Douglas always took time to teach me a thing or two. Andy Kung continues to put up with all of my "what if ..." and "why not ..." questions. The entire past and present Moore group deserves my thanks for enduring countless questions similar to those endured by Andy and for participating in the ensuing discussions.

Although many people have helped me increase my knowledge during graduate school, perhaps the strongest indication that I learned something from them is that I leave with more unanswered questions than when I arrived. I hope that the people I meet in the future will be as able to increase the number of my unanswered questions.

Several people deserve thanks for loans of equipment and supplies. Carol Balfe and the Raymond group provided feedstock water. Howard Gamper provided a Millipore filter holder and filters, and Bill Vance provided septum tops.

The second part of most author's acknowledgements is included because they realize that often the support of greatest importance is non-scientific. My mother and father, Jane and Charles Natzle, my sister, Jeanette, and brother-in-law, Bill Vance, have provided a needed "long term" family base. In addition, Paul Whitmore, Mark Logan, and Erika Schneider as apartment mates and friends have been part of a Berkeley "family". Jackie Denney deserves special thanks for her efforts to extend the family to the research group as well. I have benefited from the friendship and conversation of Joan Frisoli, Alison Abbate, and Linda Young, enjoyed discussion with Chi-Ke Cheng, Hai-Lung Dai, Michael Diegelmann, and Tomoji Kawai. A fresh view of the United States and its relationship to the rest of the world never fails to stimulate thought. A list of people to thank would not be complete without inclusion of some people whose influence is sometimes subtle, often powerful: L. Vasudeva, Le-Ping Cheng, John Stuart Mill, Michael Novak, Karl Jaspers, Kierkegaard, the German Existentialists, J.S., Nietsche, Ayn Rand, Lao-Tzu, Aristotle, and the Berkeley Concert Band gang, especially Reiko Kubota for exercising her eyes and fingers by typing my thesis.

I have tried to follow the example of successful previous graduate students when writing my acknowledgements. Hopefully, I have not left out many people I would like to thank. I am ending my acknowledgements but not my acknowledgement section. I am dissatisfied with what I have just written for two reasons. First, my acknowledgements are not original. After scores of people have worked in the same research group, the emphasis of each acknowledgement is different, but the names are the same. Secondly, I find it difficult to write acknowledgements that accurately express my gratitude. I decided I could remedy the first difficulty by philosophizing about the second. None of my predecessors have considered the problem of writing good acknowledgements. I consider this my only opportunity to write something completely creative and unfettered by the laws of nature or probability.

Some may think this section inappropriate. It is true that my time would have been better spent writing something else, but I think the section _is_ appropriate. Since it is _about_ acknowledgements, I can include it with no disruption of the generally accepted thesis format. No additional sections need be added. Also, since one major goal of the thesis is to help the reader understand what the author has learned, why not include what I have learned about acknowledgements?

Other readers might think the section appropriate, but uninteresting. I risk losing the attention and respect of those not inclined toward philosophy.

Acknowledgements almost write themselves. I began to understand acknowledgements only _after_ they were written. Upon re-reading them, I realized they did not accurately express my feelings. The crux of the problem is that although feelings of gratitude persist, the ideal emphasis is ephemeral. No difficulty is caused by this until it is time to scrutinize and formulate these feelings into a snapshot called the acknowledgement section of a thesis. Then, almost as soon as they are written, the ideal emphasis changes. I did not immediately realize how the difficulty could be resolved. I only knew the acknowledgements I had did not match my vision of "ideal" acknowledgements. I found myself crossing out word after word after word in an earnest, though fruitless, attempt to improve. (One reason to be earnest is when there is only one chance to get it right because the filing date is approaching). The nature of gratitude allows some change, but precludes improvement of my acknowledgements. I realized I was heading toward one of only two possible limits. If I continued on my course, I would end up with no acknowledgements whatsoever. That limit is a possibility, I am sure my committee members could be convinced to sign my thesis (sans acknowledgement) without batting an eye. All the people that read theses could receive all the information they need without reading someone's acknowledgements. On the other hand, there is a certain amount of ridiculousness in removing the acknowledgement of a thesis. I do have gratitude to express even though imperfectly. In spite of my frivolity here, my gratitude is deep and sincere. I must, therefore, grit my teeth as best I can, as long as I can or as long as I need to, and choose the other limit. That limit is to print my acknowledgements as they stand, with no further alteration. A few might find them interesting; at the very least, someone else coming along after me can read them (just as

I read the acknowledgements of my predecessors) and decide what they will keep and what they will throw out when they write their own acknowledgements. Also, I have learned *something* from writing these. I hope someday, after I have aged, I can read this snapshot of my feelings and appreciate the change in my perceptions.

This work was supported by the Director, Office of Energy Research, Office of Basic Energy Sciences, Chemical Sciences Division of the U.S. Department of Energy under Contract Number DE-AC03-76SF00098.

TABLE OF CONTENTS

page

Chapter I. Introduction 1

- I. The Reaction in Perspective 3
  - A. Gas Phase Vibrationally Activated Reactions 3
  - B. Liquid Water Reaction 6
  - References 14

Chapter II. Experimental 16

- I. Introduction to System Operation 16
- II. Liquid System 21
  - A. Components 21
  - B. Assembly 26
    - 1. Cell 26
    - 2. Thermocouple 26
    - 3. Ion Exchange Column 27
    - 4. Interconnection 27
  - C. Cleaning 28
  - D. Liquid System Operation 31
    - 1. Cell Constants 31
    - 2. Feedstock H_2O 32
    - 3. Establishing Proper Conditions 33
    - 4. Isotopically Mixed System 35
      - a. Feedstock D_2O 35
      - b. Column Deuteration 36
      - c. Isotopic Analysis 36

- III. Excitation Sources 40
- IV. Electronics 47
  - A. Conductivity Monitor 49
  - B. Triggered Differential Amplifier 52
  - C. Digitizer 57
  - D. Timing Electronics 58
  - E. Electronics Performance 61
- V. Absorption Spectra 66
- References 70

Chapter III. Analysis 71

- I. Laser Induced Dissociative Ionization Quantum Yields 71
  - A. Concentration of Absorbed Photons 74
    - 1. Concentration of Absorbed Photons from the Conductivity Step 74
    - 2. Concentration of Absorbed Photons from the Absorption Spectra 81
  - B. Concentration of Reactive Events 83
  - C. Conductivity from Signal Voltages 86
- II. Thermal Recombination Rate 89
- III. Discussion of Error 89
  - A. Conductivity-based Quantum Yields 90
  - B. Absorbance-based Quantum Yields 96
- References 98

Chapter IV. Results 100

- I. Laser-induced Reaction 100
- II. Thermal Recombination Reaction 124

References 134

Chapter V. Discussion 135

- I. Thermal Recombination Reaction 135
- II. Laser Reaction 142
  - A. Model-independent Interpretation 145
    - 1. Nature of the Laser-induced Reaction 145
    - 2. Wavelength Dependence of the Quantum Yield in H_2O 147
    - 3. Quantum Yield Temperature Dependence 151
    - 4. Hydrogen Mole Fraction Dependence of the Quantum Yield and the Wavelength Dependence in Nearly Pure D_2O 151
  - B. Quantum Yield Model 157
    - 1. Probability of Ion Pair Separation 158
    - 2. k_{1a}/k_{-1a} 165
    - 3. $1/(k_{1a} + k_2)$ 169
  - C. Application of the Quantum Yield Model to Results 173
    - 1. Quantum Yield vs. Hydrogen Mole Fraction 174
    - 2. Quantum Yield vs. Temperature 195
    - 3. Quantum Yield vs. Photon Energy 202

References 214

Chapter VI. Conclusions 219

I. Thermal Recombination Reaction 219

II. Vibrationally Activated Reaction 219

Appendix A. Independence of Signal with Laser Position and Intensity Profile 222

Appendix B. Quantum Yield Program 226

Appendix C. Recombination Distance Program 237

Appendix D. Non-statistical Effects in Overtone Photochemistry 242

References 245

Appendix E. Further Work 246

References 251

CHAPTER I. INTRODUCTION

A complete understanding of chemical kinetics requires exploration of all possible physical conditions in which reactions occur. One class of reactions particularly resistant to study are the reactions of vibrationally activated species in condensed phase. This is in contrast to gas phase reactions where vibrational activation is commonplace.[1] An arsenal of methods including a pipette and stopwatch, stopped flow, flow tube, equilibrium perturbation, and NMR exist for study of liquid phase reactions of molecules with a Boltzmann distribution of internal energy.[3] However, they are unable to produce vibrational activation. Perhaps the most clearcut example of a vibrationally activated reaction, first described by Goodall and Greenhow[2], is the proton transfer reaction of ground electronic state liquid water induced by single photon overtone absorption

$$H_2O \overset{h\nu}{\rightleftarrows} H_2O^* \rightleftarrows H^+ + OH^-.$$

One other method besides single photon overtone excitation has been used to produce vibrational activation of molecules in liquids. When Franck-Condon factors are favorable, photoexcitation can produce molecules with both electronic and a variable amount of vibrational energy determined by the excitation wavelength. Typically, effects resulting from the vibrational energy of the electronically excited reactant are difficult to observe.

Quantum yields of liquid phase photochemical reactions are independent of excitation wavelength, and therefore of the level of vibrational excitation. A portion of the total product yield is formed during the time the reactant is vibrationally activated. But in most reactions, vibrational relaxation competes so effectively with reaction that the total yield is dominated by reactions originating from the ground vibrational state of the excited electronic level. Thus, any wavelength dependent yield arising from vibrational excitation is swamped by the yield from vibrationally relaxed molecules. Turro et al.[4] recently reviewed a few exceptions (none proton transfer reactions) possessing wavelength dependent organic photochemical yields. But even these examples have problems of interpretation. It is difficult to distinguish a wavelength dependent mechanism involving participation of higher electronic states (S_n or T_n with $n > 1$) from a mechanism caused by vibrational excitation of S_1 or for that matter S_0.

There are several advantages when single photon overtone excitation is used for activation. Since absorption is on the potential energy surface of the ground electronic state, only two reactive processes can occur. They are either the vibrationally activated reaction or additional thermal reaction caused by the temperature jump resulting from photon absorption. These two processes are well separated in time, with the vibrationally activated molecules reacting on a timescale fast compared to relaxation of the thermal equilibrium. There is no possible interference from the reaction of vibrationally relaxed but electronically excited molecules as there is in the organic photochemical reactions described by Turro.[4]

The Goodall and Greenhow[2] experiments were the first to use single photon overtone excitation to vibrationally activate a reaction in either the gas or liquid phase. They excited the v=3 O-H stretch overtone at 9399 cm^{-1}. In a subsequent paper, quantum yields were measured as a function of temperature at four fixed wavelengths.[5] This thesis describes and discusses quantum yields for the liquid water dissociative ionization as a function of temperature, wavelength, and isotopic composition. In addition, thermal recombination rates and distances are given as a function of temperature and isotopic composition.

The introduction will put this work in perspective by relating it first to other gas phase vibrationally activated reactions, and then briefly to previous work on thermal, Boltzmann distribution proton transfer reactions. This work establishes a conceptual framework for description and interpretation of reactions of vibrationally activated species in condensed phase. Unfortunately, disadvantages inherent in the H_2O proton transfer system prevent a quantitative physical interpretation of results. A better experimental system could be amenable to a more quantitative interpretation (see Appendix E).

I. The Reaction in Perspective

A. Gas phase vibrationally activated reactions

Most vibrationally activated gas phase reactions involve chemical activation of isolated molecules.

A statistical (RRKM) theory of dissociation works well for isolated gas phase molecules. The liquid water reaction more closely resembles some gas phase experiments performed to demonstrate non-statistical behavior. An overview of experiments performed will be discussed.

Kineticists find it necessary to explore the limits of applicability of statistical theories. The goal is not simply to demonstrate non-statisticality, but to understand why exceptions occur. Although it is reasonable to expect the occurrance of non-statistical unimolecular reactions,[6] few examples have been demonstrated. Most approaches use some type of non-statistical excitation (chemical or photo-activation) and look at the reaction rate or reaction products either on a timescale short compared to the intramolecular relaxation time (high pressures with rapid quenching rates) or use a system where a non-statistical reaction is expected even at long times (extremely low activation energies). Several approaches were recently reviewed.[7]

The approaches that examine low activation energy processes include one that is technically a bimolecular reaction. It is the addition of fluorine to ethylene[8,9] or allene[10] isolated together in rare gas matrices. These reactions have energy bariers low enough that activation occurs by vibrational excitation in an energy range low enough for nearly harmonic vibrations. There is no intramolecular vibrational relaxation in a harmonic system so a non-statistical distribution of vibrational energy is expected. Quantum yields are observed for excitation of some modes that do not monotonically increase with energy. Unimolecular reactions of matrix isolated species have been considered in a recent review. They show no mode specific behavior.[11]

Another type of low activation energy unimolecular decomposition is dissociation of gas phase van der Waals molecules. The internal energy distribution of the dissociation products is non-statistical.[12,13]

Most demonstrations of non-statistical behavior at high pressures involve chemical activation. The function of the high pressure is to quench all but the initial reactions that occur immediately following excitation, before intramolecular relaxation is complete. One interesting example involves methylene addition to a fluorinated alkene to form a symmetric bicyclopropyl, fluorinated alkane with only one cyclopropyl ring initially activated. At high pressures, decomposition of the initially activated ring predominates with a reduced yield from the symmetric non-activated ring. Other reactions where regions of a large molecule physically separated from the reaction coordinate are chemically activated also show a pressure dependent product distribution indicative of incomplete intramolecular vibrational relaxation interrupted by collisions.[7,15-18]

A few attempts to observe non-statistical gas phase reactions use single photon overtone excitation for activation. Several molecules show RRKM behavior[19] and two, allyl isocyanide[20,21] and t-butylhydroperoxide[22], have experimental behavior interpreted as showing non-statistical effects. The t-butylhydroperoxide reaction is similar to the chemical activation experiments already described in that high pressures make the activation occur near the reactive site of a large molecule. The oscillator strength of the excited overtone transition is assigned to the local mode O-H stretch of the dissociating O-OH. The experimental results are consistent with the presence of a rapid non-statistical dissociation that is not quenched along with a "normal" RRKM reaction that is quenched at high pressures. The allyl isocyanide reaction shows a reaction rate not in agreement with RRKM theory at all pressures tested.

The full potential of activation by single photon overtone absorption to test RRKM theory has not been exploited. (See Appendix D)

B. Liquid Water Reaction

We now return to the liquid water reaction. The liquid structure consists of a kind of "supermolecule" composed of an extensive network of individual hydrogen-bonded water molecules. The overtone spectrum can be understood in a local mode model[23] with absorption strength caused by excitation of motions with a large component of O-H stretch motion of an individual oscillator. Following OH stretch excitation, the ensuing energy relaxation is not confined to a single water molecule, but can spread to hydrogen-bonded neighbors of the "supermolecule". Then there is competition between activation of the reactive precursor (perhaps the four-molecule linear chain proposed for the thermal reaction[24]) and randomization (relaxation) into the rest of the "supermolecule". A purely statistical, RRKM treatment of the entire "supermolecule" does not work. If energy randomization in the "supermolecule" was complete before any product was formed, then no laser induced reaction would be observed.

In several respects, the water reaction is similar to the non-statistical reactions just described. The activation energy is relatively low, being intermediate between typical statistical gas phase unimolecular reactions and non-statistical van der Waals molecule dissociations or bimolecular reactions of matrix-isolated species. Also, as in the high pressure chemical activation experiments, the observed reaction is in competition with "intramolecular" relaxation. The analogy is strongest for the unimolecular reaction of t-butyl hydroperoxide. As in H_2O, activation by excitation of OH stretch overtones is followed by the competition of two processes. In the t-butyl hydroperoxide reaction, activation of the non-statistical O-OH dissociation competes with statistical energy randomization into the entire molecule.

The question remains, "What kind of description will be useful for characterization of the liquid water reaction?" Once again it is instructive to consider analogous gas phase reactions. Several authors have suggested that description of non-statistical gas phase unimolecular reactions will require some combination of RRKM and Slater theories.[25] Slater theory describes the reaction rate when the energy in each mode is defined and does not change with time. This situation will prevail in the limit of weakly coupled modes. In other words, if the quantum state of each mode is adiabatic (does not change during the reaction), Slater theory describes the reaction. The importance of a mode to the rate calculation depends upon its projection on the reaction coordinate; where the reaction coordinate is defined as the lowest energy pathway from reactant to product. If a mode has any projection upon the reaction coordinate, it will be designated an "active" mode. If a molecule has enough vibrational excitation in each active mode to reach the global critical configuration, then the minimum potential energy of a molecule passing from the reactant to the product manifold is the potential energy of the critical configuration. If some modes do not contain enough energy to reach the global critical configuration, then reaction can still occur, but the minimum potential energy is at a local saddle point instead of the critical configuration of the global saddle point. A portion of configuration space which includes the critical configuration of the global saddle point is excluded by the defined quantum state of each mode.

For a statistical RRKM, unimolecular reaction of an isolated molecule, the energy is confined to the excited molecule. Strong mode coupling causes the energy to be rapidly shuttled among the available modes. The number of strongly coupled modes used in an RRKM calculation is equal to the number of modes in the molecule. Since all active modes are strongly coupled, and can take on any energetically allowed quantum state, the minimum potential energy of a reacting molecule is defined by the global saddle point energy minimum in the configuration space of the entire molecule. In other words, all modes of the molecule are strongly coupled, and all active modes are strongly coupled.

To summarize: in RRKM theory, a mode is important if it is strongly coupled to the modes containing vibrational excitation. In Slater theory, a mode is important if it contains vibrational energy and is "active".

One promising conceptual picture for non-statistical gas phase or for a vibrationally activated liquid phase process is provided by first breaking the modes of the system into active and non-active modes, and then once again into modes strongly-coupled and not-strongly-coupled to the modes that are vibrationally excited. The four possible types of mode are shown below.

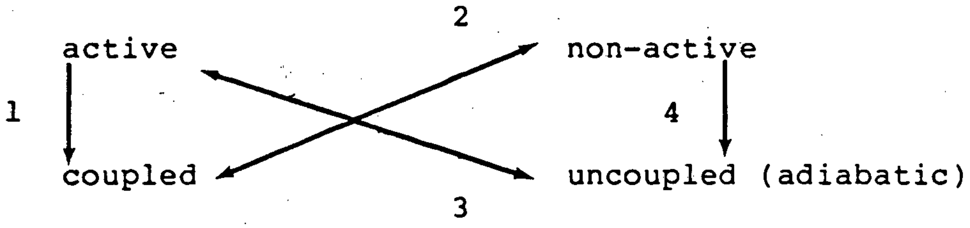

Non-active uncoupled modes (4) can be ignored. The major difference between a statistical unimolecular reaction and the situation described here is that some active modes can be uncoupled (3). Thus, the energy barrier is greater than the global saddle point. A description of the reaction rate by RRKM theory with the number, and frequency of modes determined by whether a mode is strongly coupled, and the energy barrier determined by the number of strongly-coupled, active modes will combine the relevant aspects of both RRKM and Slater theory. Thus reaction rates in condensed phase depend on the details of the energy flow; in other words, it depends on which modes are strongly coupled to excited modes. No general guideline as to the identity of each mode can be provided, but it is expected that a reactive gas phase molecule might show a higher energy barrier and/or smaller number of strongly coupled modes when vibrationally activated in a liquid. Conceivably, if the relaxation path, critical configuration, and energy barrier were known, the reaction rate could be calculated quantitatively. However, there are several problems inherent in the H_2O system which prevent a quantitative calculation of the reaction rate. Vibrational relaxation rates and pathways, and ion pair separation probabilities are not known. Therefore, only quantum yields can be determined, not reaction rates. Also, the identity of the reactive species and of the "active" modes is not known. Appendix E suggests other potential work including some systems where a quantitative treatment may be possible.

The gas phase experiments are performed by measuring product quantum yields as a function of pressure following a C.W. photolysis. Long irradiation times are required. This necessitates use of reactants with an activation energy high enough to prevent interfering dark reaction products.

There are major experimental differences between the gas phase and liquid phase experiments. In a liquid, the combination of low cross section for high overtone excitation and lower quantum yields resulting from rapid intermolecular relaxation makes product detection following a C.W. photolysis in liquids very difficult. Instead, pulsed excitation and transient conductivity measurements are used to generate and detect ionic products. Low activation energy processes can be studied because the presence of thermally generated product does not interfere with measurement of the laser generated transient products.

The liquid water proton transfer reaction is also interesting for several reasons not related to fundamental chemical kinetics. It is important to increase our understanding of liquid water and of proton transfer reactions. Water is the most important solvent in chemistry, and biology. Proton transfer reactions have a similar importance. Acid- and base-catalyzed reactions are important in the synthesis of commercial chemicals, and proton transfers play a role in many biologically important enzyme reactions. The liquid water ionization, being the simplest aqueous proton transfer imaginable is an obvious candidate for study.

The vibrationally activated reaction offers a new way to perturb the $H_2O \leftrightarrows H^+ + OH^-$ equilibrium and potentially offers new information on the reaction and relaxation of the ion pair precursor not obtained in equilibrium relaxation measurements. The recombination of H^+ and OH^- following equilibrium perturbation is diffusion controlled[24], thus no kinetic information is obtained for the recombination of the ion pair by varying the temperature or isotopic composition. The actual ion pair recombination is masked by the diffusion. In contrast, the vibrationally activated reaction is dependent upon both the reaction rate to form the ion pair, the recombination rate, and the diffusion rate. Thus details of reaction, relaxation, and recombination are to some extent unmasked.

The remainder of the thesis describes (A) the experimental apparatus, (B) analysis of data, (C) quantum yield results as a function of temperature, excitation wavelength, and isotopic composition, thermal recombination rates as a function of temperature and isotopic composition, (D) a discussion and qualitative interpretation of the results, and (E) conclusions. Several appendices are included to clarify some points, to add some details, and to stimulate thought.

1. "Unimolecular Reactions", P.J. Robinson and K.A. Holbrook, Wiley, London (1972).
2. D.M. Goodall and R.C. Greenhow, Chem. Phys. Lett. 9, 583 (1971).
3. J.E. Crooks in "Comprehensive Chemical Kinetics", v. 8, C.H. Bamford and C.F.H. Tipper, eds., Elsevier, Amsterdam (1977).
4. N.J. Turro, V. Ramamurthy, W. Cherry, and W. Farneth, Chem. Rev. 78, 125 (1978).
5. B. Knight, D.M. Goodall, and R.C. Greenhow, J. Chem. Soc. Faraday II 75, 841 (1979).
6. S.A. Rice in "Advances in Laser Chemistry", v. 3, A.H. Zewail, ed., Springer-Verlag, Berlin (1978).
7. I. Oref and B.S. Rabinovitch, Acc. Chem. Res. 12, 166 (1979).
8. H. Frei, L. Fredin, and G.C. Pimentel, J. Chem. Phys. 74, 397 (1981).
9. H. Frei and G.C. Pimentel, J. Chem. Phys. 78, to be published (1983).
10. A.K. Knudsen and G.C. Pimentel, submitted to J. Chem. Phys.
11. M. Poliakoff and J.J. Turner in "Chemical and Biochemical Applications of Lasers", v. V, C.B. Moore, ed., Academic Press, New York (1980).
12. D.H. Levy, L. Wharton, and R.E. Smalley in "Chemical and Biochemical Applications of Lasers", v. 2, Academic Press, New York (1977).

13. D.H. Levy, L. Wharton, and R.E. Smalley, Acc. Chem. Res. 10, 139 (1977).

14. J.D. Rynbrandt and B.S. Rabinovitch, J. Phys. Chem. 75, 2164 (1971).

15. A.-N. Ko and B.S. Rabinovitch, Chem. Phys. 30, 361 (1978).

16. J.F. Meagher, K.-J. Chao, J.R. Barker, and B.S. Rabinovitch, J. Phys. Chem. 78, 2535 (1974).

17. F.C. Wolters, B.S. Rabinovitch, and A.-N. Ko, Chem. Phys. 49, 65 (1980)

18. A.B. Trenwith, B.S. Rabinovitch, and F.C. Wolters, J. Chem. Phys. 76, 1586 (1982).

19. J.M. Jasinski, J.K. Frisoli, and C.B. Moore, Discuss. Faraday Soc., submitted.

20. K.V. Reddy and M.J. Berry, Chem. Phys. Lett. 66, 223 (1979).

21 K.V. Reddy and M.J. Berry, Faraday Discuss. Chem. Soc. 67, 188 (1979).

22. D.W. Chandler, W.E. Farneth, and R.N. Zare, J. Chem. Phys. 77, 4447 (1982).

23. A.C. Tam and C.K.N. Patel, App. Opt. 18, 3348 (1979).

24. M. Eigen and L. DeMaeyer, Proc. Roy Soc. (London), Ser. A 247, 505 (1958).

25. R.D. Levine, Adv. Chem. Phys. 47, part 1, 239 (1981).

CHAPTER II. EXPERIMENTAL

The experimental goal is to measure the transient conductivity of a sample of pure water following laser excitation of O-H stretch overtones. The experimental apparatus consists of (1) a liquid system used to contain transport, purify and monitor the water, (2) an optical excitation source, and (3) electronics used to monitor and record the time dependent conductivity. A Cary 14 spectrometer is used to record absorption spectra. This section gives an introduction to the operation of the apparatus, then gives the details of the three subsystems.

I. Introduction to System Operation

The water conductivity is measured by a cell in the H_2O system along with the triggered differential amplifier, low pass filter, digitizer and averager shown in Figure II-1. The differential amplifier and digitizer are triggered by a pulse generator. After a short delay, a Raman-shifted laser source is triggered. The generated light excites overtones of the water flowing between electrodes of the conductivity cell. Product ions give a transient conductivity recorded by a signal averager. The H_2O system removes impurity ions by continuously circulating the water in a closed loop

Figure II-1

Transient conductivity changes induced by dissociative ionization of water are produced and measured with this apparatus.

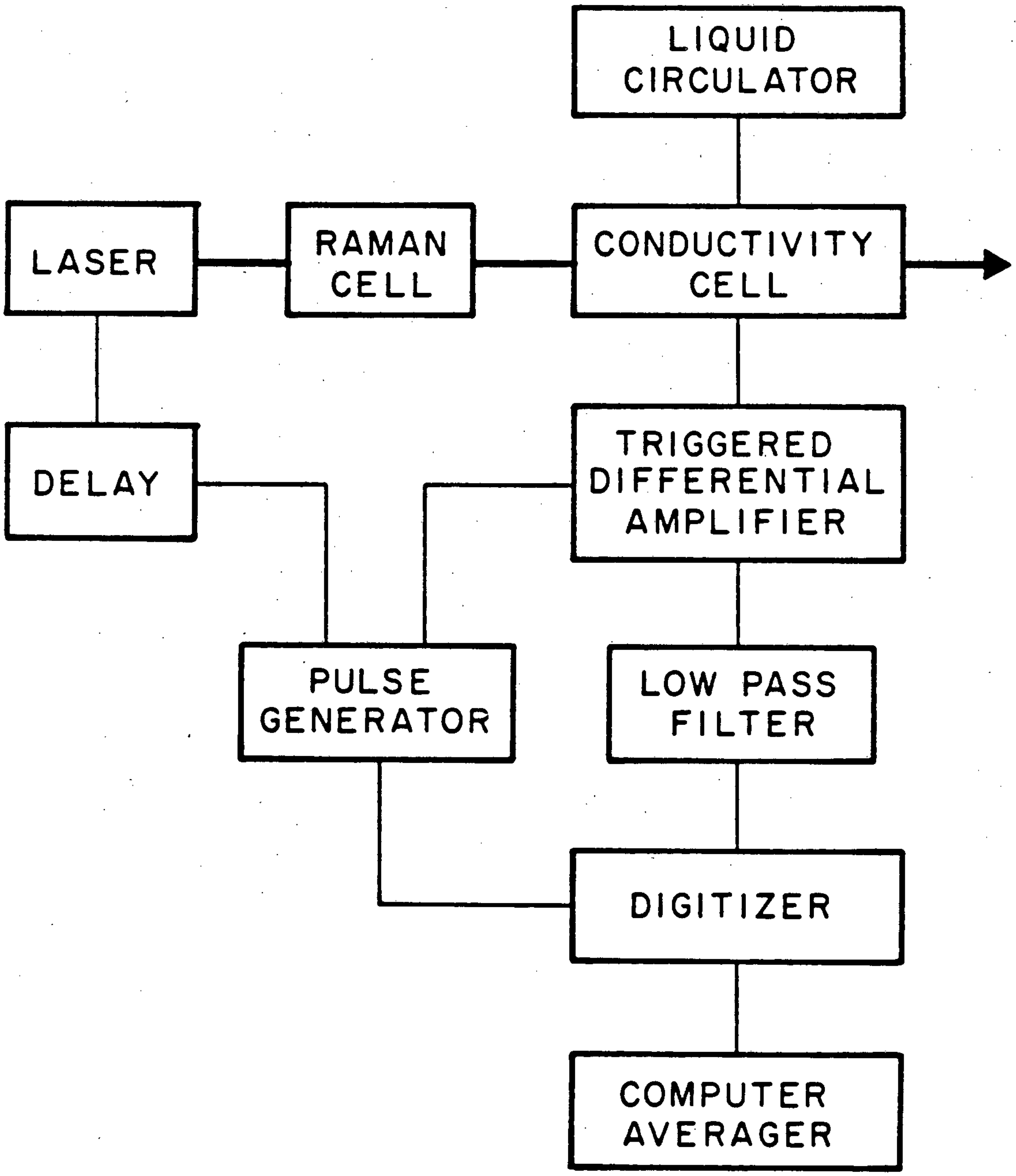
LIQUID CIRCULATOR
LASER
RAMAN CELL
CONDUCTIVITY CELL
DELAY
TRIGGERED DIFFERENTIAL AMPLIFIER
PULSE GENERATOR
LOW PASS FILTER
DIGITIZER
COMPUTER AVERAGER

XBL 8212-12403

Figure II-2

Schematic diagram of the water system.

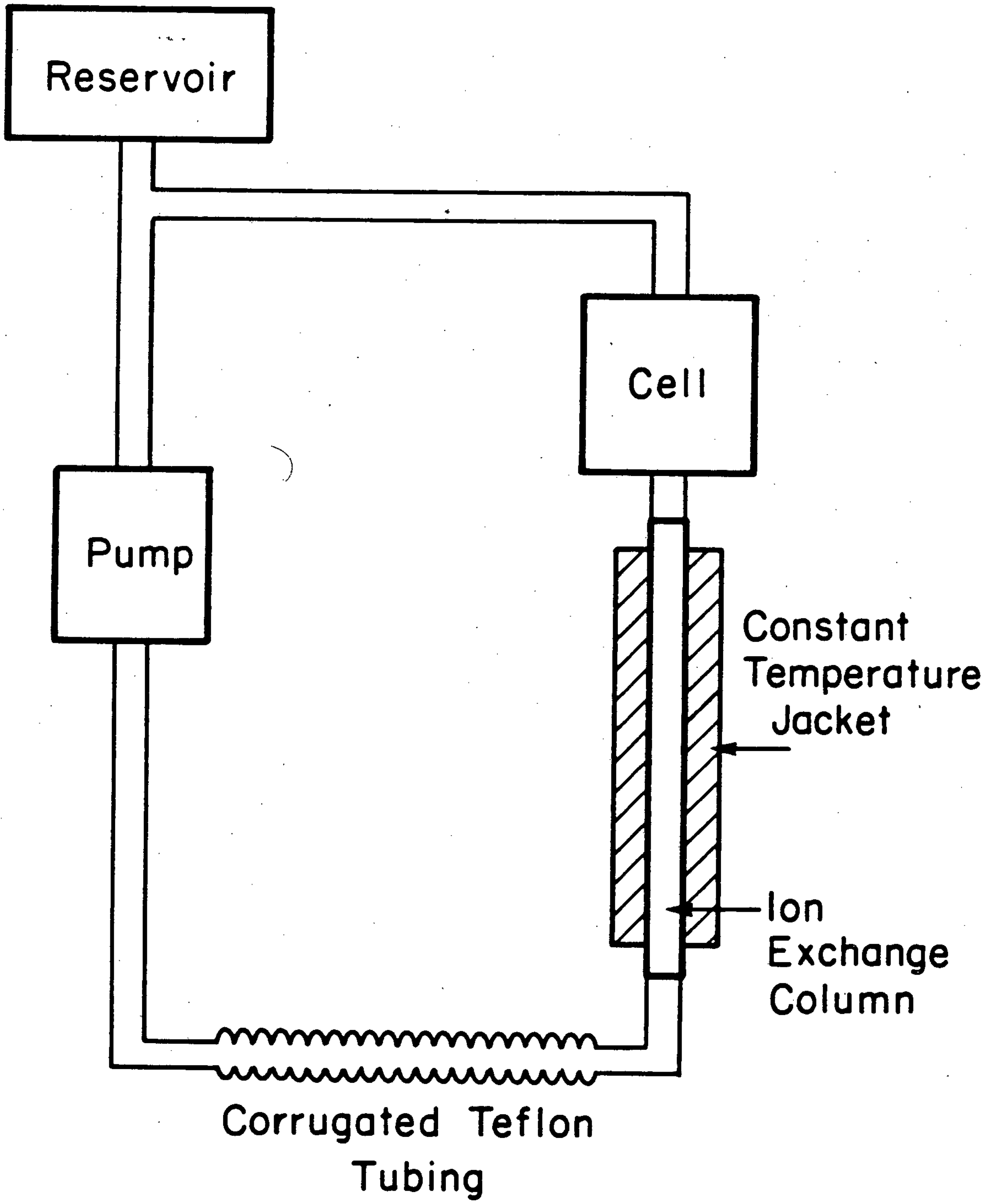
Reservoir
Cell
Pump
Constant Temperature Jacket
Ion Exchange Column
Corrugated Teflon Tubing

XBL 831-7706

through an ion exchange column immediately preceding the conductivity cell.

II. Liquid system

This section describes the components, the assembly, the cleaning, and the operation of the water system, Figure II-2, containing H_2O, D_2O, or isotopic mixtures.

The best closed loop circulation system was constructed of quartz, Pyrex, FEP Teflon, PTFE Teflon, and silicone rubber. Other trial systems will be mentioned.

A. Components

The components of the H_2O system consist of a water reservoir, a pump, an ion exchange column with constant temperature jacket, a thermocouple, and a conductivity cell.

A 225 ml Pyrex bulb is used as a water reservoir during system fill and evacuation/degassing. It supplies a Cole Palmer Masterflex pump. The pump uses a model 7545-00 drive unit with a 7017 peristaltic pump head using 6411-47 silicone tubing. The tubing is 0.25" inside diameter (ID) and 0.379" outside diameter (OD). An 18 cm piece of 1/4" SGA Scientific #R8428-14 corrugated, flexible teflon tubing is connectd to the pump outlet. The ion exchange column is a 78 cm length of 8 mm OD, 7 mm ID, TFE Elastofluor tubing partially filled with Rohm & Haas Amberlite MB-1 mixed bed ion exchange resin. Column supports are made of 0.21 mm mesh Teflon Spectramesh grid #146464 from Spectrum Medical Industries. The grid is stretched over a few millimeters-length of polytetrafluoroethylene, PTFE tubing and then inserted in the column. Larger diameter Vycor glass and polyethylene columns with glass wool column supports were tested with satisfactory results. The ion exchange column is jacketed with a concentric 1-1/8" diameter copper tube. Brass end caps with Viton O-rings seal the copper jacket to the teflon ion exchange column. The water temperature is adjusted by circulating methanol in the jacket. The methanol is pumped with a Lauda model K-4/R temperature controller by Brinkmann Instruments. The absolute water temperature is measured with a copper-constantan thermocouple with a water-ice reference.

The conductivity cell shown in Figure II-3 is machined from a 1/2" x 1-3/4" x 6" teflon block with a chamber 1/2" x 4". Inner walls are smooth and edges perpendicular to the flow are rounded to minimize water turbulence. The bare platinum electrodes are made of 0.051" diameter platinum wire bent and flattened into a staple with 2.7 mm x 9 mm electrode faces. Electrode pairs are located 2-1/2" and 3" downstream from the cell inlet to allow inlet turbulence to damp before reaching the electrodes. Quartz windows 1/8" or 1/16" x 1" x 6" are sealed with Viton O-rings. A 1/16" rubber pad is sandwiched between

Figure II-3

Scale drawing of conductivity cell and electrodes. A 6" x 1-3/4" x 1/8" stainless steel plate with a 1-3/4" x 1/2" opening facing the electrodes screws into the cell body and forces a window against the O-ring. The plate and window are not shown.

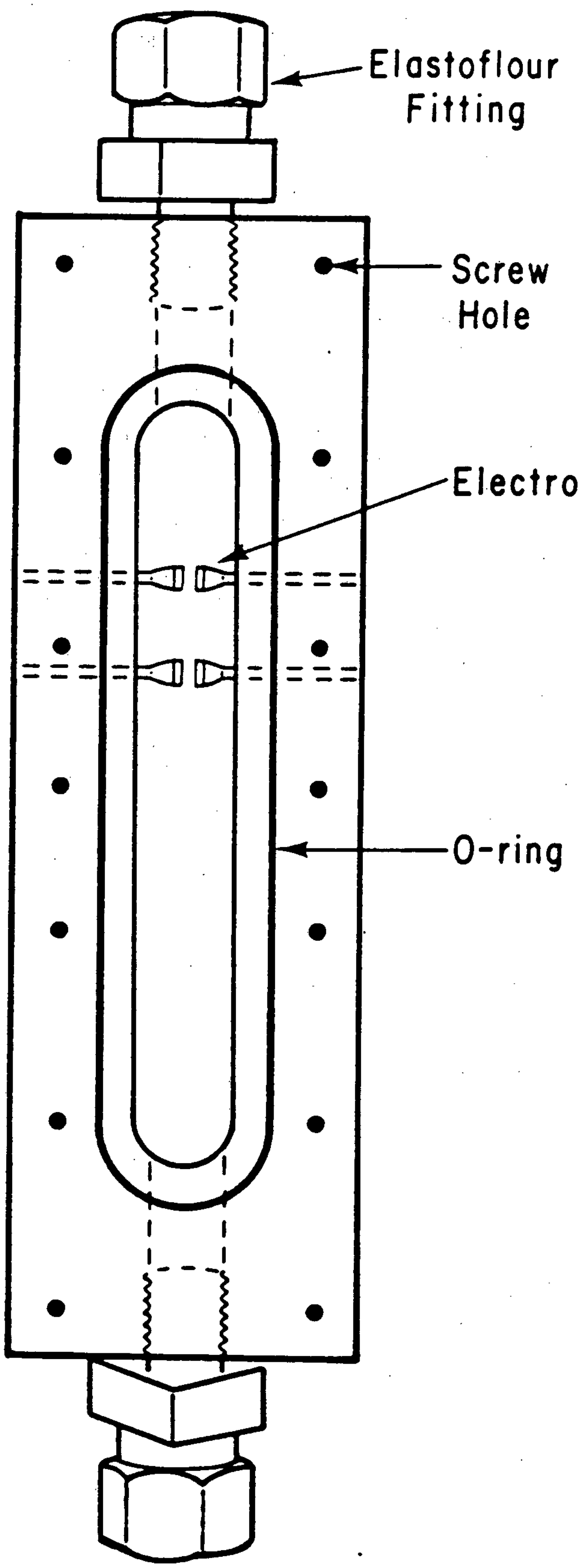
Elastoflour Fitting
Screw Hole
Electrodes
O-ring

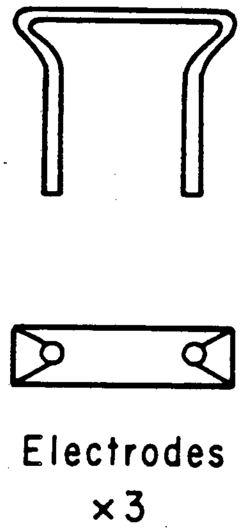
Electrodes
×3

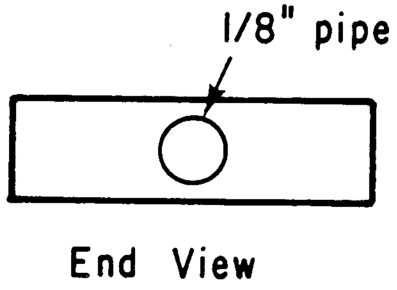
1/8" pipe
End View

XBL 8212-12402

the window and a 1/8" x 6" x 1-3/4" stainless steel retaining plate which screws into the teflon cell.

Several other cells were used for some H_2O quantum yield measurements. A teflon cell with epoxied quartz windows and epoxied platinum staple electrodes was used for measurements taken with a CMX-4 dye laser pumped optical parametric oscillator. Also, two laminar fluid flow cells were used with a Quanta Ray Nd^{+3}:YAG pumped dye laser system. One was made of 3 x 9 mm rectangular cross section quartz tubing with platinum foil electrodes epoxied to ground quartz inserts. Long times were required to desorb ions from ground glass surfaces of the quartz inserts after exposure to KCl conductivity solutions used to determine cell constants. Another cell was made from quartz strips epoxied to form a rectangular channel 1 mm x 2 mm x 300 mm. Electrodes were produced by laminating 9 mm x 14 mm strips of 0.001" platinum foil to the inner wall of the rectangular cell with FEP teflon film. The electrodes were located 25 cm from the cell inlet so that turbulence created at the cell inlet is damped before reaching the electrodes. Torr-Seal epoxy from Varian was selected for its low interaction with H_2O. This cell was discarded after delamination of an electrode. Platinum electrodes vacuum deposited directly on quartz disintegrated on contact with water. However, platinum can be vacuum deposited over an underlayer of titanium or niobium about 200 μm in thickness[1]. Metal oxides, Bi_2O_3 and PbO, have been used for some applications requiring transparent electrodes[2].

B. Assembly

System assembly is done in two parts. First, the cell, thermocouple, and ion exchange column were assembled. Then, the components are interconnected primarily with 8 mm Elastofluor fittings and PTFE tubing.

1. Cell

Electrical connection must be made to the electrodes before attaching them to the cell body. Copper wire is soldered into holes concentrically drilled in the base of the electrode arms. Then the arms are gripped with pliers and forced into undersize holes drilled in the teflon cell. Aluminum foil is used to protect the arms during insertion. A uniform interelectrode distance of 2 mm is obtained by using two removable glass microscope slides as spacers.

2. Thermocouple

The thermocouple is encased in a sealed 4 mm OD Pyrex tube pressure fitted within a concentric 3.5 cm length of 8 mm OD teflon rod. The rod mounts in an Elastofluor fitting. The immersed length is adjusted to about 6.5 cm.

The thermocouple tip lies 7.8 cm downstream from the final electrode pair of the conductivity cell.

3. Ion exchange column

Rohm and Haas Amberlite MB-1 mixed bed resin is used in the ion exchange column. Trace amounts of amine and styrene decomposition products are leached from the resin by soaking in high purity water for several days. Ten to fourteen ml of resin are poured into the column in several small portions to minimize separation of cationic and anionic forms of the resin caused by a higher settling rate for the denser cationic form. A larger resin volume does not significantly improve the ionic purity of the H_2O and will impart trace amounts of organic impurities at a higher rate. Higher pressures at the output of the pump decreases silicone tubing lifetime. Bio Rad AG501-X8 ion exchange resin columns were not used because they produced H_2O with twice the conductivity of the column described.

4. Interconnection

Elastofluor fittings can not be used to connect the silicone pump tubing or the fluorinated ethylene-propylene, FEP, Teflon corrugated tubing to the Elastofluor PTFE tubing. The silicone tubing is simply slipped over and clamped onto the Elastofluor tubing with metal tubing clamps.

The FEP tubing is attached as shown in Figure II-4. The smooth ends of the FEP tubing and the Elastofluor tubing are slipped over a snug-fitting 7 mm OD, 3.2 cm length of PTFE tubing insert. The assembly is covered with an FEP sleeve under PTFE heat shrink tubing, SGA catalog No. R8428-5, and is heated with a heat gun above the approximate 270°C melting point of the FEP sleeve. The FEP Teflon melts forming a strong bond to the PTFE tubing. Care must be taken not to heat the portion of the FEP corrugated tube beyond the PTFE insert.

C. Cleaning

The Teflon, quartz, Pyrex, and silicone rubber parts of the system must be cleaned to prevent contamination of the high purity circulating water.

The Teflon cell body, Elastofluor fittings, and Spectramesh column supports were cleaned by soaking in aqua regia and then rinsing in water for about 5 hours. The PTFE tubing and flexible FEP tubing were assembled with the clean Elastofluor fittings and filled with concentrated nitric acid for about 5 hours. The system was then rinsed and filled with water for 4 hours. Quartz windows were cleaned with methanol then soaked in an aqueous 2% sodium hydroxide, 1% sodium EDTA solution to remove adsorbed ions. The Pyrex water reservoir and

Figure II-4

Attachment of FEP corrugated tubing, A, to Elastofluor PTFE tubing, B, is shown. The corrugated tube must be slipped on the PTFE insert, C. Then the heat shrink tubing, E, and FEP sleeve, D, are heated to seal the FEP.

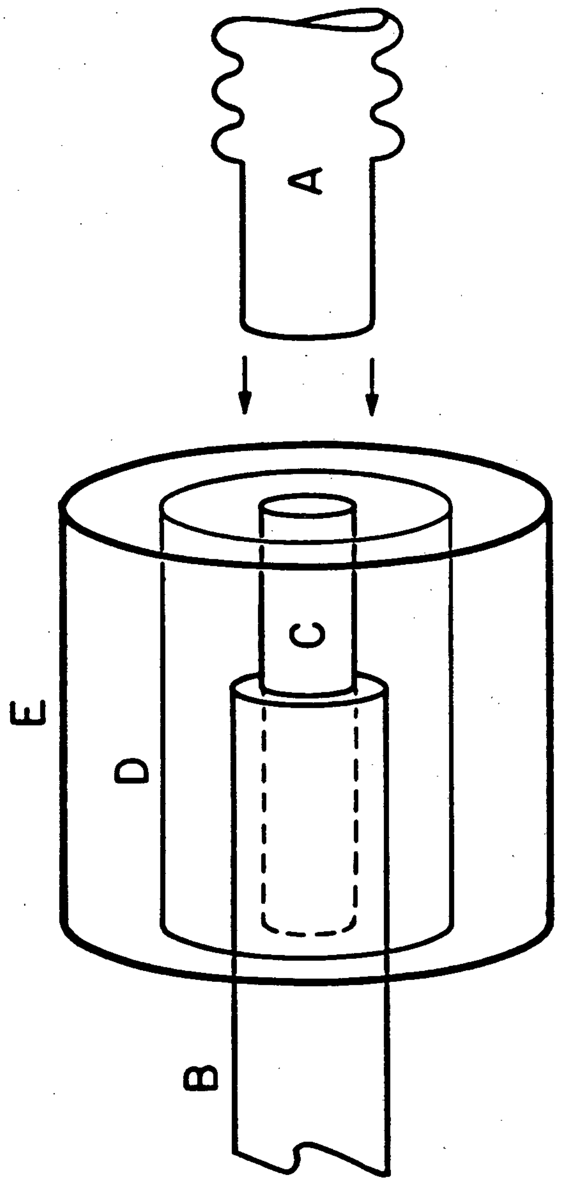
A
C
E
D
B

thermocouple well are boiled for several minutes in dilute nitric acid.

Electrodes were cleaned before assembly by immersion in 1 part nitric acid to 3 parts hydrochloric acid followed by passage of 1 amp of current for two minutes through the positively charged electrode. A platinum wire served as the negative electrode. Silicone tubing for the peristaltic pump was cleaned by rinsing with methanol followed by immersion in boiling water which is allowed to cool to room temperature.

Preferred materials and cleaning procedures for high-purity systems are discussed in reference (3).

D. Liquid system operation

Operation of the liquid system with H_2O includes the following steps: (1) cell constant determination, (2) preparation of feedstock water, and (3) establishing the proper temperature, purity and flow in the circulating water. System preparation and isotopic analysis with H_2O/D_2O mixtures will also be described.

1. Cell constants

Cell constants for both electrode pairs were determined by measuring the resistance of a 10^{-2} molar KCl solution with an A.C. Wheatstone bridge. The cell is immersed in a constant temperature bath of known temperature and allowed to equilibrate. The cell capacitance and resistance is determined by bridge balance. The cell constant, k, was found by the equation

$$k = KR$$

where R is the cell resistance and K is the conductivity of 10^{-2} molar KCl[4], 1.413×10^{-3} $[1 - 1.981 \times 10^{-2}(25 - T)]$ $\text{ohm}^{-1}\ \text{cm}^{-1}$. The cell constant is $0.319 \pm 0.15\ \text{cm}^{-1}$ for both electrode pairs. The cell must be rinsed, then filled with pure H_2O for a day or more following cell constant determination to remove contaminating potassium and chloride ions.

2. Feedstock H_2O

Feedstock water for the circulating water system came from two sources. One source was a Pyrex and quartz pyrolytic still where the water vapor is passed in an oxygen atmosphere through a 900°C quartz tube pyrolyzer. Trace organic impurities are oxidized to CO_2 and H_2O during passage through the pyrolyzer. The condensed H_2O is then redistilled in a second stage and stored. An oxygen purge prevents atmospheric CO_2 from reaching the water. In the second source, water was prefiltered in Barnstead charcoal and ion exchange resin filters, then distilled in a Corning Mega-Pure still. No difference in conductivity is noticed using water from either source.

3. Establishing proper conditions

Water is introduced to the system by filling the expansion bulb. Dissolved CO_2 and many air bubbles must be removed after pouring an ion exchange column and filling the sytem with H_2O. Evacuation of the system using a dry ice/acetone trapped mechanical pump causes the water to boil. Vertical orientation of the ion exchange column eliminates trapping of rising gas bubbles. Several evacuation/repressurization cycles while circulating the water are needed to remove dissolved atmospheric gasses.

The system is repressurized with argon to exclude atmospheric CO_2 from the system. The peristaltic pump circulates the water by squeezing flexible silicone tubing with moving rollers. The flow rate of about 2.5 ml/sec corresponds to about 60 pump revolutions/min or 180 pressure pulses/min. Flow rate changes caused by the pressure variation at the outlet of the pump can produce turbulence in the conductivity cell contributing to low frequency noise in the conductivity signal. These variations are minimized by impeding the fluid flow at the conductivity cell inlet and allowing the system volume between the pump and the flow restriction to expand and contract in response to pressure pulses from the pump. An 18 cm section of corrugated FEP teflon tubing and to some extent, the flexibility of the silicone pump tubing allow system expansion. The flow restriction is provided by the ion exchange column.

An alternate technique is to allow the system to expand and contract into a chamber partially filled with a bubble of compressed gas. This method is undesireable because dissolved gas comes out of solution as the pressure is reduced in the ion exchange column and conductivity cell. Bubbles forming or passing near the conductivity cell electrodes produce spurious signals. Water temperature was varied from 50°C to about -0.1°C for supercooled H_2O. The stability is ± 0.2°C over 2 minutes. At 8.5°C, the water cools a maximum 0.2°C while traveling from conductivity cell to thermocouple. The overall error in the absolute temperature measurement is ± 0.4°C. Most tubing, the ion exchange column, and the conductivity cell are insulated with foam rubber or Armstrong Armaflex.

Four systems were used to maintain the purity of circulating H_2O when measuring the wavelength dependence of the quantum yield: (1) an ion exchange column, (2) an ion exchange column plus a 1.2 μm and 0.47 μm Millipore filter, (3) an activated charcoal column with an ion exchange column plus both Millipore filters, and (4) an ion exchange column plus a 100 watt Hanovia Hg lamp immersion well[5] plus both Millipore filters. A GC/MS of water which was photolyzed longer than 1.5 hours in system (4) showed no detectable organic impurities or less than 5 ppm by weight. The quantum yields measured with each system agreed within experimental error. The simplest system, an ion exchange column, was used with H_2O/D_2O mixtures and for temperature dependent studies in H_2O.

The conductivity of the system ranges between 102% to 200% of the conductivity caused by the equilibrium concentration of hydroxide and hydronium ions (5.5×10^{-8} ohm^{-1} cm^{-1} at 25°C). The poorest conductivities were with the quartz cell with ground glass inserts. The all Teflon system typically gives a conductivity 110% of theoretical.

4. Isotopically mixed system

The isotopically mixed system is nearly identical to the H_2O system with the following exceptions. Feedstock D_2O must be prepared, an ion exchange column deuterated, and isotopic composition of the system analyzed.

4a. Feedstock D_2O

Feedstock 99.8% D_2O (Bio-Rad catalog no. 710-1003 or Aldrich catalog no. 15,188-2) was pyrolytically distilled. The still was pre-deuterated by distilling and then discarding about 10 ml of D_2O while heating all normally cool regions of the still with a heat gun. After cooling, 200-300 ml of D_2O was added to the still and collected after the first stage of distillation.

4b. Column deuteration

A deuterated ion exchange column was obtained by preparing the column with H_2O, followed by three successive cycles of draining, filling, and mixing with high purity D_2O. Mixing is accomplished by degassing the system at least six times. Vigorous boiling during degassing assists mixing. The ratio of the volume of retained water in the drained system to the volume of the filled system is 1:8. The mole fraction of hydrogen in the final mixture with highest isotopic enrichment was 0.0057 ± 0.002. The ionic conductivity was 110% of the theoretical conductivity of equibrium D_3O^+ and OD^- in the mixture.

Highly deuterated columns with a smaller D_2O expenditure could be obtained by drying the column before exposure to D_2O. Direct vacuum drying or after pre-rinsing with dioxane or ether produced resin beads with a tendency to disintegrate upon re-hydration.

4c. Isotopic analysis

The isotopic composition of the H_2O was determined from samples drawn through a Teflon-coated silicone rubber septum with a syringe. Density measurements with a 3 ml pyncnometer are used to determine isotopic enrichment for hydrogen mole fractions greater than 0.10. Liquid phase infrared spectroscopy was used for smaller hydrogen mole fractions. Measured hydrogen mole fractions have an uncertainty of 0.002 at 0.000 mole fraction hydrogen increasing to 0.01 at 0.10 mole fraction hydrogen. The uncertainty is 0.01 over the remaining range.

Infrared spectra with 8 cm^{-1} resolution were taken on a Nicolet 7199 FTIR spectrometer using a HgCdTe detector, KBr beamsplitter, and Globar source. Liquid samples were taken in 1 cm path cylindrical quartz cells. Figure II-5 shows the infrared spectrum of three different H_2O-D_2O mixtures in the 5600 cm^{-1} to 6800 cm^{-1} region. The peak in the 0.003 mole fraction H_2O spectrum at 6250 cm^{-1} is a D_2O peak, and the shoulder at 6030 cm^{-1} is an HOD absorption. The shoulder height increases linearly as hydrogen mole fraction is increased. To determine isotopic composition, the peak height of a water sample from the liquid system is compared to a calibration based on measurements at 0.011, 0.032, 0.058, and 0.140 mole fraction hydrogen.

Higher resolution gas phase spectra of water vapor in equilibrium with the liquid taken with the same instrument in 15 cm pathlength sapphire window cells could also be used to analyze the isotopic composition. The area of several well-resolved OH and OD stretch lines of HOD and D_2O can be measured if pressure broadened beyond the instrumental resolution of 0.06 cm^{-1} by addition of an inert bath gas; 673 torr of N_2 produces a measured line

Figure II-5

The infrared spectra of 0.003, 0.017, and a 0.038 mole fraction hydrogen sample of water are shown by curves A, B, and C, respectively. The peak at 6030 cm^{-1} is from HOD. The peak at 6250 cm^{-1} is from D_2O. The pathlength is 1 cm. The absolute scale for spectrum A, B, and C, is 0.0760, 0.0804, and 0.0800 base 10 absorbance units/division.

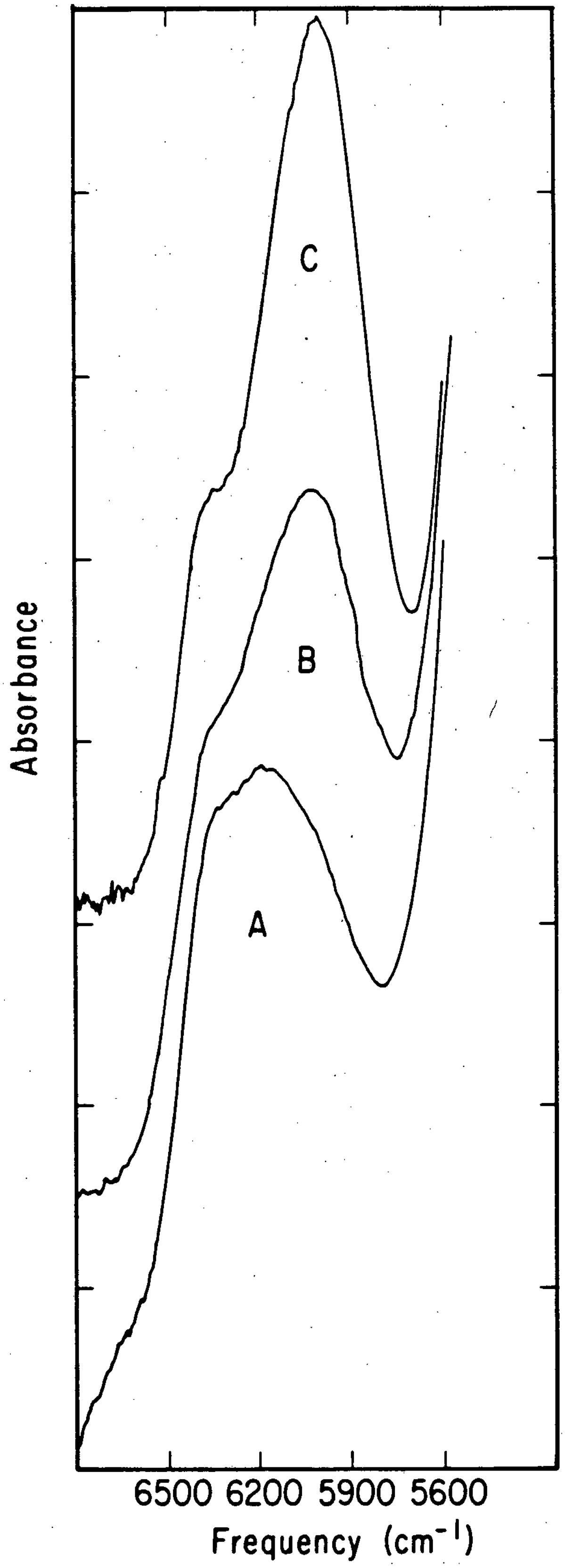

XBL 8212-12407

width of 0.28 cm^{-1}. The liquid phase spectral analysis was found to be easier and probably more accurate.

III. Excitation sources

This section describes generation, wavelength selection, and alignment of light between 1.41 μm and 0.55 μm used to excite liquid water.

Preliminary experiments used a Chromatix CMX4/IR with IR-1 mirrors and model 300A oven and temperature controller. A Chromatix CMX-4/IR consists of a temperature-tuned, $LiNbO_3$ optical parametric oscillator pumped by a Chromatix CMX-4 flashlamp pumped dye laser. The theory of optical parametric oscillation is described in several review articles[6,7]. Wavelengths between 1.35 μm and 0.98 μm mere generated. The signal and idler beam were separated using a Schott JB-639522 near IR linear variable filter. Up to 200 μJ pulses of combined signal and idler wavelengths could be generated when pumping with a 6 to 7 mJ, 1 μs pulse near 0.59 μm. Typical powers after the linear variable filter were 10-30 μJ. Output powers were measured with a Molectron J3-05 pyroelectric detector. Wavelengths were determined with a Bausch and Lomb 600 groves/mm diffraction grating blazed at 28°41'. The grating is calibrated using visible light from the dye laser. The dye laser wavelength is determined with a 1.5 meter Jobin-Yvon monochromator.

Quantum yields at 9050 cm^{-1} and 10204 cm^{-1} agree within 7% and 27% of values measured with the Quanta Ray system to be described. Much higher pulse energies were obtained with a Quanta Ray DCR-1, Nd^{+3}:YAG-pumped PDL-1 dye laser that can be Stokes shifted in a high-pressure hydrogen or methane Raman cell[8]. This system is used for all reported quantum yields. Dye laser output is focussed first with a 50 cm lens external to the 1 m Raman cell. Sixty centimeters from this lens is an internal 6.7 cm focal length lens supported in a teflon holder. The internal lens produces a second focus which enhances second Stokes output. Figure II-6 shows the geometry of the Raman generator. The desired output wavelength is selected with a quartz prism, Corning 7-56 or Corning 7-69 filter. Power is optimized by adjusting the Raman cell gas pressure and divergence of the dye laser. Table II-1 shows optimum conditions at several output wavelengths.

The dye laser wavelength is checked with a Beck Wavelength Reversion Spectrometer. Reported wavelengths are accurate to 1 nanometer. Near infrared frequencies are calculated from the dye laser frequency and the Raman frequency of the gas in the Raman cell. Hydrogen produces a frequency change of 4155 cm^{-1} per shift. Methane produces a frequency change of 2917 cm^{-1} per shift. The typical average light flux at the cell is 20 MW cm^{-2} in a spot 1.5 mm^2. This corresponds to an 8 nsec pulse, with a

Figure II-6

Excitation source and Raman shifter geometry. The external lens is a 50 cm F.L. quartz lens. The internal lens is a 1 cm diameter 6.7 cm F.L. glass lens.

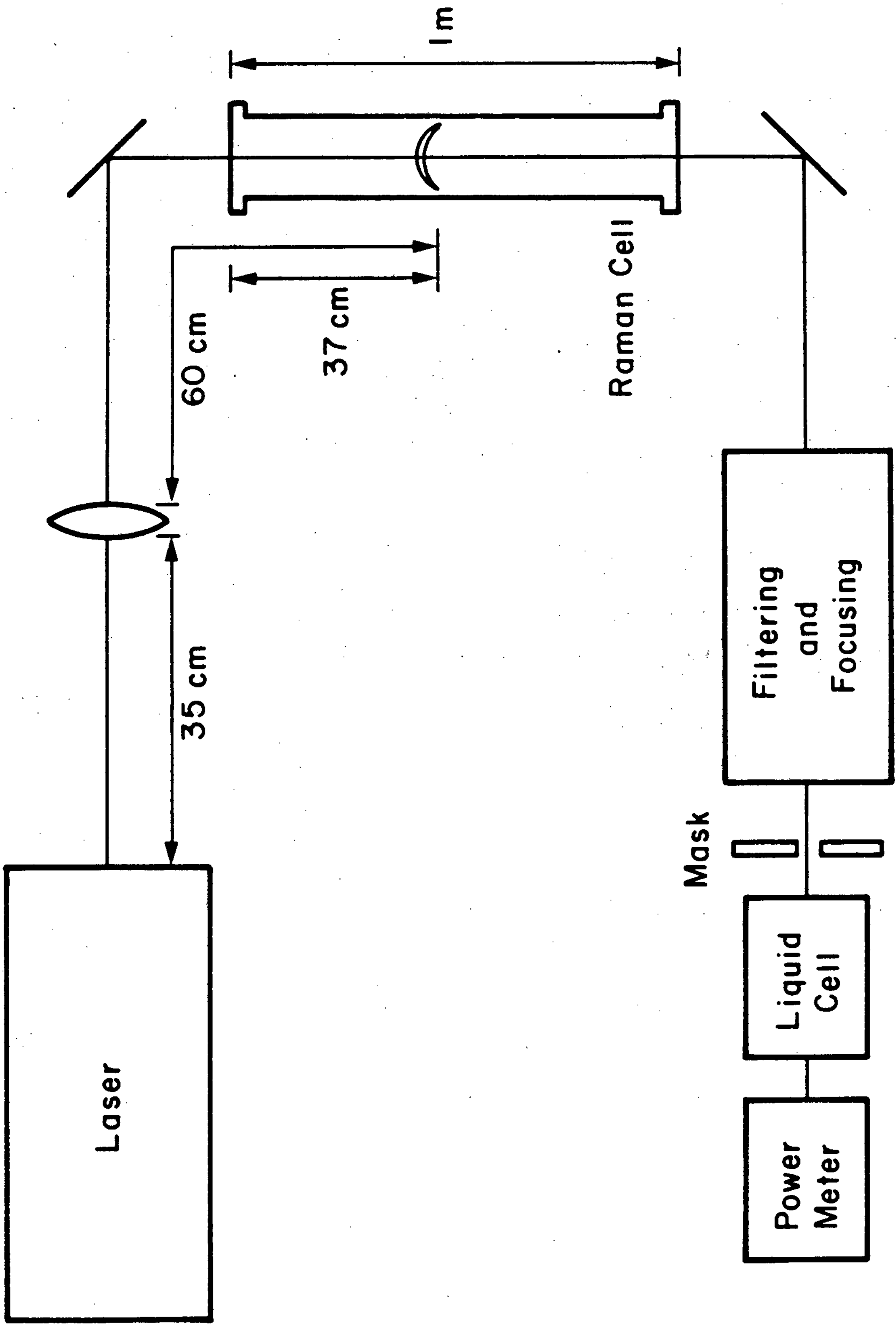
1 m
Raman Cell
60 cm
37 cm
35 cm
Laser
Filtering and Focusing
Mask
Liquid Cell
Power Meter

XBL 8212-12404

fluence of 0.16 J/cm^2 and energy of 2.4 mJ. The beam profile is not a uniform Gaussian because the final dye amplifier is longtitudinally pumped with the "doughnut" mode Quanta Ray.

For some experiments at 1.06 μm, a Raytheon SS404 Nd^{+3}:YAG laser is used[9]. The maximum flux of 55 MW cm^{-2} at 1.06 μm was used in quantum yield measurements in D_2O. The pulse length is 15 ns, the fluence 0.83 J/cm^2, and the beam area 1 mm^2. The Raytheon beam profile is of good quality with no "doughnut". For 2.28 μm output, the laser pumps an angle tuned $LiNbO_3$ optimal parametric oscillator[10] to generate a 1.2 mJ, 10 ns pulse with a 12 MW cm^{-2} flux at the conductivity cell. Pulse energies are measured with a Scientech 38-0101 calorimeter.

Comparisons of quantum yield measurements at 1.06 μm show that the quantum yield is independent of electrode geometry, focussing parameters, and beam profiles. Table II-2 shows that measurements with three cells and three laser sources agree within 35%.

The cell is initially aligned with a visible beam by tilting the cell until the spot reflected from the rear window does not strike the electrodes. An Eastman Kodak IR Phosphor card is used to direct the near infrared light. Spurious signals result if the laser beam strikes the cell electrodes. The problem is eliminated by use of a mask. The mask is made of a pair of anodized

Table II-1. Table of Raman cell output energies

Dye	Raman Medium	Raman Shift	λ in (nm)	λ out (nm)	Energy (mJ)
DCM	H_2	2nd Stokes	650	1410	> 0.4
Rh640	H_2	2nd Stokes	600	1197	1.6
Rh610	H_2	2nd Stokes	586	1142	2.25
Rh610	H_2	2nd Stokes	577	1110	2.4
Rh590	H_2	2nd Stokes	572	1090	1.4
Rh590	H_2	2nd Stokes	560	1047	2.1
DCM	CH_4	2nd Stokes	628	990	1.7
DCM	CH_4	2nd Stokes	624	980	1.3
DCM	CH_4	2nd Stokes	615.8	961	0.75
RH640	CH_4	2nd Stokes	616.6	950	2.9
Rh640	CH_4	2nd Stokes	605.8	937	1.2
Rh640	CH_4	2nd Stokes	600	923	3.5
DCM	H_2	1st Stokes	663.8	916.5	2.0
DCM	H_2	1st Stokes	660	909	2.4
DCM	H_2	1st Stokes	650	890.5	2.7
DCM	H_2	1st Stokes	629	852	4.2
DCM	H_2	1st Stokes	627	847	4.0
Rh640	H_2	1st Stokes	611.6	820	4.0
RH640	H_2	1st Stokes	600.4	800	3.5
RH590	H_2	1st Stokes	564.7	738	5.1

Optimum pressures for 2nd Stokes is 400-500 psi for both H_2 and CH_4.

Optimum pressure for 1st Stokes output in hydrogen is 165 psi at 738 nm, increasing to 375 psi at 916.5 nm. Typical energy conversion efficiencies for 1st Stokes in hydrogen are between 10 and 17%, 2nd Stokes efficiency in hydrogen is 4-5%.

razor edges 1.4 mm apart, 9 mm in front of the electrodes. The razor edges are oriented parallel to the electrode plane.

IV. Electronics

This section describes both the important and the unwanted features of the signal, then details the electronics chosen to record the important and eliminate the unwanted portions.

Important features of the conductivity versus time, Figure II-7, include (1) the pre-laser background conductivity, (2) the peak conductivity immediately following excitation, (3) the conductivity relaxation rate, and (4) the baseline increase after relaxation. Unwanted features of the observed conductivity include (1) the small magnitude of the transient signal; especially when compared to the large background conductivity, and (2) the presence of large amplitude low frequency noise. The transient signal magnitude is as small as 3×10^{-6} times the background conductivity resulting from equilibrium hydronium and hydroxide ion plus a small concentration of unidentified ions. The equilibrum conductivity has a time varying noise component with a frequency between D.C. and about 20 Hz. The magnitude is up to 700 times as large as the signal magnitude. The noise comes from flow turbulence in the cell and from an undetermined

Table II-2. Comparison of quantum yields for excitation at $9400\ cm^{-1}$

Cell	Laser Source	Temp. (°C)	Ø
Knight et al.[A]	Nd^{+3}:glass Laser Associates	10	3.6×10^{-7}
		25	6.0×10^{-7}
Expoxied Strip Quartz	Raman shifted dye	10	2.8×10^{-7}
Teflon	Raman shifted dye	10.6	3.25×10^{-7}
	Raytheon Nd^{+3}:YAG	10	3.8×10^{-7}
		23	4.85×10^{-7}
		25	4.6×10^{-7}

A) B. Knight, D.M. Goodall, R.C. Greenhow, J. Chem. Soc. Faraday Trans. 2, 75, 841 (1979).

source. Perhaps reactive metal atoms reduced from Na^+ ions near the cathode catalytically produce OH^- ions and H_2 gas.

An A.C. coupled amplifier could have been used to eliminate problems caused by the two unwanted features of the signal by amplifying the small fast transient while filtering out the static background and low frequency noise. However, it would also produce baseline overshoot or baseline droop which distorts the magnitude of the baseline step.

The electronics actually used consists of four parts. The conductivity monitor separates the static conductivity from the transient conductivity and amplifies only the transient conductivity. The static conductivity is monitored separately. The triggered differential amplifier increases the transient voltage and attenuates the low frequency noise. The digitizer records the signal. The optical isolator prevents laser noise from entering the system along triggering lines.

A. Conductivity monitor

The conductivity monitor, shown in Figure II-8, is a conductivity bridge with transient current differences between the two arms detected with an Analog Devices AD507K operated as a current to voltage converter. The

Figure II-7

Transient conductivity in H_2O showing (1) the pre-laser background conductivity, (2) the peak conductivity immediately following excitation, (3) the relaxation rate, and (4) the baseline increase after relaxation. The magnitude of the transient is as small as 3×10^{-6} times the level of background conductivity, (1). The signal shown here has a peak magnitude about 10^{-4} times the background conductivity. The temperature is 19.8 C, with excitation at 9400 cm^{-1}.

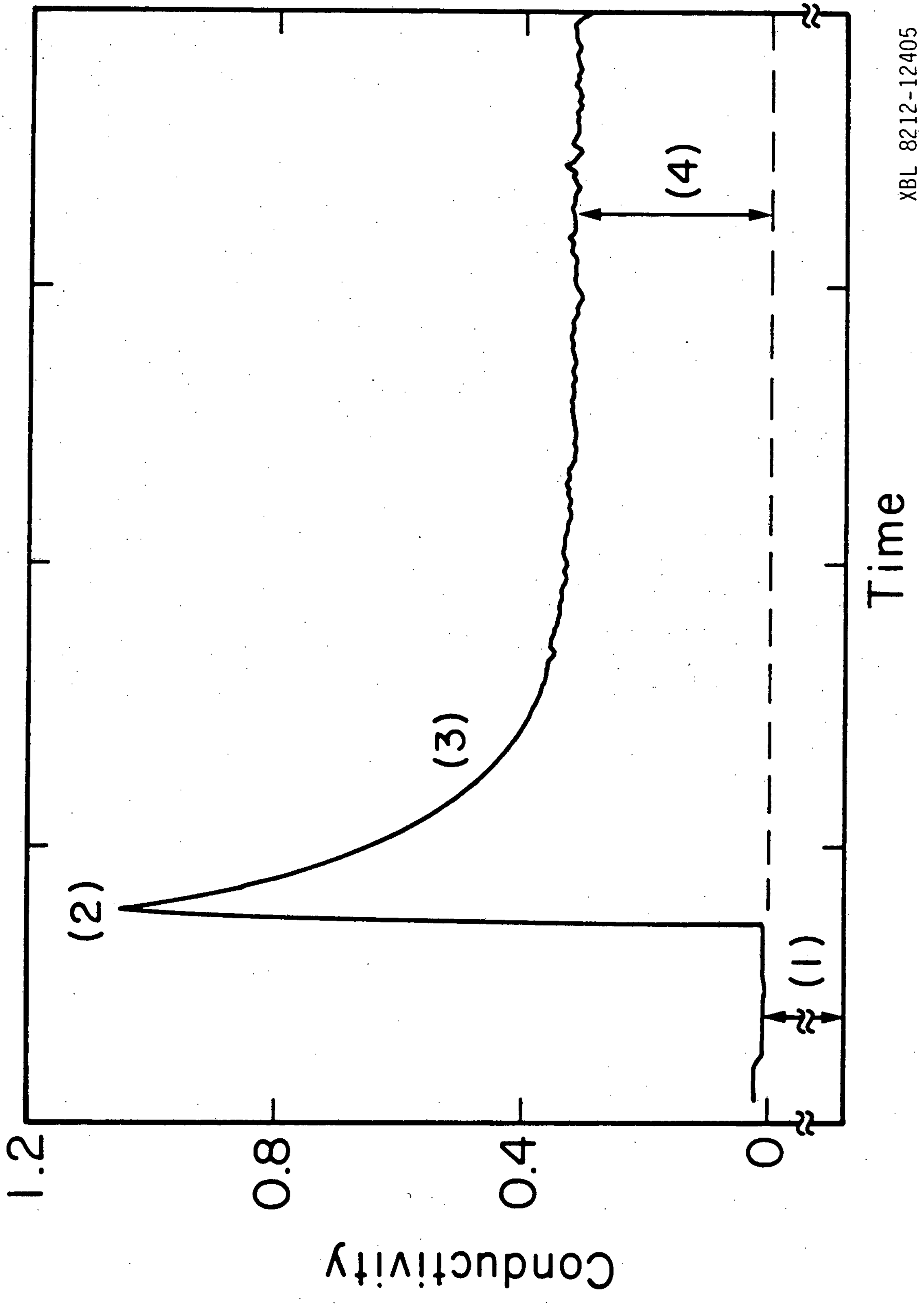

XBL 8212-12405

to ground by one arm of the conductivity bridge. The cell in the other arm is illuminated by the laser. Potentiometer R6 allows D.C. balance of the bridge to prevent current flow into the current to voltage converter in the absence of a transient conductivity. Bridge balance eliminates contribution from the static conductivity. Diodes D1 and D2 protect the amplifier input from voltage surges caused by switching the bias voltage polarity. Capacitors C2 and C3 prevent the bias voltage reference point from changing on the timescale of the transient conductivity signal. Capacitor C1 prevents the magnitude of the bias voltage from varying with time.

The voltage across R3 is monitored with voltage follower LM310 and is proportional to the equilibrum conductivity. Signal output from the current to voltage converter proceeds to the triggered differential amplifier.

B. Triggered Differential Amplifier

The triggered differential amplifier is shown in simplified form in Figure II-9. The circuit has two modes of operation depending on whether or not the signal is being digitized. When the conductivity is not being digitized, the FET is turned on, sending the same signal to both inputs of the CA3130 differential amplifier. This results in a gain of one and an output near zero volts.

Figure II-8

Schematic diagram of the transient and static conductivity monitor. Resistance is in ohms and capacitance in μfd. V^+ and V^- are +15v and -15v. RC1 and RC2 are the conductivity cell resistances.

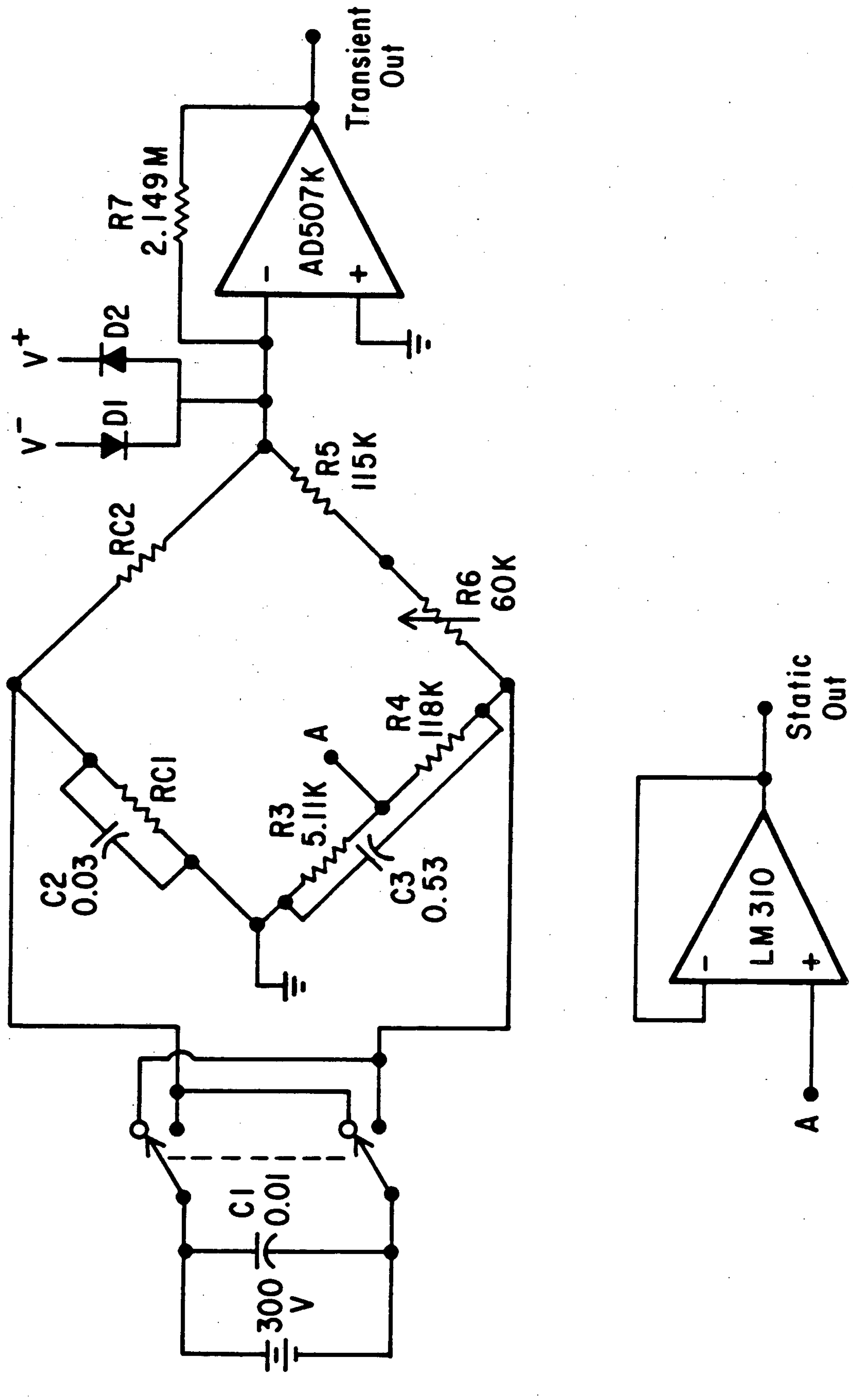
Transient Out
R7 2.149 M
AD507K
-
+
V+
D2
V−
D1
RC2
R5 115K
R6 60K
R4 118K
A
RC1
R3 5.11K
C2 0.03
C3 0.53
C1 0.01
300 V
Static Out
LM310
-
+
A

XBL 831-7731

Figure II-9

Schematic diagram for the triggered differential amplifier.

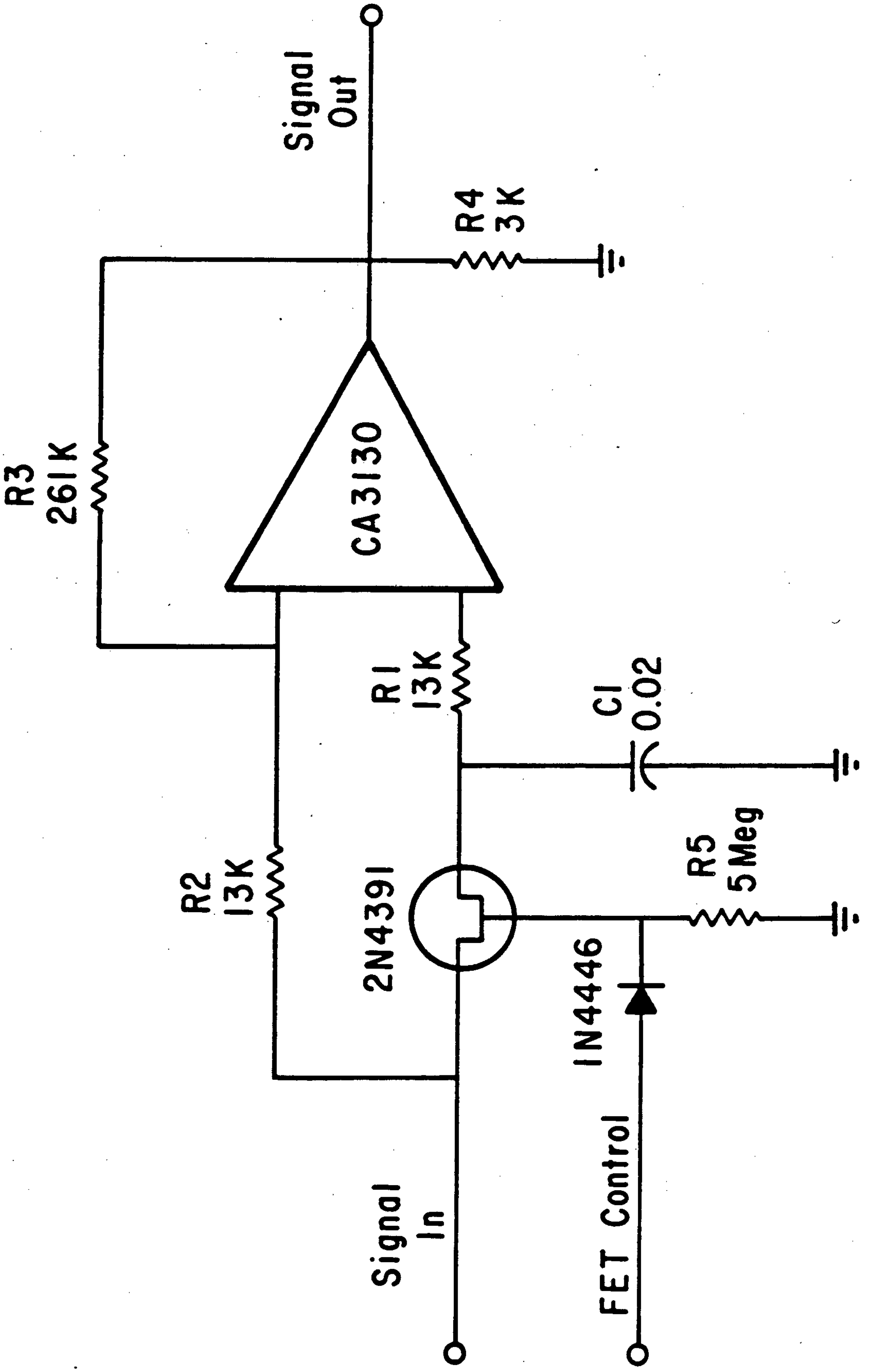
Signal Out
R4 3K
R3 261K
CA3130
R1 13K
C1 0.02
R2 13K
2N4391
R5 5Meg
1N4446
Signal In
FET Control

XBL 831-7729

During this mode, low frequency noise is eliminated. The mode of operation is changed after digitization begins. The FET is turned off, capacitor C1 stores the instantaneous signal voltage, and the circuit amplifies the difference between the stored voltage and the subsequent voltage with a gain of 20. The system risetime from conductivity monitor input to triggered differential amplifier output is about 2.5 μsec.

C. Digitizer

The signal is D.C. coupled to the 7A16 vertical amplifier of a Tektronix 7912 transient digitizer with a PDP 11/10 Digital Equipment computer averager or to the 7A16P vertical amplifier of a Tektronix 7912 AD transient digitizer with LSI-11 computer averager. The digitizers use an electron beam to write on a diode array, similar to the way an electron beam writes on the phosphor screen of an oscilloscope. Digitization occurs when a second electron beam reads the diode array. If high frequency noise is not filtered out, the writing beam intensity is spread over so many vertical diodes in some horizontal channels that no written signal is detected by the read beam. Inaccurate decay times and peak amplitudes can result.

A low pass filter preceding the digitizer input filters out high frequency noise. A cut off frequency of 300 kHz is for signal decay times less than about 75 μs. The cut off frequency is 60 kHz for longer decay times. The low pass filter also attentuates the signal for a net gain from triggered differential amplifier input to low pass filter output of 12.29 for 60 kHz cut off and 6.3 for 300 kHz.

D. Timing Electronics

Three synchronized electrical pulses needed to control the experiment are shown in Figure II-10. They are (1) a digitizer trigger pulse, (2) a control pulse for the FET of the triggered differential amplifier, and (3) a laser Q-switch trigger needed to generate laser output. Generally, laser-generated electrical pulses are used for pulses (1) and (3). A pre-laser baseline is digitized during the time between pulse (1) and pulse (3). Occasionally, longer delays than provided by the laser are needed. A pulse generator and adjustable delay can be used to trigger the digitizer and laser. Pulse (2) is generated externally. This section describes the optical isolator used to isolate the laser electronics from the signal collection electronics and the timing circuit used to generate pulse (2).

Figure II-10

Timing diagram of electrical pulses used for experimental control. Pulse (1) triggers a digitizer. Pulse (2) controls the triggered differential amplifier, and pulse (3) controls the laser Q-switch. (A) and (B) show the timing of the laser output and conductivity signal relative to the electrical pulses.

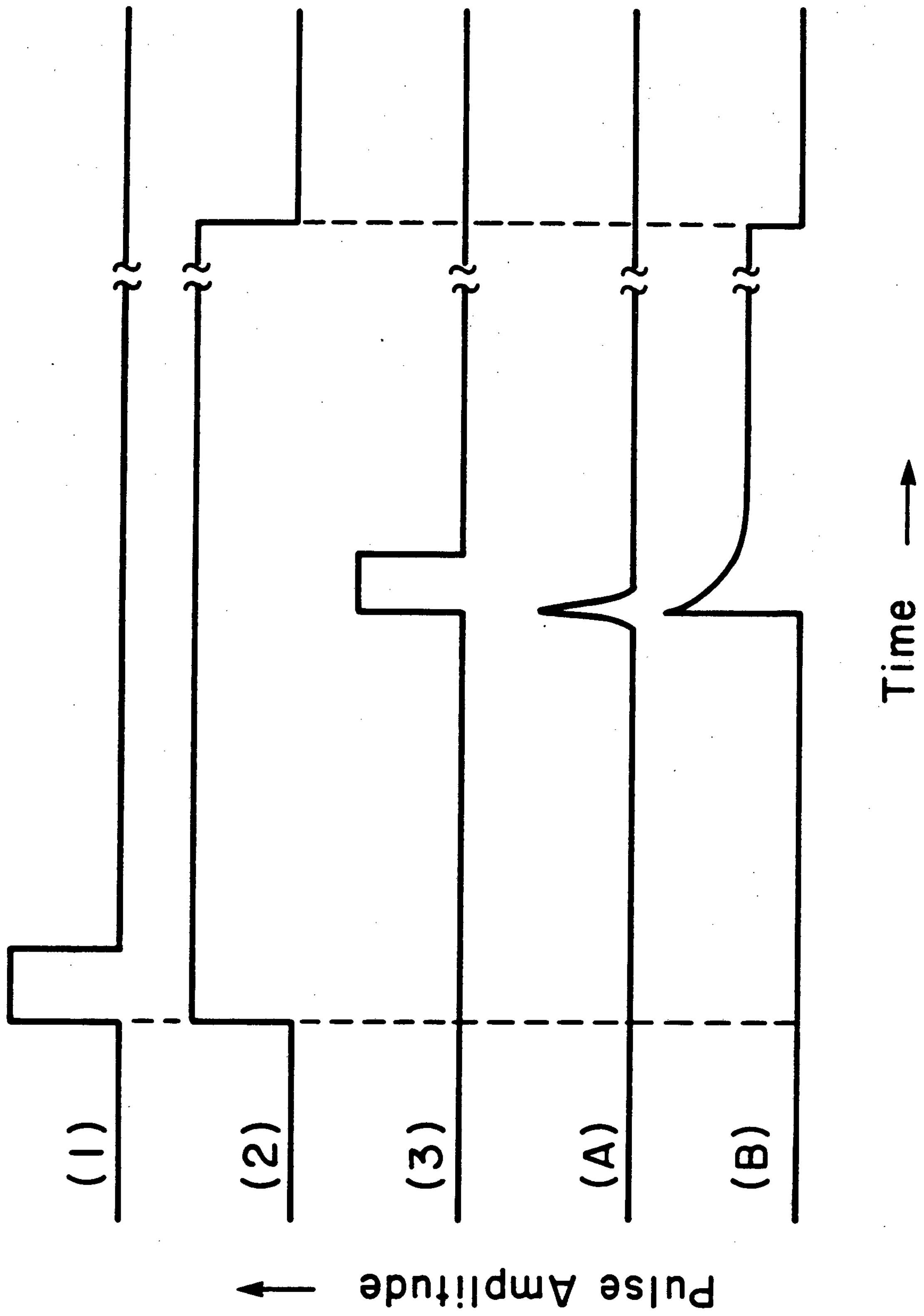
(1)
(2)
(3)
(A)
(B)
Pulse Amplitude
Time

XBL 831-7726

The schematic diagram in Figure II-11 shows an optical isolator which eliminates transmission of laser noise to the signal collection electronics. It consists of a 6N136 optical isolator chip followed by an inverting amplifier capable of driving both the signal averager and a timing circuit for the FET in the triggered differential amplifier. With the Quanta-Ray Nd:YAG laser there is a delay of about 240 μs between the lamp pulse out and the laser pulse. Digitizer triggering with the lamp out pulse, (1), allows a prelaser baseline to be recorded. With the Raytheon YAG laser there is an ≈ 200 μs delay between the first amplifier out pulse (1) and laser output.

The timing circuit in Figure II-12 generates a gate which controls the FET. A pulse from the opto-isolator triggers the LM311 comparator, which starts a timing cycle in a 555 chip configured as a monostable multivibrator. The 7 or 60 ms output pulse turns off the FET after inversion by LM311, A2.

E. Electronics performance

Signal collection proceeds at the 10 Hz laser repetition rate. Typically, 512 shots are averaged, the conductivity cell polarity reversed, and the same number

Figure II-11

Schematic diagram of optical isolator. Resistor values are from left to right, 300 Ω, 1 Megohm, 22 kΩ, 49.9 kΩ, 200 kΩ, and 51 Ω. The capacitor is 0.47 μFd.

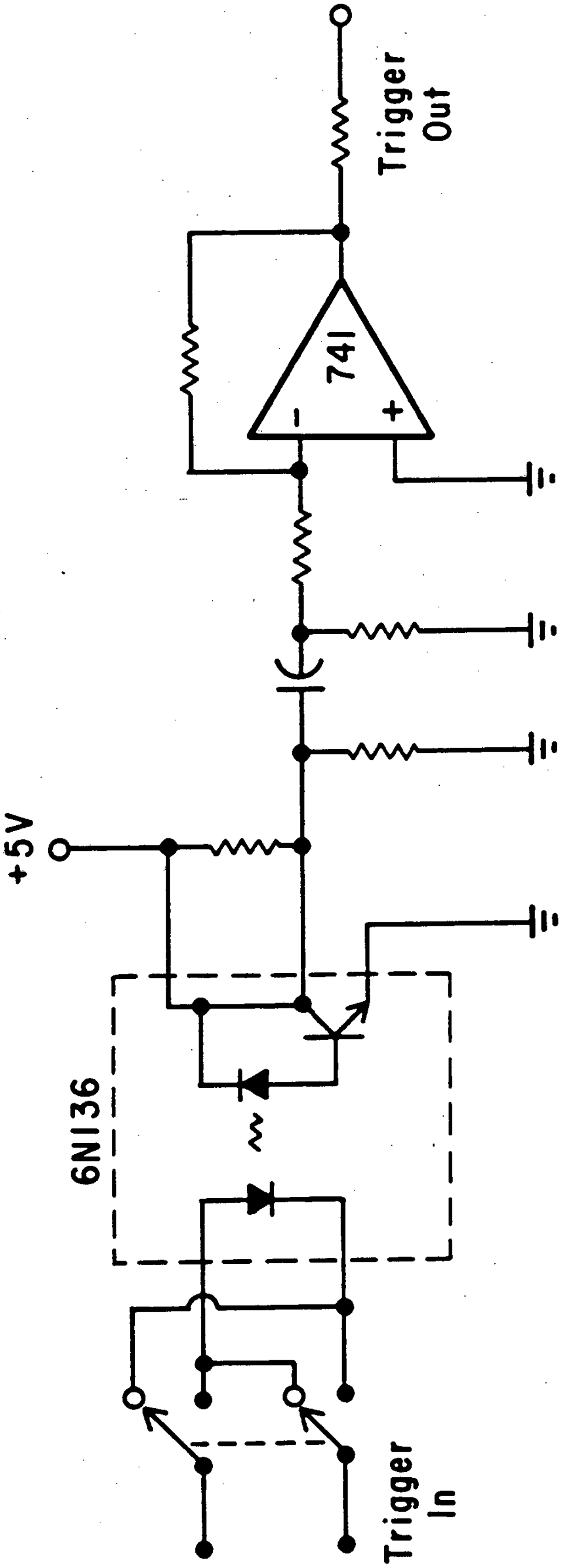
Trigger Out
741
+5V
6N136
Trigger In

XBL 831-7728

Figure II-12

Schematic diagram of timing circuit used to control the FET in the triggered differential amplifier. Resistor R1 is 62K or 510KΩ for a 7 or 60 ms output pulse.

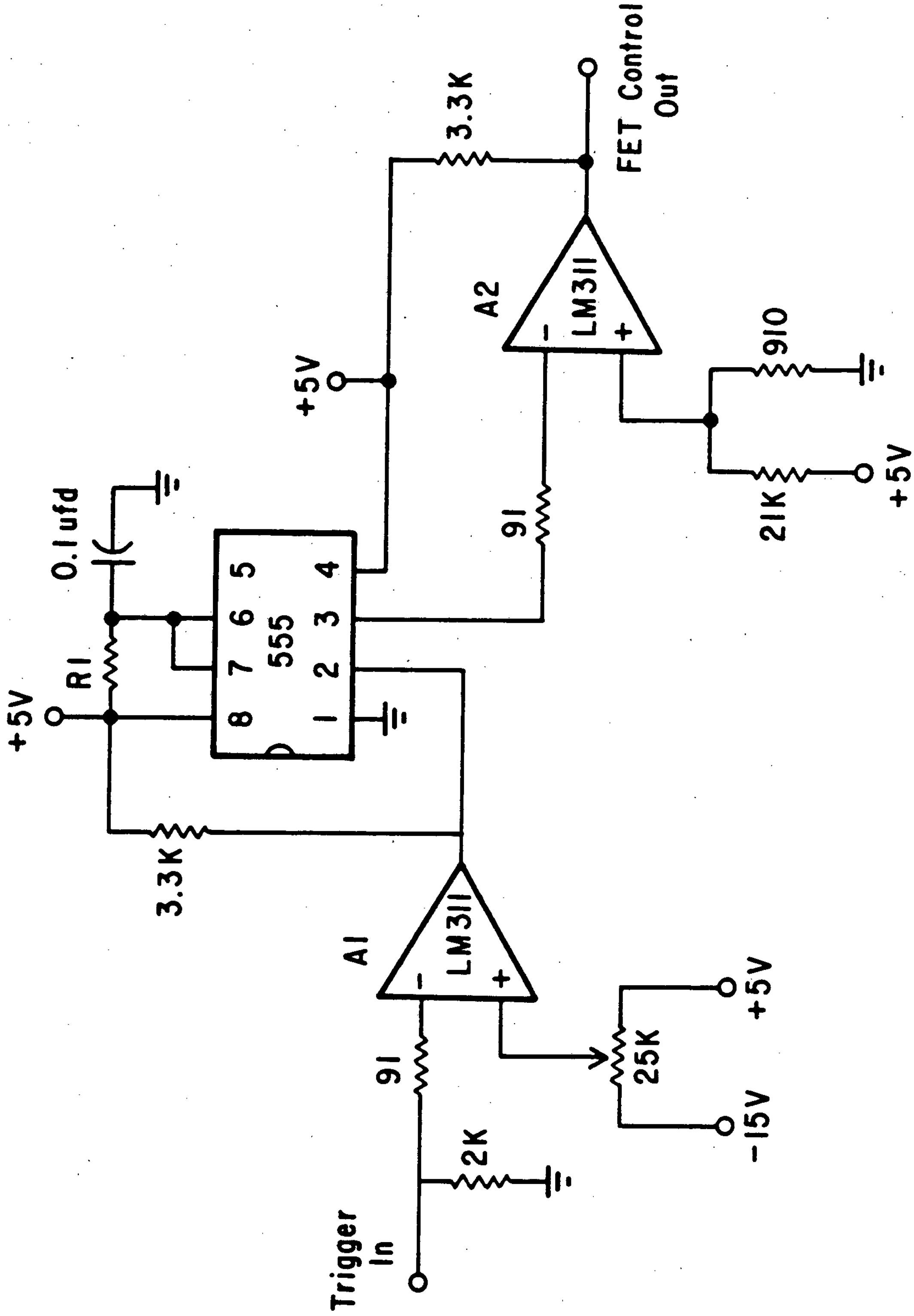
Trigger In
2K
91
A1
LM311
-
+
25K
+5V
-15V
3.3K
+5V
R1
0.1ufd
8
7
6
5
555
1
2
3
4
+5V
91
A2
LM311
-
+
910
21K
+5V
3.3K
FET Control Out

XBL 831-7730

of additional shots averaged. Subtraction of the two signals eliminates pick-up and multiplies the conductivity signal by two. The subtracted pick-up is about 5 x 10^{-10} A in magnitude. A step increase of about 1.5 x 10^{-10} A with 300 V applied to the conductivity cell produces a conductivity step with signal to noise of one after averaging 1024 shots. This step increase corresponds to a 3 x 10^{-13} molar change (3 ppm) in hydronium and hydroxide ion concentrations at 25°C.

V. Absorption spectra

Absorption spectra between 1.19 μm and 0.63 μm were taken of H_2O/D_2O mixtures in a 10 cm cylindrical quartz cell using a Cary 14 spectrometer with an IR1 detector. Mixtures were prepared by weight. Results at several wavelengths of interest are shown in Table II-3. The spectra are shown in Figure II-13. The absolute baseline was set by comparison with D_2O data by Sullivan[11]. The absorbance in H_2O at 650 nm is 13% greater than measured by Tam and Patel[12] by optoacoustic measurements.

Figure II-13

Absorption spectrum of liquid H_2O (A), 0.485 mole fraction hydrogen (B), 0.297 (C), 0.198 (D), 0.099 (E), D_2O (F), and the spectrometer baseline (G). Curves D and E should be shifted upward by 0.005 absorbance units. The path length is 10 cm.

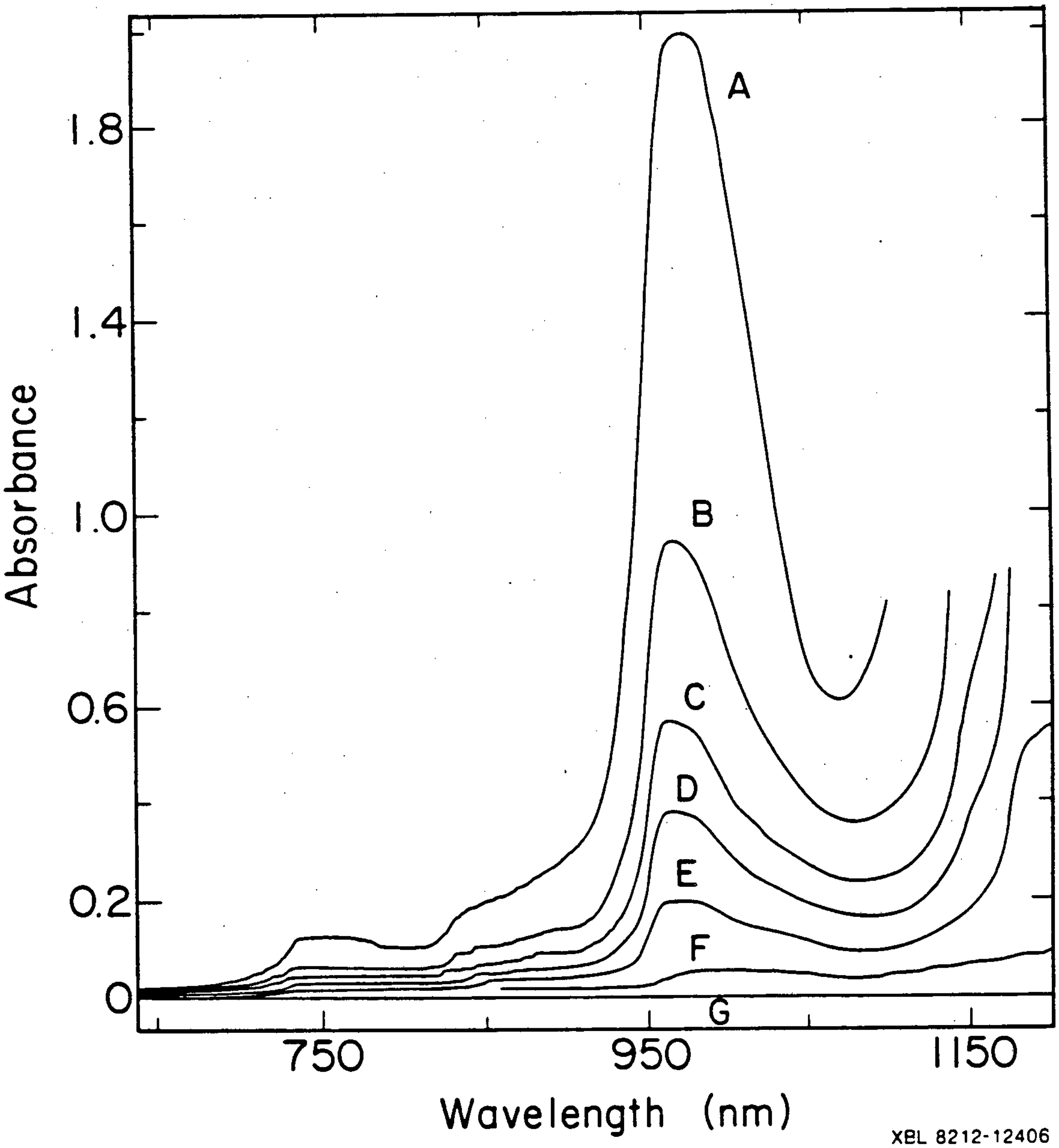

XBL 8212-12406

Table II-3. Absorbance[a] of H_2O/D_2O mixtures.

		mole fraction hydrogen				
λ (nm)	D_2O	0.099	0.198	0.297	0.485	H_2O
737.8	0.000278[b]	0.0015	0.0028	0.0039	0.0058	0.0117
799.25	0.00042[b]	0.0016	0.0028	0.0039	0.0053	0.0097
820	0.00052[c]	0.0017	0.0029	0.0040	0.0058	0.0108
847.3	0.0008	0.0027	0.0046	0.0061	0.0097	0.0185
890.5	0.0017	0.0040	0.0062	0.0089	0.0134	0.0258
909.4	0.0016	0.0048	0.0067	0.0091	0.0148	0.0316
916.5	0.0016	0.0049	0.0071	0.0104	0.0160	0.0344
922.6	0.0018	0.0051	0.0079	0.0112	0.0184	0.0403
923.6	0.0018	0.0051	0.0083	0.0116	0.0189	0.0414
950.2	0.0021	0.0120	0.0226	0.0345	0.0585	0.1259
950.4	0.0021	0.0121	0.0227	0.0349	0.0592	0.1279
961.1	0.0037	0.0197	0.0383	0.0565	0.0928	0.1830
989.8	0.0055	0.0188	0.0343	0.0499	0.0836	0.1862
1047.0	0.0050	0.0125	0.0208	0.0284	0.0427	0.0681
1063.0	0.0044	0.0112	0.0186	0.0257	0.0383	0.0635
1101.0	0.0048	0.0105	0.0175	0.0250	0.0385	0.0817
1109.0	0.0050	0.0114	0.0186	0.0264	0.0426	--

[a] Absorbance (cm^{-1})

[b] from Sullivan, reference (11)

[c] extrapolated form Sullivan's data

$I/I_o = 10^{(-Abs)(length)}$

1. J.D. McIntyre and D.M. Kolb, Symp. Faraday Soc., 4, 99 (1970).
2. A. Prostak, H.B. Mark, Jr., and W.N. Hansen, J. Phys. Chem., 72, 2576 (1968).
3. "Ultrapurity: Methods and Techniques" edited by Morris Zief and Robert Speights (Marcel Dekker, Inc., New York, 1972).
4. G. Jones and B.C. Bradshaw, J. Am. Chem. Soc. 55, 1780 (1933).
5. P.D. Goulden and P. Brooksbank, Anal. Chem. 47, 1943 (1975).
6. R. Byer and R.L. Herbst, in "Non-linear Infrared Generation", edited by Y.R. Shen (Springer-Verlag, New York, 1977).
7. A. Yariv, "Quantum Electronics" (J. Wiley and Sons, New York, 1975).
8. L. Young, Ph.D. Thesis, University of California, Berkeley (1981).
9. M. Zughul, Ph.D. Thesis, University of California, Berkeley (1978).
10. H.L. Dai, Ph.D. Thesis, University of California, Berkeley (1981).
11. S.A. Sullivan, J. Opt. Soc. Am. 53, 962 (1963).
12. A.C. Tam and C.K.N. Patel, Applied Optics, 18, 3348 (1979).

CHAPTER III. ANALYSIS

The analysis consists of two parts. The first is a calculation of the quantum yield for the laser induced reaction. The second is a calculation of the thermal recombination rate from the equilibrium relaxation that follows perturbation by the laser-induced dissociative ionization. The end of the analysis section includes a discussion of experimental errors in the laser induced reaction.

I. Laser-induced dissociative ionization quantum yields

The goal of the data analysis is to relate the transient voltage changes shown in Figure II-7 to the chemical and physical processes of the dissociative ionization reaction. This section shows that the transient can be related most directly to reaction quantum yield. First, after some background, it is shown that the reaction kinetics can not be determined directly from the transient conductivity.

Absorption of a photon with energy greater than the dissociative ionization reaction threshhold initiates two competitive processes, both affecting the solution conductivity. The processes are (1) formation of separated product ions, H_3O^+ and OH^-, and (2) energy thermalization to produce a temperature jump.

The kinetics of the two processes are described by the following equations:

$$(H_2O)^* \underset{k_{-1a}}{\overset{k_{1a}}{\rightleftharpoons}} (H^+ \ldots OH^-) \underset{k_{-1b}}{\overset{k_{1b}}{\rightleftharpoons}} H^+ + OH^- \qquad (1)$$

$$(H_2O)^* \underset{k_{-2}}{\overset{k_2}{\rightleftharpoons}} (H_2O) \qquad (2)$$

$(H_2O)^*$ denotes a vibrationally activated species, probably involving more than one H_2O, (H_2O) a vibrationally relaxed species, $(H^+ \ldots OH^-)$ an ion pair, and $H^+ + OH^-$ separated ions.

Processes (1) and (2) can be observed by monitoring the transient conductivity. The conductivity, L, is

$$L = \left[\lambda_{H^+} C_{H^+} + \lambda_{OH^-} C_{OH^-}\right] + \lambda_i C_i \qquad (3)$$

with λ_i and C_i the single ion equivalent conductivity and concentration of species i, respectively. So, process (1) directly increases the conductivity in proportion to the concentration of product ions C_{H^+} and C_{OH^-}. The temperature jump of process (2) increases the conductivity by increasing the equivalent ionic conductivity, λ, of the pre-existing ions and increasing equilibrium ionic concentrations.

There are two timescales in the reaction kinetics that affect the conductivity. A rapid thermalization rate, k_2, and rapid ion pair formation rate, k_{1a}, preceding a slow relaxation of the $H_2O \rightleftarrows H^+$ and OH^+ disequilibrium, (3) in Figure II-7. If the electronics were infinitely fast, (1), the transient risetime in Figure II-7 would be related to k_1 and k_2. In practice, the electronics risetime is slow compared to $1/k_1$ and $1/k_2$, but fast compared to the equilibrium relaxation rate. This means neither k_1 nor k_2 can be determined from the signal risetime.

However, the quantum yield can be determined from step (4) in Figure II-7, and the equilibrium relaxation, (3), extrapolated to (2), the conductivity peak. The quantum, yield, ϕ, for the production of separated ions is the fraction of vibrationally activated species that react.

$$\phi = \frac{k_1[(H_2O)^*]}{(k_1 + k_2)[(H_2O)^*]} \tag{4}$$

where k_1 is the overall rate for production of separated ions. Recognizing

$$\frac{k_1}{k_1 + k_2}[(H_2O)^*] = [\text{reactive events}] \tag{5}$$

and

$$[(H_2O)^*] = [\text{absorbed photons}] \tag{6}$$

the quantum yield becomes

$$\phi = \frac{[\text{reactive events}]}{[\text{absorbed photons}]} = \frac{[\text{product } H^+]}{[\text{absorbed photons}]} \quad (7)$$

The remainder of this section shows how the quantum yield is calculated. The concentration of absorbed photons is calculated, from either the baseline step, which is proportional to the temperature jump, or from the absorption spectrum and transmitted laser energy. The concentration of reactive events is related to the conductivity jump. Also, the measured voltage changes must be related to the absolute conductivity changes.

A. Concentration of Absorbed Photons

The concentration of absorbed photons is calculated from either the measured conductivity step or from the absorption spectrum of the water. First, the method using the conductivity step is described.

1. Concentration of absorbed photons from the conductivity steps.

The concentration of absorbed photons is related to the temperature increase calculated from the conductivity step. The necessary equations for any composition and temperature are given. Calculated concentrations assume a uniform spatial distribution of absorbed photons and product ions. Actually, the laser intensity is not uniform and does not completely fill the interelectrode region. The actual laser geometry does not influence the calculated quantum yields as shown in Appendix A.

The concentration of absorbed photons, [N], is given by

$$[N] = \frac{C_p \rho \Delta T}{hc\nu N_A} \tag{8}$$

where C_p is the specific heat, ρ is the density, N_A is Avogadro's number, and $hc\nu$ is the photon energy. For H_2O, equation (8) becomes

$$[N] = \frac{(28730)\Delta T}{\nu} \tag{9}$$

where ν is in cm^{-1}, ΔT is in degrees Celsius and [N] is in $moles/cm^3$.

For D_2O

$$[N] = \frac{(25780)\Delta T}{\nu} \tag{10}$$

and for isotopic mixtures, a linear interpolation is made. C_p and ρ are considered temperature independent over the temperature range studied with values taken at 25°C.

For H_2O,

$C_p = 0.998$ cal/gm C [1] and

$\rho = 0.99704$ gm/cm^3 [2].

For D_2O,

$C_p = 1.004$ cal/gm C [3] and

$\rho = 1.10445$ g/cm^3 [2].

For small conductivity changes, temperature changes are given by the derivative of equation (3).

$$\Delta L = \frac{dL}{dT} \Delta T , \tag{11}$$

with the derivative given by

$$\frac{dL}{dT} = \sum_i \left(\frac{d\lambda_i}{dT} C_i + \lambda_i \frac{dC_i}{dT} \right) . \tag{12}$$

Thus, two sources contribute to the conductivity step. The first term is the temperature-induced change in ionic mobilities and the second is the temperature-dependent water ionization equilibrium.

The conductivity and concentration of four different ions, H^+, OH^-, Na^+, and Cl^-, are used in equation (12). The theoretical concentration and conductivity of H^+ and OH^- ions is used in equation (12). The concentration of Na^+ and Cl^- is found by attributing the measured excess conductivity above that from H^+ and OH^- to Na^+ and Cl^-. No significant error is introduced if the excess conductivity is produced by a fully dissociated species other than NaCl. (The discussion of errors section shows that the quantum yield is relatively insensitive to errors in the contribution of impurity ions to the conductivity step and jump.) The temperature dependence of the equivalent conductivity is given by the temperature dependence of the solvent viscosity independent of the ionic identity for small concentrations and temperature-independent ionic radii.

$$\lambda_i = \frac{P_i}{\eta(T)} \qquad (13)$$

where $\eta(T)$ is the solution viscosity and P_i is the proportionality constant. From Stokes' Law, $P_i = Ze_oF/1800\ \pi r_i$. Ze_o is the ionic charge, and r_i the ionic radius.[4] The equivalent conductivities used for NaCl are as follows.

For H_2O

$$\lambda_{Na^+} + \lambda_{Cl^-} = 67.188 + 2.135(T) + 9.49 \times 10^{-3}(T)^2 \qquad (14)$$

with T in degrees Celsius and λ in $cm^2\ ohm^{-1}\ mol^{-1}$.[8]

For D_2O

$$\lambda_{Na^+} + \lambda_{Cl^-} = \frac{\lambda_{Na^+}(25°C)}{\eta\ (T)} \qquad (15)$$

where

$$\eta(T) = \exp[(669.2/(T-133.98)) - 3.966] \qquad (16)$$

with T in Kelvin and η in centipoise. Equation (16) is obtained by modifying a functional form that works well for H_2O [5] to fit data for D_2O [6] within about 2% from 20°C to 40°C. The conductivity of NaCl in D_2O, λ (25°C), is 104.2 cm^2 ohm^{-1} mol^{-1} after a small 0.2% correction to the data of Giere at 98.9% D_2O.[7] For mixtures of H_2O and D_2O, a linear interpolation is made between equations (14) and (15). The error is 1.6% when compared to Giere's experimental result at 25°C in 47.8% D_2O.[7]

Ionic conductivities used for H^+ and OH^- ions are as follows:

For H_2O [8],

$$\lambda_{OH^-} = 110.88 + 3.468(T) \qquad (17)$$

with T in degrees Celsius and λ_{OH^-} in $cm^2 ohm^{-1} mol^{-1}$ fits experimental data[9-11] within 6% from 0°C to 75°C and within 2% from 15°C to 75°C.

$$\lambda_{H^+} = 224.33 + 5.305(T) - 0.0113\,(T)^2 \qquad (18)$$

fits experimental data[9,11-13] within 2% from -6°C to 55°C. For D_2O and H_2O/D_2O mixtures at 25°C, a linear extrapolation with mole fraction is unsatisfactory. However,

$$\lambda_{L^+} + \lambda_{OL^-} = 548.9\, X_{H_2O} + 411.2\, X_{HDO} + 363.4\, X_{D_2O} \qquad (19)$$

is satisfactory with an error of 0.65% at 0.096 mole fraction deuterium[7]. Agreement with experimental data is within about 4% over the temperature range from 18°C to 75°C[7] if the conductivity of an arbitrary mixture of hydrogen and deuterium is scaled by the temperature dependence of H_2O conductivity given in equations (17) and (18). Equation (19) requires H_2O, D_2O, and HDO mole fractions of a given isotopic mixture. If the distribution of hydrogen in hydrogen/deuterium mixtures is statistical, then the equilibrium expression for

$$H_2O + D_2O \rightleftarrows 2HDO$$

is

$$[HDO]^2/[H_2O][D_2O] = 4. \tag{20}$$

This approximate expression is used only to obtain a fit of hydrogen and hydroxide ion conductivities. The reader should see reference (14) if a more precise expression for the equilibrium constant is required for other applications.

Equation (12) also needs the temperature dependence of the equilibrium hydrogen and hydroxide ion concentrations, or $K_w(T)$. For H_2O,

$$pK = -6.118 + 4476.6/T + 0.017105(T) \tag{21}$$

with T in Kelvin, agrees within about 0.3% with experimental data[15] for K_w between 0°C and 60°C and is in reasonable agreement with Ackermann's[16] value at 80°C. For D_2O,

$$pK = 4900/(T) - 7.5527 + 0.0200854(T) \tag{22}$$

with the temperature in Kelvin, matches experimental results[17] for K_w within about 0.7% between 5°C and 50°C. The pK of (22) is multiplied by a factor of 0.999 to agree with Gold and Lowe[18] at 25°C. Then K_w is calculated from the expression

$$K_w = K_H[1 - n + n\ell]^3[1 - n + n(K_D/K_H)\ell^{-3}] \tag{23}$$

where K_H is K_w for H_2O, K_D is K_w for D_2O, n is the deuterium mole fraction and ℓ, taken to be 0.69, is the fractionation factor for L_3O^+ ions. L represents an H or a D. Calculated values match experimental values at 25°C within 4.5%, with the maximum deviation at 0.5 mole fraction deuterium. Several alternate expressions for K_w which fit the experimental data equally well are given by Gold and Lowe[18]. Finally, [N], the concentration of absorbed photons, is found by insertion of equations (14), (15), (17), and (23), their temperature derivatives, and the measured conductivity step into equation (12) to give ΔT. Then ΔT is inserted into equation (8).

2. Concentration of Absorbed Photons from Absorption Spectra.

The method described above is not universal. In D_2O, and some isotopic mixtures, the absorbance and the temperature dependence of K_w are smaller than for H_2O. Therefore, the baseline step is too small to measure accurately. Instead, absorption spectra and transmitted laser energies are used to calculate a baseline step and the concentration of absorbed photons. The absorption spectrum and transmitted energy gives the energy deposited in the solution. The baseline conductivity step is proportional to the deposited energy. The proportionality constant is given by calibration at wavelengths and isotopic compositions where a baseline step is readily observed.

The energy absorbed is given by

$$PE_o - PE = (10^{+\varepsilon c \ell} - 1)PE \qquad (24)$$

where PE_o is the laser pulse energy before the cell, PE is the transmitted pulse energy, and $\varepsilon c \ell$ is the absorbance of the water. Generally, the absorbance is calculated from Cary 14 spectra of isotopic mixtures given in the Experimental section. For wavelengths longer than 700 nm, a linear interpolation is made between the two spectra closest in hydrogen mole fraction to the sample being measured. For a few wavelengths shorter than 600 nm, Cary 14 measurements at 650 nm as a function of hydrogen mole fraction are scaled to match results by Tam and Patel for H_2O and D_2O^{19}. The equation used is

$$\varepsilon(\lambda, X_H) = \frac{\varepsilon(650, X_H) - \varepsilon(650, D_2O)}{\varepsilon(650, H_2O) - \varepsilon(650, D_2O)} [\varepsilon_{TP}(\lambda, H_2O) - \varepsilon(\lambda, D_2O)] + \varepsilon_{TP}(\lambda, D_2O)$$

where $\varepsilon(\lambda, X_H)$ is the molar extinction coefficient at wavelength λ, and mole fraction hydrogen, X_H. Subscript TP denotes data by Tam and Patel. Two sources are used for the pure D_2O spectrum at wavelengths longer than 700 nm. Cary 14 spectra are used for wavelengths longer than 820 nm. Data by Sullivan[20] are used for wavelengths between 820 nm and 700 nm.

The deposited energy, if measured in millijoules, is related to a conductivity step as follows:

$$\Delta T = \frac{(PE_o - PE)(2.39 \times 10^{-4} \text{ cal/mJ})}{\rho C_p V} \qquad (25)$$

where ρ is the density in g/cm^3, C_p is the heat capacity in cal/g °C, and V is the effective volume. Replacing ΔT in equation (6)

$$\Delta L = \frac{dL}{dT} \frac{(PE_o - PE)(2.39 \times 10^{-4})}{\rho C_p V} \qquad (26)$$

where ΔL is the conductivity change, and dL/dT is given in equations (11) and (12). All variables in this equation are known except V, the effective volume. To determine V, a wavelength and isotopic composition are chosen where both an absorbed energy and a conductivity step are easily measured. The values are inserted in equation (26) and it is solved for V. Values at 1.06 μm with hydrogen mole fractions of 1.0, 0.9, 0.40, and 0.32; 0.847 μm with mole fractions 1.0 and 0.9; and 1.1 μm with a hydrogen mole fraction of 0.32 were averaged to yield an effective volume of 0.141 ± 0.01 cm^3. Once V is determined, equation (26) is used to calculate baseline conductivity steps at other wavelengths and isotopic compositions. The method for determining the concentration of absorbed photons from the conductivity step was already described.

B. Concentration of reactive events

The remaining information needed to calculate the quantum yield is the concentration of reactive events. The concentration of reactive events is equal to the concentration of product hydronium ion. This shows how the concentration of product hydronium ion, ΔC_{H^+}, is obtained from the peak conductivity. As mentioned previously, the two rapid processes influencing the peak conductivity are: (i) an increase in ionic mobility caused by the rapid temperature jump; and (ii) formation of ionic products. The contribution of process (ii) to the peak conductivity is found by subtracting the portion arrising from process (i). The contribution to the peak conductivity change from process (i) is proportional to the baseline conductivity step.

The conductivity magnitude is about one-third the step size. The lowest arrow curve C, Figure III-1 indicates the contribution to the peak from process (i). For small temperature and ionic concentration changes

$$\Delta L_{peak} = \Delta L_{mob} + \Delta L_{IP}$$

$$= \left[\left.\frac{\partial L}{\partial T}\right|_{C_i} \Delta T \right] + \left[\left.\frac{\partial L}{\partial C_{H^+}}\right|_{T} \Delta C_{H^+} + \left.\frac{\partial L}{\partial C_{OH^-}}\right|_{T} \Delta C_{OH^-} \right] \quad (27)$$

where ΔL_{mob} represents the mobility induced conductivity change of process (i) and ΔL_{IP} is the ionic product induced conductivity change of process (ii). Equation (27) can be simplified by considering each term separately. First, consider the temperature-dependent mobility term. The temperature derivative of the conductivity is calculated in the previous section and is given in equations (11) and (12). The term in equation (12) involving dC_i/dT is zero because there are no temperature induced changes in ionic concentrations immediately following the laser pulse; or

$$\Delta L_{mob} = \sum_i C_i \frac{d\lambda_i}{dT} \Delta T \qquad (28)$$

Previously described equations for equilibrium ionic concentrations, C_i, ionic mobilities, $\lambda_i(T)$, and the temperature jump, ΔT, are used to determine ΔL_{mob}. Now, consider the second term of equation (27). Replacing $\partial L/\partial C_i$,

$$\Delta L_{IP} = \lambda_{H^+} \Delta C_{H^+} + \lambda_{OH^-} \Delta C_{OH^-} \qquad (29)$$

Since $\Delta C_{H^+} = \Delta C_{OH^-}$

equation (29) becomes

$$\Delta L_{IP} = (\lambda_{H^+} + \lambda_{OH^-})\Delta C_{H^+}. \qquad (29a)$$

Solution of equation (27) gives the concentration of product hydronium ion.

$$[\text{reactive events}] = \Delta C_{H^+} = (\Delta L - \Delta L_{mob})/(\lambda_{H^+} + \lambda_{OH^-}) \qquad (30)$$

Expressions for the ionic mobility of H^+ and OH^- were given previously. Equation (8) and equation (30) are combined in equation (7) to give the quantum yield.

C. Conductivity from signal voltages

The previous treatment uses solution conductivity changes in the data analysis. The transient signal voltages recorded during the experiment must be converted to solution conductivity changes. The conversion is described in this section as follows:

(1) The voltage change at the output of the conductivity monitor is calculated given a small change in conductivity.

(2) This voltage is amplified and the final voltage at the signal averager input is calculated, giving a relationship between cell conductivity changes and recorded voltages.

(3) The solution conductivity change is calculated given an identical small change in cell conductivity.

(4) The relationships are combined to yield the solution conductivity change as a function of recorded voltage change.

(1)

The schematic for the cell amplifier is shown in Figure II-8. At bridge balance, the bias voltage across the illuminated cell, RC2, is

$$V_c = \frac{RC2}{RC2 + R5 + R6} V \tag{31}$$

where V is the 300 V bias battery. The current through the illuminated RC2 arm of the bridge is

$$i_c = V_c/RC2 \tag{32}$$

For small conductivity changes

$$\Delta i_c = \frac{di_c}{d(1/RC2)} \Delta(1/RC2) \tag{33}$$

The derivative

$$\frac{di_c}{d(1/RC2)} = V_c - \frac{VRC2(R5 + R6)}{(RC2 + R5 + R6)^2} \tag{33b}$$

The second term can be neglected for two reasons. First, RC2 is large compared to R5 + R6 so that the second term is only 3-4% of the first term. Also, V_c is fixed by capacitors on the reference side of the bridge. The time constant for a change in V_c is several tens of milliseconds, long compared to the transient signal. Thus,

$$\Delta i_c = V_c \Delta(1/RC2). \tag{33c}$$

The AD507K op amp forces the current differences between the two arms of the bridge through feedback resistor, R7. The voltage change at the conductivity monitor output is

$$\Delta V_{cm} = -V_c R_7 \Delta(1/RC2) \tag{34}$$

(2)

The cell monitor voltage is further amplified before being sent to the signal averager. The final voltage at the signal averager is

$$\Delta V_o = [\text{Gain}]\Delta V_{cm} \tag{35}$$

where [Gain] is the gain of the triggered differential amplifier and low pass filter. Replacing ΔV_{cm} and V_c from equations (34) and (31)

$$\Delta V_o = -\frac{[\text{Gain}]\ RC2\ V(R7)}{(RC2 + R5 + R6)}\ \Delta(1/RC2) \tag{36}$$

(3) and (4)

The solution conductivity is

$$L = \frac{k_{c2}}{RC2} \tag{37}$$

where k_{c2} is the cell constant. For an identical small change in conductance (1/RC2)

$$\Delta L = k_{c2}\ \Delta(1/RC2) \tag{38}$$

Rearranging (36) and $\Delta(1/RC2)$ in (38) gives an expression relating conductivity changes to measured voltage changes:

$$\Delta L = \frac{-k_{c2}\ (RC2 + R5 + R6)\ \Delta V_o}{(RC2)\ [\text{Gain}]\ R7\ V} \tag{39}$$

Numerical values are as follows: $k_{C2} = 0.319\ \mathrm{cm}^{-1}$; RC2 = 5.27 MΩ at 25°C and 110% of theoretical conductivity of pure water; R5 = 115 KΩ, R6 = 7KΩ, Gain = 12.29 with a low pass filter setting of 60 KHz and V = 300 V.

II. Thermal recombination rate

The exponential decay of the conductivity signal following equilibrium perturbation by the laser induced reaction is caused by recombination of the excess H^+ and OH^-. The recombination rate, k_{-1} of equation (2), is obtained from the experimental decay time, τ [21].

$$\frac{1}{\tau} = k_{-1}[C_{H^+} + C_{OH^-}] + k_1 \tag{40}$$

The ionic production rate, k_1, is ignored because it is small compared to the first term (R). The equilibrium constant of equation (23) is used to calculate $C_{H^+} + C_{OH^-}$ when solving for k_{-1}.

III. Discussion of Error

This section describes the sources of both random and systematic error in the quantum yield determination. The error for determinations based on the conductivity jump and conductivity step are discussed first. Since the absorbance based quantum yields are calibrated against the conductivity based quantum yields, they will retain the systematic error of the conductivity based quantum yields. In addition, there is a calibration error and errors in the absorption spectrum not present in the conductivity based quantum yields.

A. Conductivity Based Quantum Yields

There are two sources of systematic error and two sources of random error. The systematic error comes from cell constant uncertainty and from errors in the expressions used for temperature-dependent ionic conductivities and the water equilibrium constant. The random error comes from statistical uncertainty in the peak conductivity and in the baseline step increase. The magnitude of each of these errors will be determined by estimating its contribution to the peak and step voltages used in the quantum yield calculation.

Error estimation requires knowing the sources of the conductivity signal. The lower arrow in curve C of Figure III-1 indicates the contribution to the conductivity peak from the temperature-dependent mobility of H^+ and OH^- and of Na^+ and Cl^-. In H_2O near 25°C with a D.C. conductivity 10% greater than for ionically pure water, the arrow is located 0.31 times the baseline step. The remaining 0.69 of the baseline step comes from H^+ and OH^- equilibrium relaxation. Of the (0.31) (step) increase, 11.5% is from the temperature-dependence of the Na^+ and Cl^- ionic conductivity and 88.5% is from the temperature

Figure III-1

Transient conductivity signals at 16670 (A), 11740 (B), and 8440 cm^{-1} (C). The initial baseline for each signal is given by the dotted line (....). The conductivity jump extrapolated to the time of the laser pulse is shown with an arrow (→). The calculated jump for a quantum yield of zero is shown with an arrow (←).

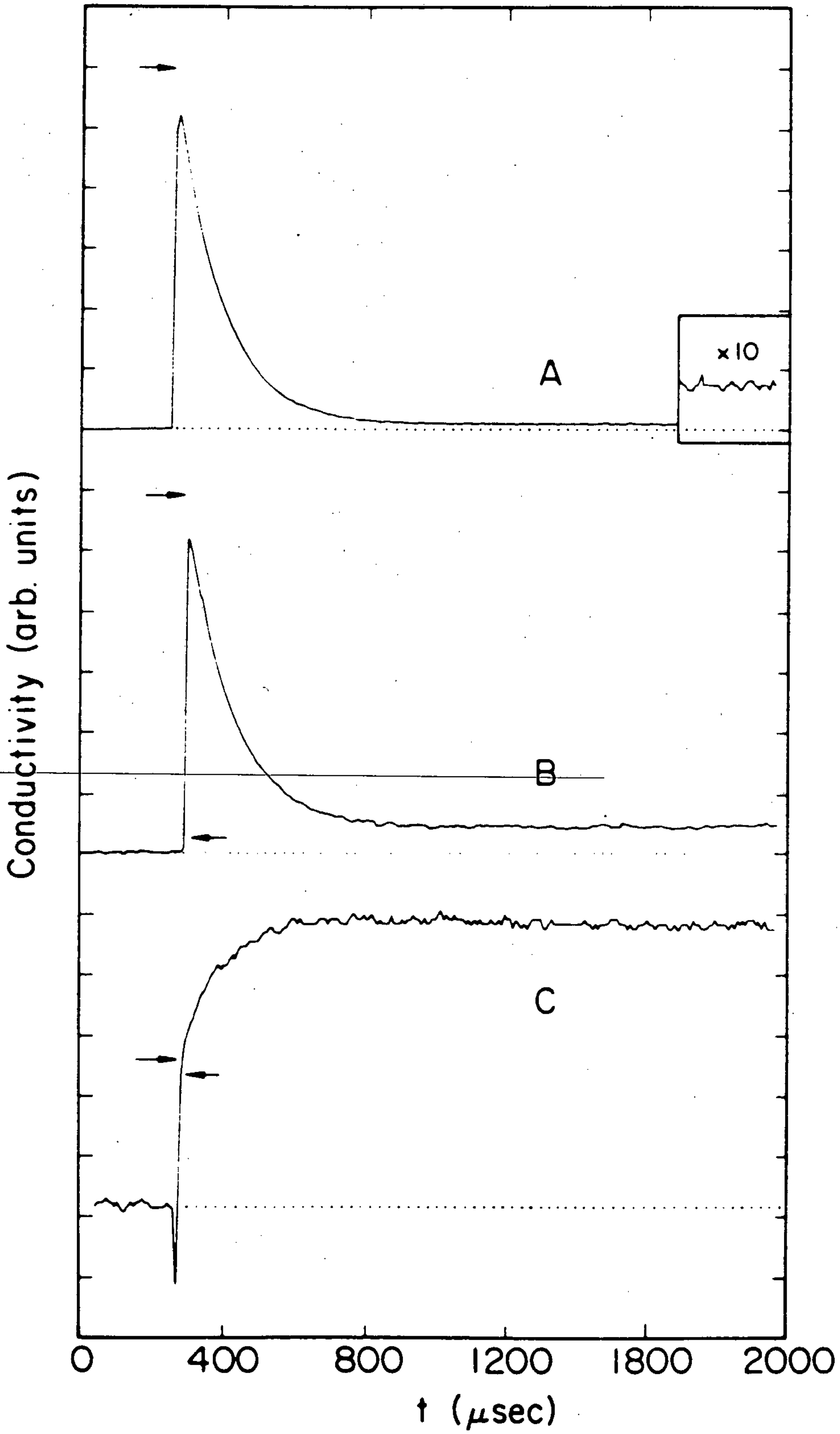

XBL 829-11422

dependence of the H^+ and OH^- ionic conductivity. These ratios hold with an accuracy of ± 2% for D_2O as well.

First, uncertainty in the position of the arrow is considered. The source of this uncertainty is uncertainty in the temperature derivative of the ionic conductivity. The maximum systematic error caused by uncertainty in the temperature derivative of ionic conductivities is estimated[22] to be 15% for H^+ and OH^- [23] and 15% for Na^+ and Cl^- [24]. The uncertainty in the temperature derivative of K_w is $< 2\%$. The total maximum error in the calculated photon concentration is then

$$(0.7)(0.02) + (0.3)(0.15) \approx 6\%.$$

The total fractional error in the calculated contribution of the laser-induced ionization to the peak conductivity caused by an error in the position of the arrow is dependent on the relative magnitude of the peak and step. The approximate expression is

$$\frac{(0.15)[(0.3)\text{ step}]}{\text{peak} - [(0.3)\text{ step}]}$$

Thus the total error is excitation energy dependent. The maximum absolute error in the quantum yield is zero when the peak ≈ to the step ($\phi \approx 2 \times 10^{-7}$ in H_2O), because the peak error and the step error cancel. The total ϕ error at 1.06 μ is about 2%. When the conductivity signal looks like curve A in Figure III-1, the error in the peak is insignificant and the baseline step error dominates, giving a total quantum yield error of 6%.

The relative error for intermediate hydrogen mole fractions or as a function of temperature is the same.

Another source of systematic error is uncertainty in the cell constant of the conductivity cell. An error in cell constant produces an error in the measured concentration of impurity ions and therefore an error in the calculated position of the arrow indicating the temperature-induced conductivity jump. Consider H_2O near 25°C with a D.C. conductivity from impurities 10% greater than from H^+ and OH^-. A 20% error in cell constant will triple the measured Na^+ and Cl^- concentration and triple its contribution to the transient conductivity. It will change the position of the calculated arrow from 0.31 (step) to 0.35 (step), a less than 2% error in the peak at 1.06 μ and a 7% error in the number of absorbed photons, for a net 5% quantum yield error. The wavelength dependence is identical to that already described. The relative error as a function of hydrogen mole fraction is nearly zero. The maximum combined systematic error from a 20% cell constant error and from ionic conductivity uncertainty is about 7% at 1.06 μ.

There are also two sources of random error. There are statistical baseline errors and statistical peak errors. The statistical peak errors are typically about 4% of the distance above the final baseline, independent of absolute peak height. The statistical baseline step uncertainty is about 1×10^{-3} V for a low pass filter setting of 0.06 MHz, with 1280 shots averaged at each polarity.

Table III-1

hydrogen mole fraction	statistical baseline uncertainty
0.00567	20%
0.0174	20%
0.038	15%
0.153	10%
0.3179	5%
1.0	< 2%

Table III-1 shows the estimated statistical baseline step error for data at 1.06 μm as a function of hydrogen mole fraction. The statistical peak error exceeds the baseline error for 1.06 μm excitation at a hydrogen mole fraction > 0.4.

B. Absorbance based quantum yields

Quantum yields based on the absorption spectra are not dependent on the baseline step increase. Thus, statistical baseline error is eliminated. Systematic and random uncertainty from the zero absorbance point of the spectrometer and pen reproducibility is added. After the zero absorbance point is set, measured absorbances at 650 nm differ from those of Tam and Patel[19] at 650 nm by about 0.00016. Their stated absolute accuracy is about 0.00014. The pure D_2O measurement differs by about 0.0005 cm^{-1}. Therefore, an absolute accuracy of 0.0005 cm^{-1} is assumed. In addition, a statistical uncertainty of about 0.0005 cm^{-1} is found for the spectrometer pen position. Table III-2 shows the systematic and random error from uncertainty in the absorption spectrum at an excitation wavelength of 1.06 μm.

Comparison of absorbance based and conductivity step based quantum yields at 1.06 μm for hydrogen mole fractions between 0.15 and 0.32 shows agreement within about 10%.

Table III-2

mole fraction hydrogen	Quantum yield error from absorbance uncertainty statistical	 systematic
D_2O	12.5%	12.5%
0.0174	9%	9%
0.038	7%	7%
0.1108	4%	4%
0.198	2.7%	2.7%

Analysis references

1. N.S. Osborne, H.F. Stimson, and D.C. Ginnings, J. Res. Natl. Bur. Std. 23, 197 (1939).
2. R.C. Weast, ed., "Handbook of Chemistry and Physics", 53rd edition, CRC Press, Cleveland (1972) p. F-4.
3. I. Kirshenbaum, "Physical Properties and Analysis of Heavy Water", McGraw-Hill, New York (1951).
4. J. O'M. Bockris, "Modern Electrochemistry", v.l, p 471 Plenum, New York (1970).
5. G.S. Kell in "Water: A Comprehensive Treatise", Vol. 1, edited by F. Franks, Plenum Press, New York (1972) p. 407.
6. R.C. Hardy and R.L. Cottingham, J. Chem. Phys., 17, 509 (1949).
7. V.A. Giere, Z. Naturforschung, 5a, 581 (1950).
8. David Goodall, private communication.
9. A.S. Quist and W.L. Marshall, J. Phys. Chem., 69, 2984 (1965).
10. K.N. Marsh and R.H. Stokes, Aust. J. Chem., 17, 740 (1964).
11. R.A. Robinson and R.H. Stokes, "Electrolyte Solutions", Butterworth (1959).
12. M. Nakahara, N. Takisawa, and J. Osugi, J. Phys. Chem., 85, 112 (1981).

13. B.B. Owen and F.H. Sweeton, J. Am. Chem. Soc., 63, 2811 (1941).

14. W.J. Albery in "Proton Transfer Reactions", edited by E.F. Caldin and V. Gold, Chapman and Hall, London (1975) p. 263.

15. H.S. Harned and R.A. Robinson, Trans. Faraday Soc., 36, 973 (1940).

16. Th. Ackermann, Z. Elektrochem., 62, 411 (1958).

17. A.K. Covington, R.A. Robinson, and R.G. Bates, J. Phys. Chem., 70, 3820 (1966).

18.. V. Gold and B.M. Lowe, J. Chem. Soc. (A), 936 (1967).

19. A.C. Tam and C.K.N. Patel, Applied Optics, 18, 3348 (1979).

20. S.A. Sullivan, J. Opt. Soc. Am., 53, 962 (1963).

21. M. Eigen, W. Kruse, G. Maass, and L. De Maeyer, Progr. Reaction Kinetics, 2, 285 (1964).

22. The error in the slope given a deviation from a curve y(x) over a range in x and y of R_x and R_y, respectively, is taken to be (4)(deviation of y)/R_y

23. Using footnote 22: 4(0.04)(650)/700 = 15% for a 4% deviation and a range of ionic mobilities of 700 cm^2 ohm^{-1} equivalent.

24. Using footnote 22: 4(0.02)(135)/70 = 15% for a 2% deviation and a range of ionic mobilities of 70 cm^2 ohm^{-1} equivalent.

CHAPTER IV. RESULTS

Results are presented in two parts. The first part presents quantum yields of the laser-induced reaction. The second part presents thermal recombination rates.

I. Laser-induced Reaction

Quantum yields for the laser-induced reaction are presented as a function of fluence, photon energy, temperature, and mole fraction hydrogen. The reader should keep in mind that as the mole fraction of hydrogen is increased from 0 to 1.0, the composition of the solution changes approximately as in Equation (20) of the analysis section. Most hydrogen is in the form HOD at low hydrogen mole fractions.

The initial transient voltage as a function of laser pulse energy or fluence is shown in Figures IV-1 and IV-2. Figure IV-1 shows results for H_2O at 10°C. The initial transient voltage is proportional to the quantum yield. The dependence is linear in pulse energy over a factor of twenty at 12,500 cm^{-1} and a factor of fifty at 16,670 cm^{-1}. Figure IV-2 shows results for 0.12 X_H, the mole fraction of hydrogen in D_2O. The initial peak height is linear in the pulse energy over a factor of twenty for excitation at 16500 cm^{-1}. The absolute peak magnitude for excitation at 11802 cm^{-1} in 0.0057 mole fraction hydrogen in D_2O is 60 to 70 times smaller than for pure H_2O. The reduction is caused by a lower overtone absorption (x 1/20), lower

Figure IV-1

The dependence of quantum yield on fluence in H_2O near 10°C. Normalized initial transient voltage ($\Delta V/\Delta V_m$) as a function of normalized pulse energy (E/E_m); (□) data at 16670 cm^{-1} where ΔV_m is 0.525 ± 0.015 V and E_m is 11.5 ± 0.1 mJ; (Δ) data at 12500 cm^{-1} where ΔV_m is 0.144 ± 0.008V and E_m is 2.02 ± 0.05mJ. The solid lines represent the behavior expected for a single-photon process. 10 mJ corresponds to an intensity of 50 ± 25 MW cm^{-2} and a fluence of 0.4 ± 0.2 J cm^{-2}.

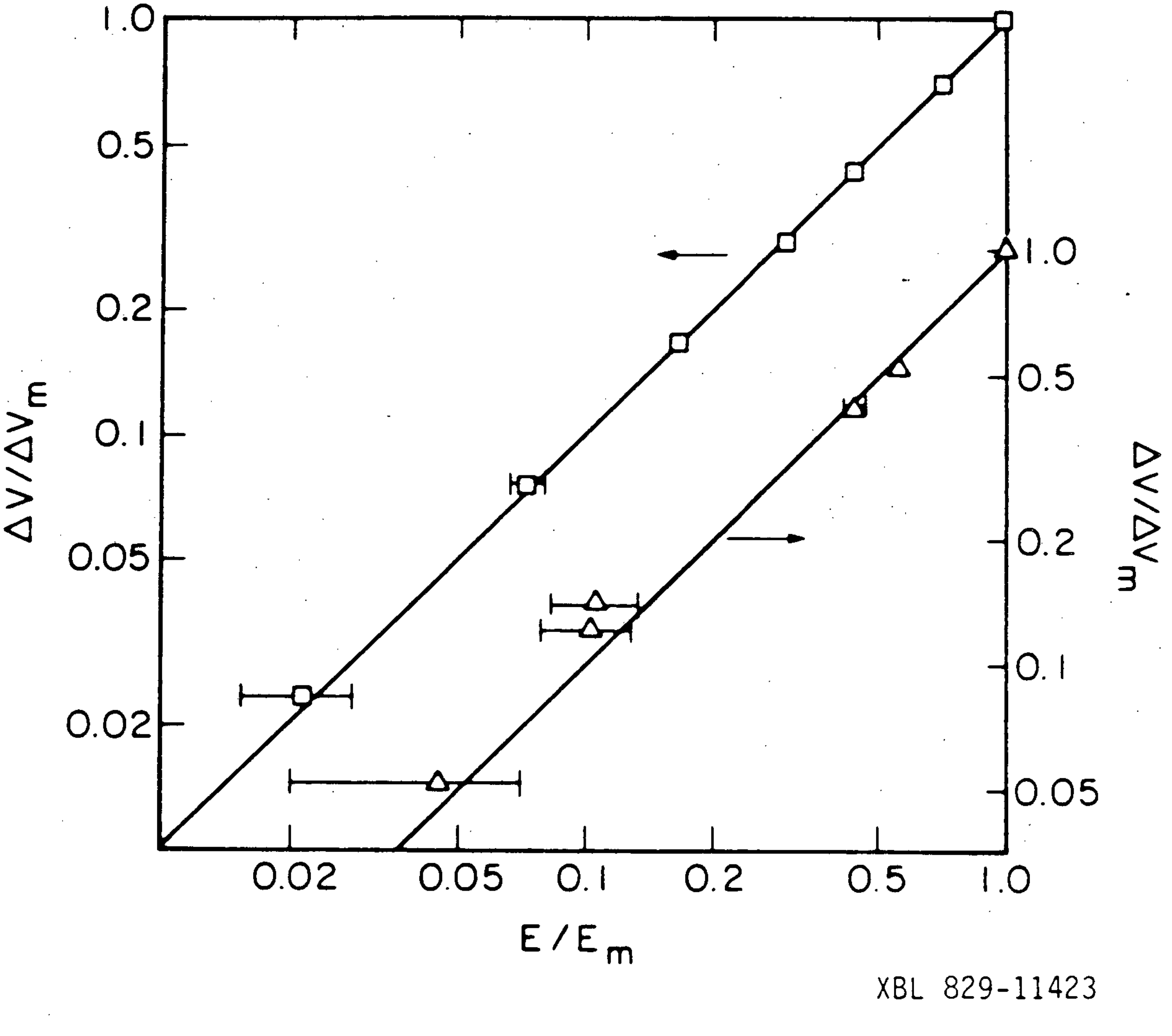

XBL 829-11423

Figure IV-2

The dependence of the quantum yield on fluence is shown. The normalized initial transient voltage $\Delta V/\Delta V_m$ as a function of the normalized pulse energy E/E_m. (●) represents data for 0.12 mole fraction hydrogen in D_2O. The temperature is 24°C. The photon energy is 16,500 cm^{-1}. ΔV_m is 0.023 V and E_m is 9.2 mJ.

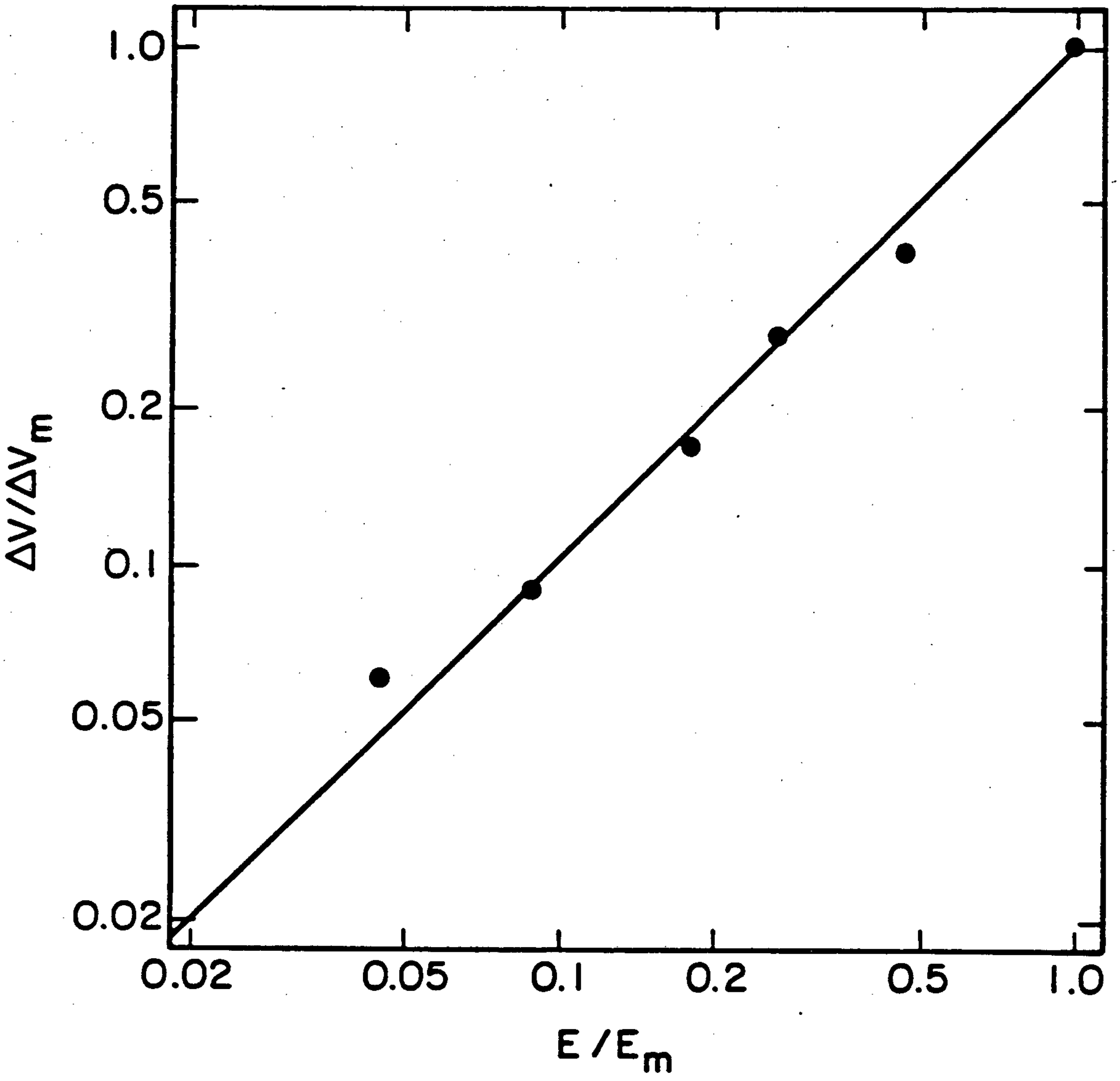

XBL 831-7701

product ion mobilities (x 1/1.5), and a lower quantum yield (x 1/2) in D_2O.

The photon energy dependence of the quantum yield between 8000 cm^{-1} and 17,000 cm^{-1} is shown for H_2O and 0.12 X_H; 0.512 X_H, 0.406 X_H, 0.318 X_H; and less than 0.017 X_H in Figures IV-3, IV-4, and IV-5.

The absorption bands in this wavelength range correspond to O-H or O-D stretching overtones or to stretch plus bend combinations. For H_2O, the departure from a smooth increase of ϕ with ν is outside the limits of experimental error. The most striking feature of Figure IV-3 is that superimposed on the trend of increasing ϕ with increasing ν noted in reference 1 is a pattern which correlates with the absorption spectrum. The quantum yield rises rapidly on the low-frequency side of a band and is relatively constant through the band center and high-frequency wing.

No qualitative difference in behavior is seen between bands involving pure stretching excitation and those involving combination with bending vibrations. A small hump in the quantum yield at the $3\nu_s + \nu_b$ overtone is present.

In the wavelength range shown, the absorption strength of a D_2O molecule is more than an order of magnitude smaller than for an H_2O or HOD molecule. This means that at 0.12 X_H, mole fraction of hydrogen added to D_2O, the absorption spectrum is roughly proportional to that of H_2O as shown in

Figure IV-3

Quantum yield (ϕ) as a function of photon energy (ν) for 0.12 mole fraction hydrogen in D_2O at 24 ± 1°C, (●). Quantum yield for photoionization of H_2O at 10 ± 1°C, (○) as a function of photon energy (ν). A line is drawn through experimental points. Estimated errors are shown for H_2O. For 0.12 mole fraction hydrogen, Log(ϕ) has a 10% random uncertainty at 9400 cm^{-1}, 15% near 11100 cm^{-1}, and 35% near 12200 cm^{-1}. The absorption spectrum of H_2O is shown as the dependence of the natural absorption coefficient (α) on wavenumber (ν). [$I/I_o = \exp(\alpha l)$.] Band assignments shown (ref. 2-4) with subscripts b and s representing bending and stretching modes, respectively.

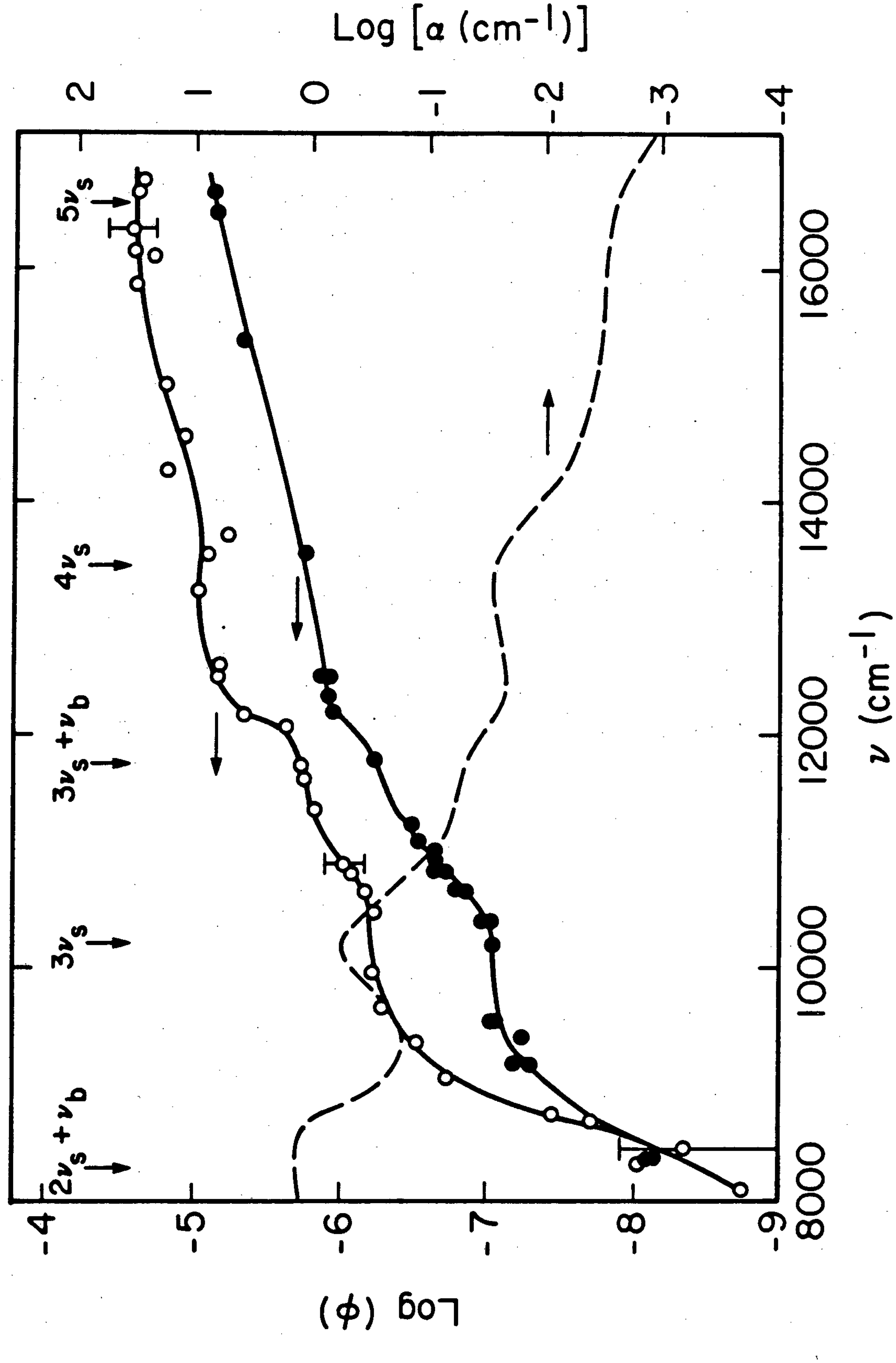

Log [α (cm⁻¹)]
2
1
0
-1
-2
-3
-4
Log (φ)
-4
-5
-6
-7
-8
-9
ν (cm⁻¹)
8000
10000
12000
14000
16000
2ν_s + ν_b
3ν_s
3ν_s + ν_b
4ν_s
5ν_s

XBL 831-7716

Figure IV-4

Quantum yield as a function of photon energy for photoionization of several mole fractions of hydrogen in D_2O. Experimental points for successive mole fractions are displaced upward by one unit. The bottom of the graph represents $\log_{10}(\phi) = -8$, -9, and -10 for $X_H = 0.512$ (X), 0.406 (●), and 0.318 (O), respectively. The vertical scale is +1decade/division. The solid line has the same shape as the quantum yield for H_2O, but is displaced to overlay the experimental points. Random error varies from about 7% at 9400 cm^{-1} to 17% at 12200 cm^{-1}.

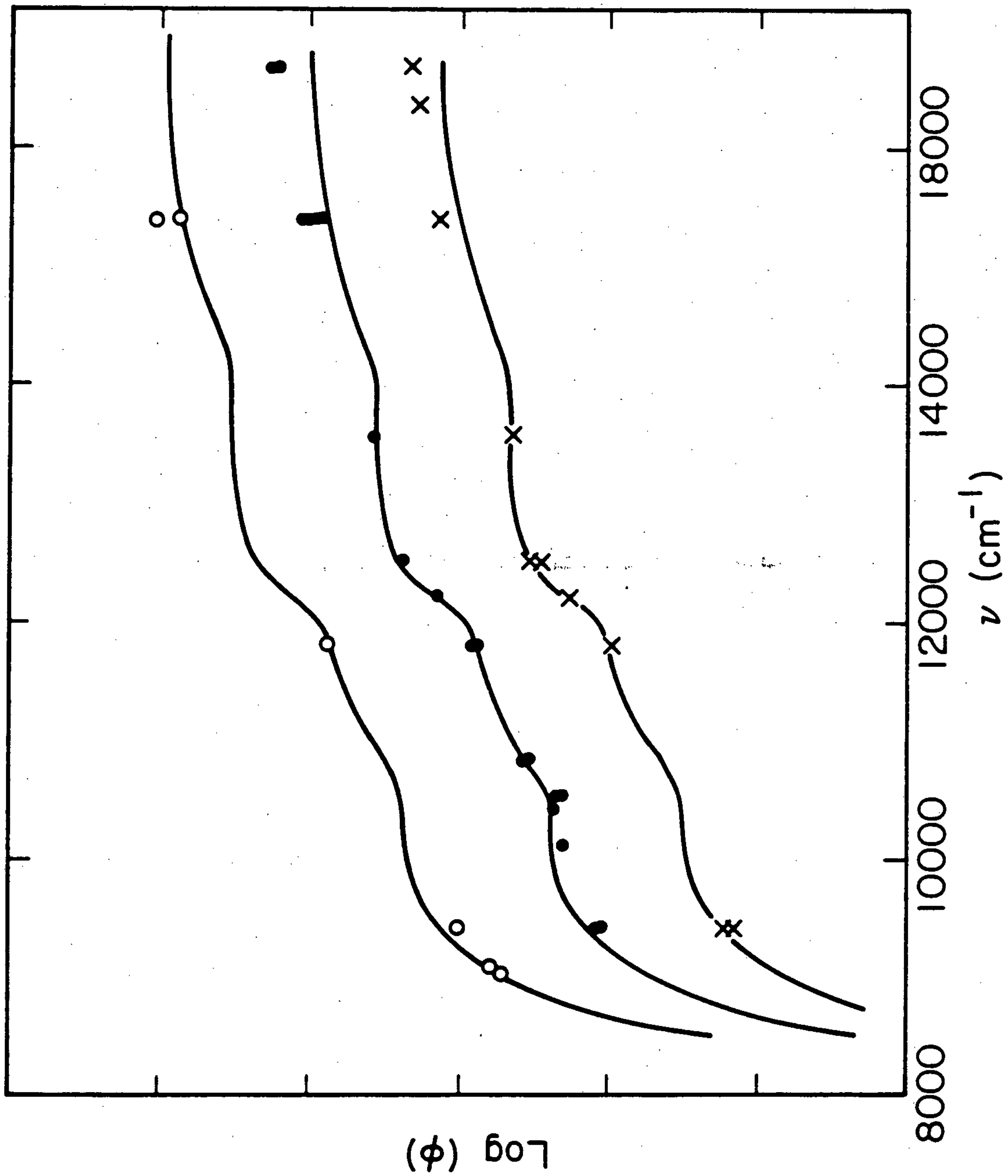

XBL 831-7713

Figure IV-5

Quantum yield (ϕ) as a function of photon energy (ν) in predominantly D_2O. The mole fraction of hydrogen is $X_H \leq 0.017$. The relative error can be estimated from points shown in the figure.

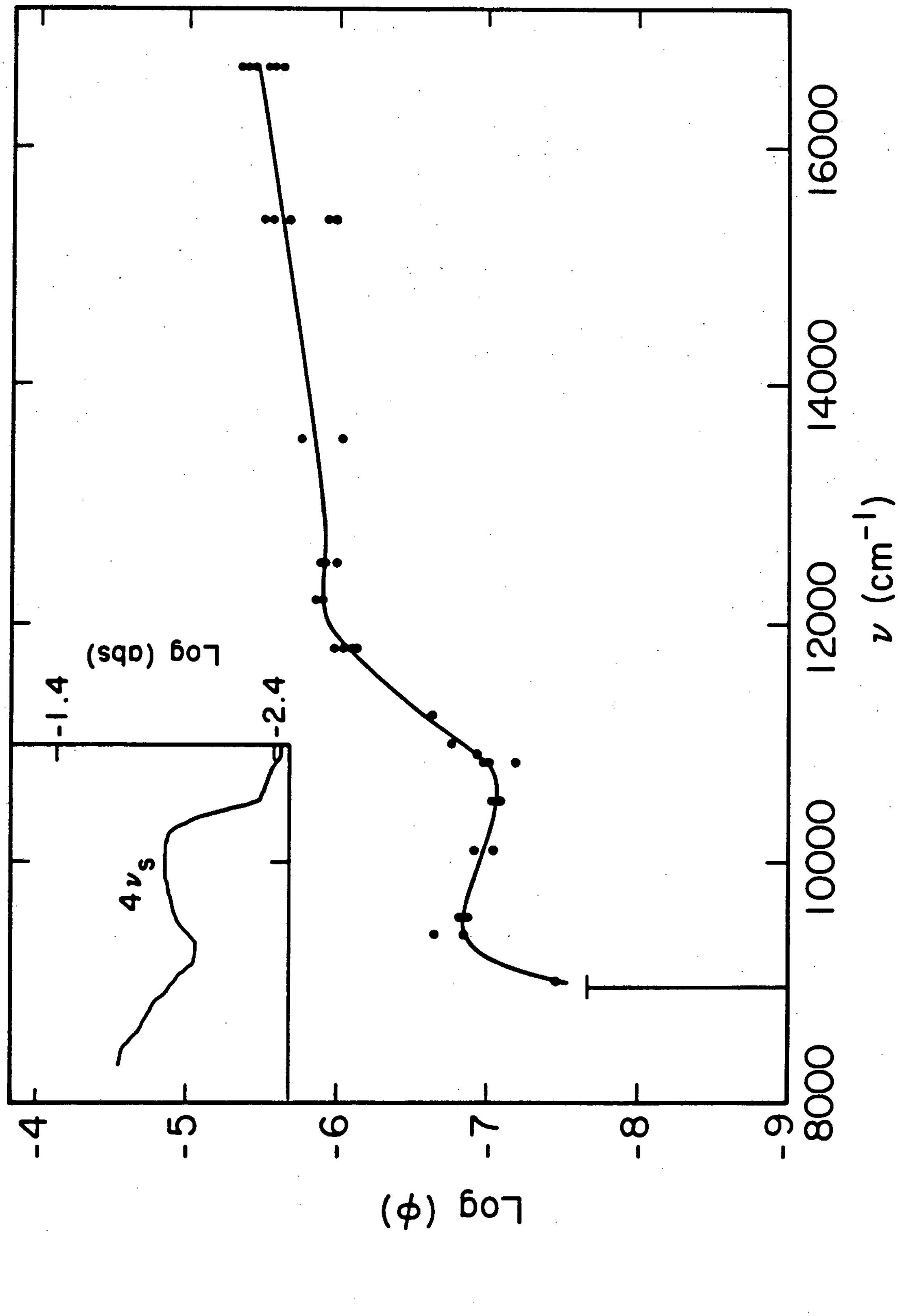
Log (φ)
-4
-5
-6
-7
-8
-9
8000
10000
12000
14000
16000
ν (cm⁻¹)
Log (abs)
-1.4
-2.4
4ν_s
XBL 831-7722

Figure II-13. The quantum yield of the $X_H = 0.12$ mixture is shaped like the H_2O quantum yield, but is displaced to lower yields. The quantum yields for higher hydrogen mole fractions, Figure IV-4, show behavior similar to $X_H = 0.12$.

Figure IV-5 shows the quantum yield along with the absorption spectrum near the $v = 4$, O-D stretch in nearly pure D_2O, $X_H < 0.017$. At this composition, the absorption is mostly by D_2O molecules. The quantum yield rises sharply on the red side of the $v = 4$, O-D stretch overtone absorption, then declines through the center of the band. It goes through a minimum on the blue side of the band, then rises as higher overtones begin contributing to the absorption. Additional structure in the quantum yield or the absorption spectrum from higher overtones is not resolved.

The first observable quantum yield is from excitation of the $v = 3$ O-H stretch in H_2O at 10250 cm^{-1} and the $v = 4$ O-D stretch in D_2O at 9000 cm^{-1}. There is no known feature in the absorption spectrum of isotopic mixtures at energies higher than 8000 cm^{-1} enabling selective excitation of either HOD or D_2O. However, for dilute H_2O in D_2O, a band centered at 7168 cm^{-1} is attributed to the overtone of the O-H stretch of HOD molecules.[5,6] D_2O absorption is small. Excitation of this feature at 7072 cm^{-1} in 0.038 X_H did not produce an observable laser-induced reaction.

Figure IV-6 shows the temperature dependence of the quantum yield for five excitation wavelengths in H_2O. The

Figure IV-6

H_2O quantum yield as a function of temperature for excitation of four quanta of O-H stretch; (Δ) 13570 cm^{-1}, (X) 12484 cm^{-1}; three quanta of stretch plus one bend, (O) 11737; or three quanta of stretch, (+) 10065 cm^{-1}, (●) 9399 cm^{-1}. The quantum yields at each wavelength are normalized by the quantum yield at 0°C, ϕ (T = 0). Random error is approximately 10% for excitation of v = 3, and 15% for excitation of v = 4.

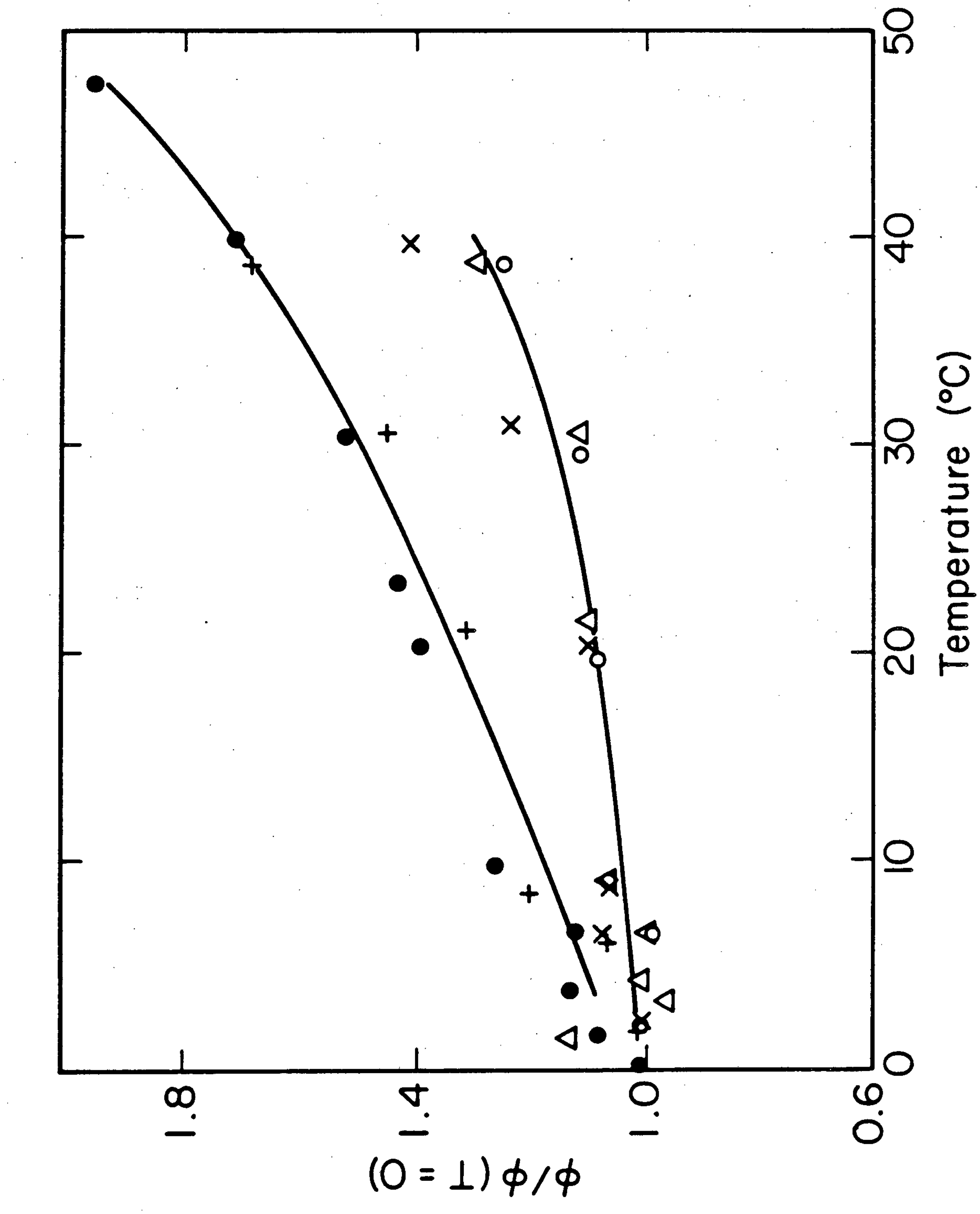

XBL 831-7719

quantum yield increases as temperature increases. The fractional increase is smaller with a higher photon energy. As temperature goes from 0 to 40°C, the quantum yield increase is a factor of 1.7 for three quanta of OH stretch and a factor of 1.3 for three quanta of stretch plus one bend or for four quanta of OH stretch. Figure IV-7 shows the temperature dependence of the quantum yield for nearly pure D_2O; $X_H = 0.017$, for excitation at 9400 cm^{-1}. The yield increases a factor of 1.8 from 0°C to 40°C, almost identical to the behavior of H_2O.

The structure of liquid water becomes more ordered as the temperature is reduced below 4°C[7]. Measurements at 9400 cm^{-1} show no change from the general decline of ϕ with decreasing temperature as the temperature is reduced below 4°C.

The dependence of the quantum yield on hydrogen mole fraction is shown in Figure IV-8 for excitation at 11800 cm^{-1} and 9400 cm^{-1} and in Figure IV-9 for excitation at 15380 cm^{-1}. Figure IV-8 shows a 2.5 times larger quantum yield for H_2O than for D_2O. However, the increase in quantum yield is not monotonic with increasing hydrogen mole fraction. A quantum yield minimum occurs for about a 0.2 hydrogen mole fraction. Figure IV-10 shows 9400 wavenumber conductivity curves recorded at 0.0174, 0.15, 0.60, 0.81, and 1.0 mole fraction hydrogen. Figure IV-9 shows an eleven times larger quantum yield for H_2O than for D_2O at 15380 cm^{-1}. The increase with greater hydrogen mole fraction is monotonic.

Figure IV-7

The quantum yield of nearly pure D_2O, $X_H = 0.0174$, as a function of temperature for excitation of four quanta of O-D stretch at 9400 cm^{-1}. The quantum yield is normalized by the quantum yield at 0°C, ϕ (T = 0).

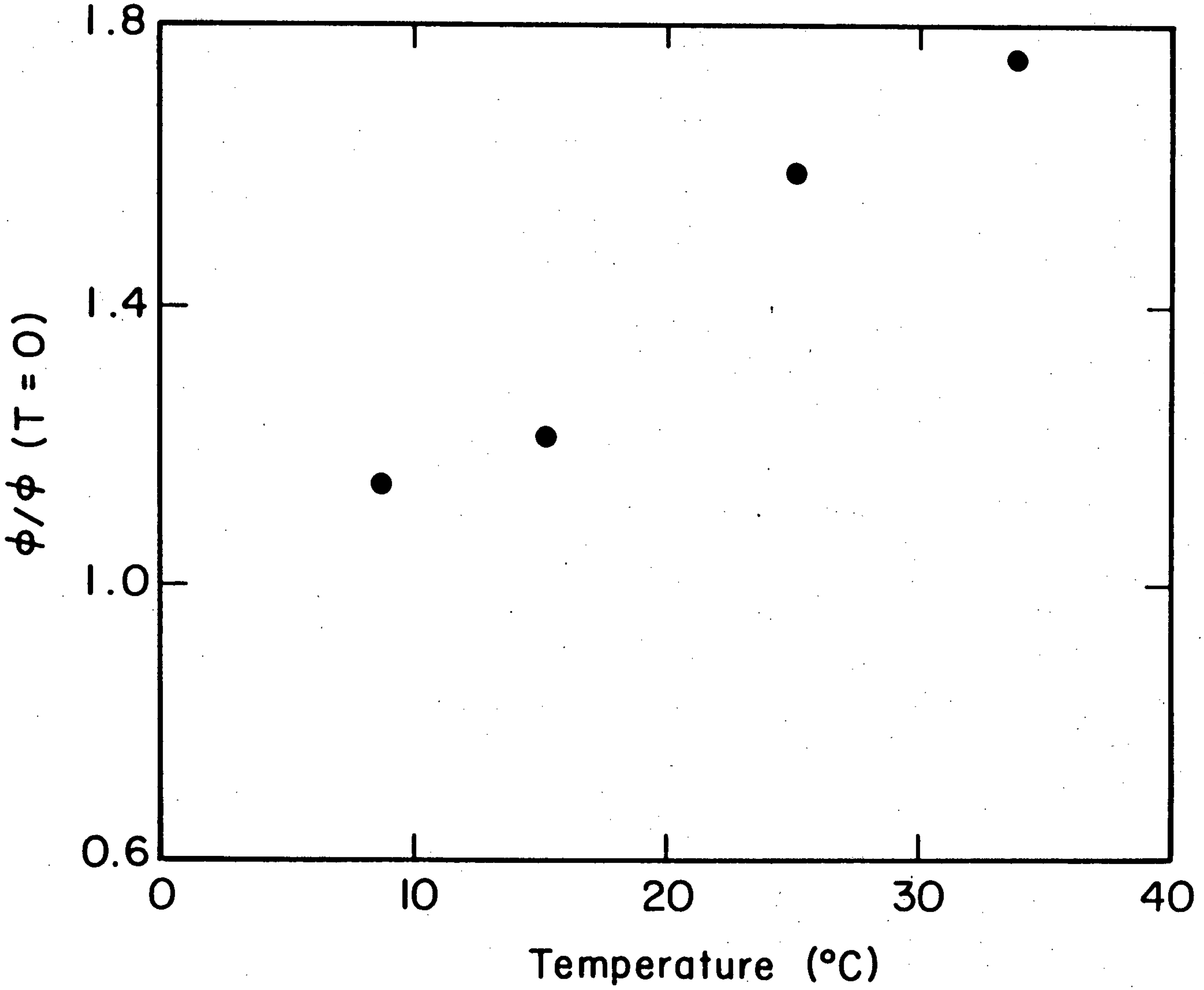

XBL 831-7724

Figure IV-8

The dependence of the quantum yield (ϕ) on hydrogen mole fraction for excitation at 9400 cm^{-1} at 25 ± 1°C (+) and 11800 cm^{-1} at 24.5 ± 1°C (O). The quantum yield is normalized by the quantum yield in pure D_2O at the excitation wavelength, ϕ (D_2O). The values of $\phi(D_2O)$ are 1.93×10^{-7} at 9400 cm^{-1} and 8.12×10^{-7} at 11800 cm^{-1}. The solid curve is a fit to the form of

$$\phi = \sum_i \varepsilon_i c_i \ell \, \phi_i / \sum_i \varepsilon_i c_i \ell$$

where i represents H_2O, HDO, or D_2O and $\varepsilon_i c_i \ell$ is the absorbance of species i. At 9400 cm^{-1}, the best fit is with $\phi_{H_2O} = 3.81 \times 10^{-7}$, $\phi_{HOD} = 2 \times 10^{-9}$, and ϕ_{D_2O} 2.54×10^{-7}. At 11800 cm^{-1}, $\phi_{H_2O} = 1.037 \times 10^{-6}$, $\phi_{HOD} = 2.62 \times 10^{-7}$, $\phi_{H_2O} = 1.69 \times 10^{-6}$. Estimated uncertainty at 9400 cm^{-1} is shown in Table III-2. Estimated uncertainty at 11800 cm^{-1} is approximately three times the values in Table III-2.

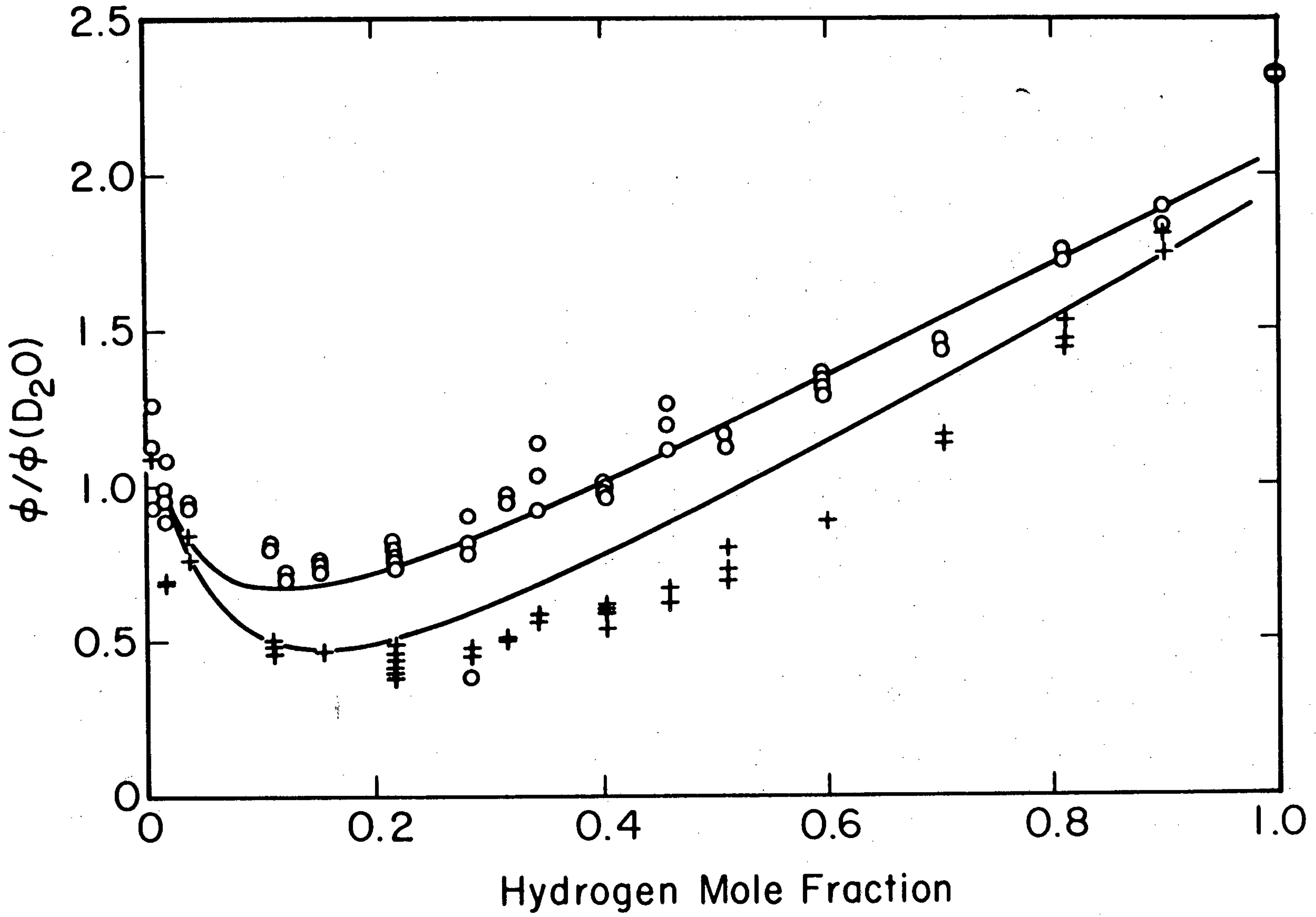
2.5
2.0
1.5
1.0
0.5
0
$\phi/\phi(D_2O)$
0
0.2
0.4
0.6
0.8
1.0
Hydrogen Mole Fraction

XBL 831-7720

Figure IV-9

The dependence of the quantum yield (ϕ) on hydrogen mole fraction for excitation at 15380 cm^{-1}. The quantum yield is normalized by the quantum yield in pure D_2O, ϕ (D_2O).

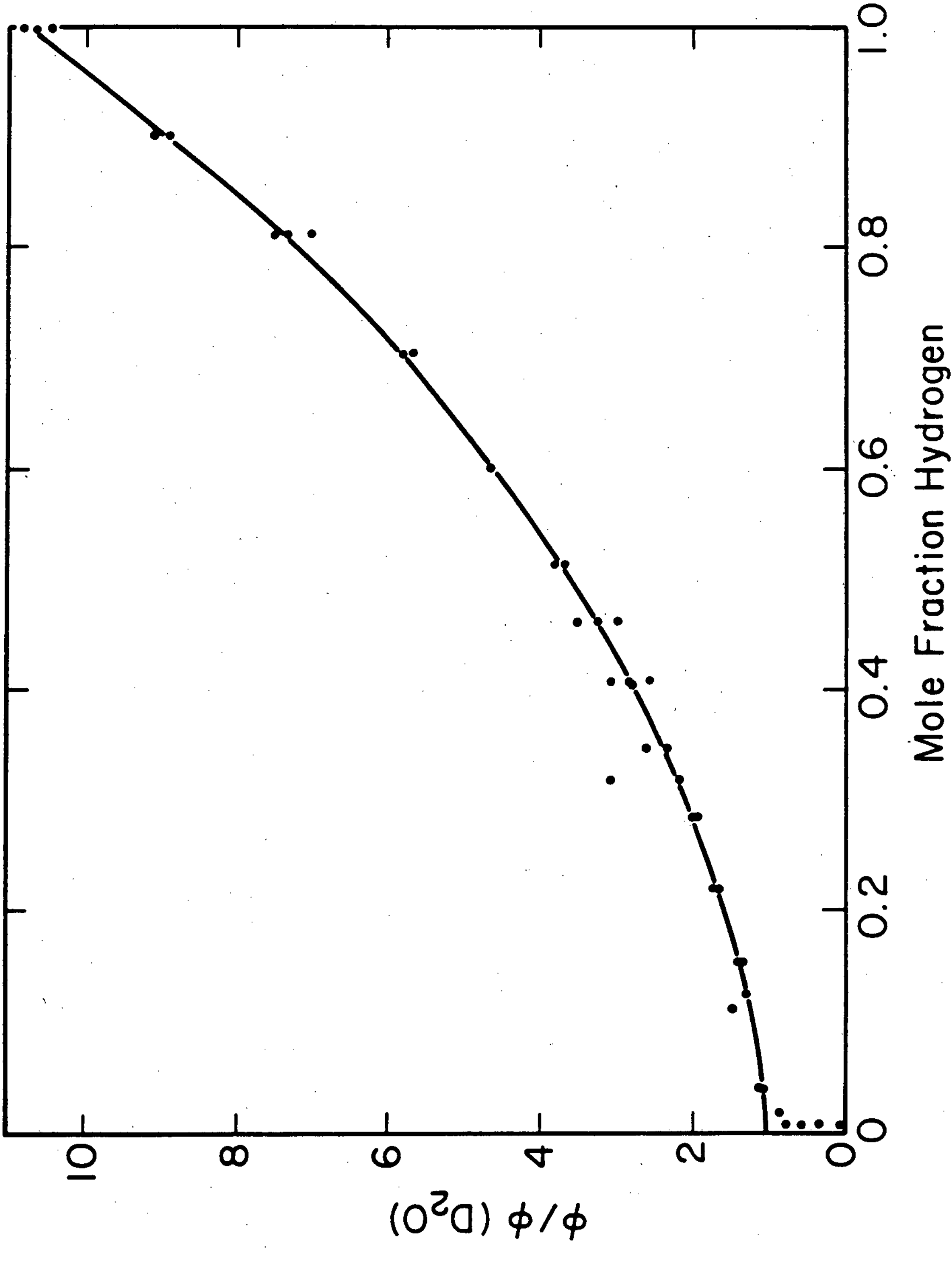

XBL 831-7721

Figure IV-10

Experimental transient conductivity curves for several hydrogen mole fractions. Excitation is 9400 cm^{-1} and temperature, 25°C. The peak amplitude is scaled to equal 1. A larger baseline step denotes a lower quantum yield, to a first approximation. Curve A has the lowest quantum yield and curve E the greatest quantum yield. Curve A (0.15 X_H), B (0.60 X_H), C (0.81 X_H), D (0.0174 X_H), and E (1.0 X_H).

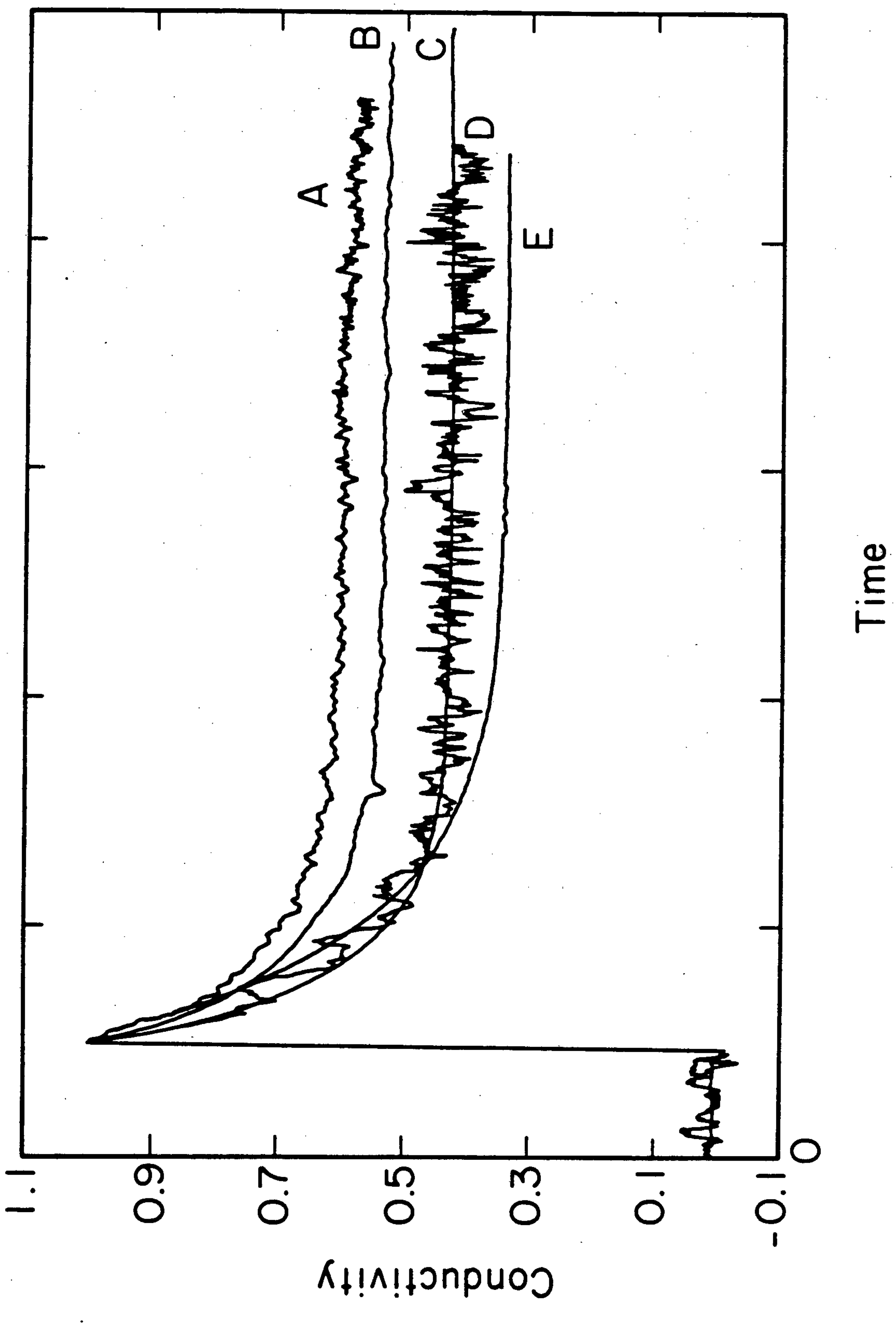

XBL 831-7725

The apparent decline in quantum yield for the point with highest deuterium enrichment is not outside the combined experimental error for conductivity peak height and spectral absorbance. If the true absorbance of D_2O were lower than used in the quantum yield calculation, then the first two or three points in Figure IV-9 would have a higher position. Two factors could produce excess absorbance in the reported D_2O absorbances[8]; H_2O contamination, or organic contaminants in the feedstock D_2O.

II. Thermal Recombination Reaction

This section presents the thermal recombination rate as a function of temperature and isotopic composition. Figure IV-11 shows the temperature dependence of the rate in H_2O and in D_2O. An Arrhenius plot, in Figure IV-12 gives $k = 3.94 \times 10^{13} \exp(-3.49/RT)$. In H_2O, the Arrhenius rate increases from 6.37×10^{10} L/mol s at 0°C to 1.72×10^{11} L/mol s at 50°C. The rate at 25°C is 1.09×10^{11} L/mol s. The Arrhenius line lies slightly below the average of the experimental points at 1.12×10^{11} L/mol s. D_2O results are not as accurate due to lower signal amplitudes and fewer measurements. A normal isotope effect is observed with the rate for hydrogen greater than the rate for deuterium. The rate in X_H = 0.017 D_2O at 25°C is 7.07×10^{10} L/mol s. Table IV-1

Figure IV-11

Thermal ionic recombination rate as a function of temperature for H_2O (●) and D_2O (x).

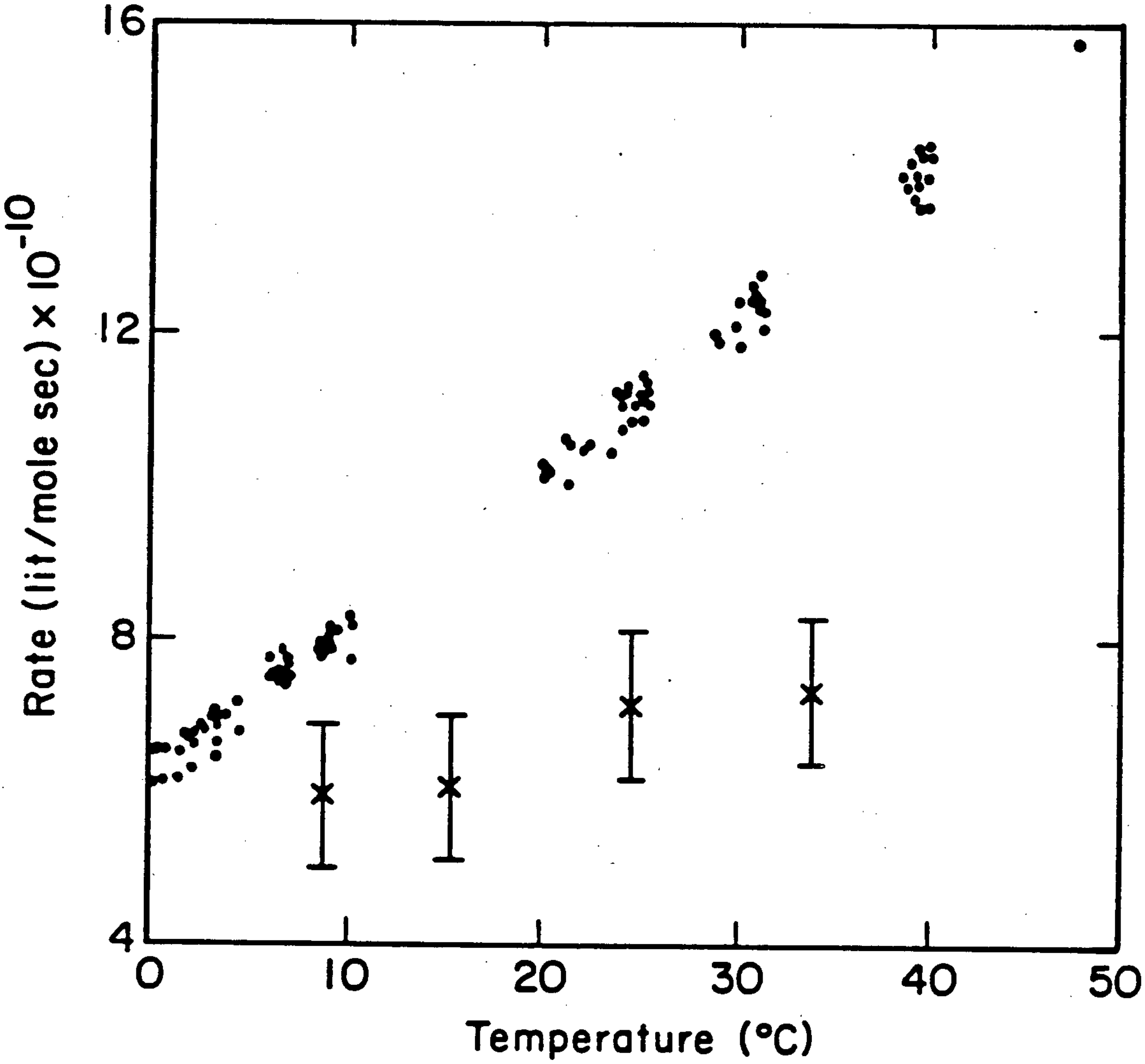

XBL 831-7702

Figure IV-12

Arrhenius plot of ln(k) vs 1000/T for the thermal recombination. The solid line (—) is a least squares fit of this data (.). The dashed line (--) is a comparison with reference 9, the points (Δ) are from reference 10. The point (O) is from reference 11, the point (X) from reference 12, and the point (+) from reference 1.

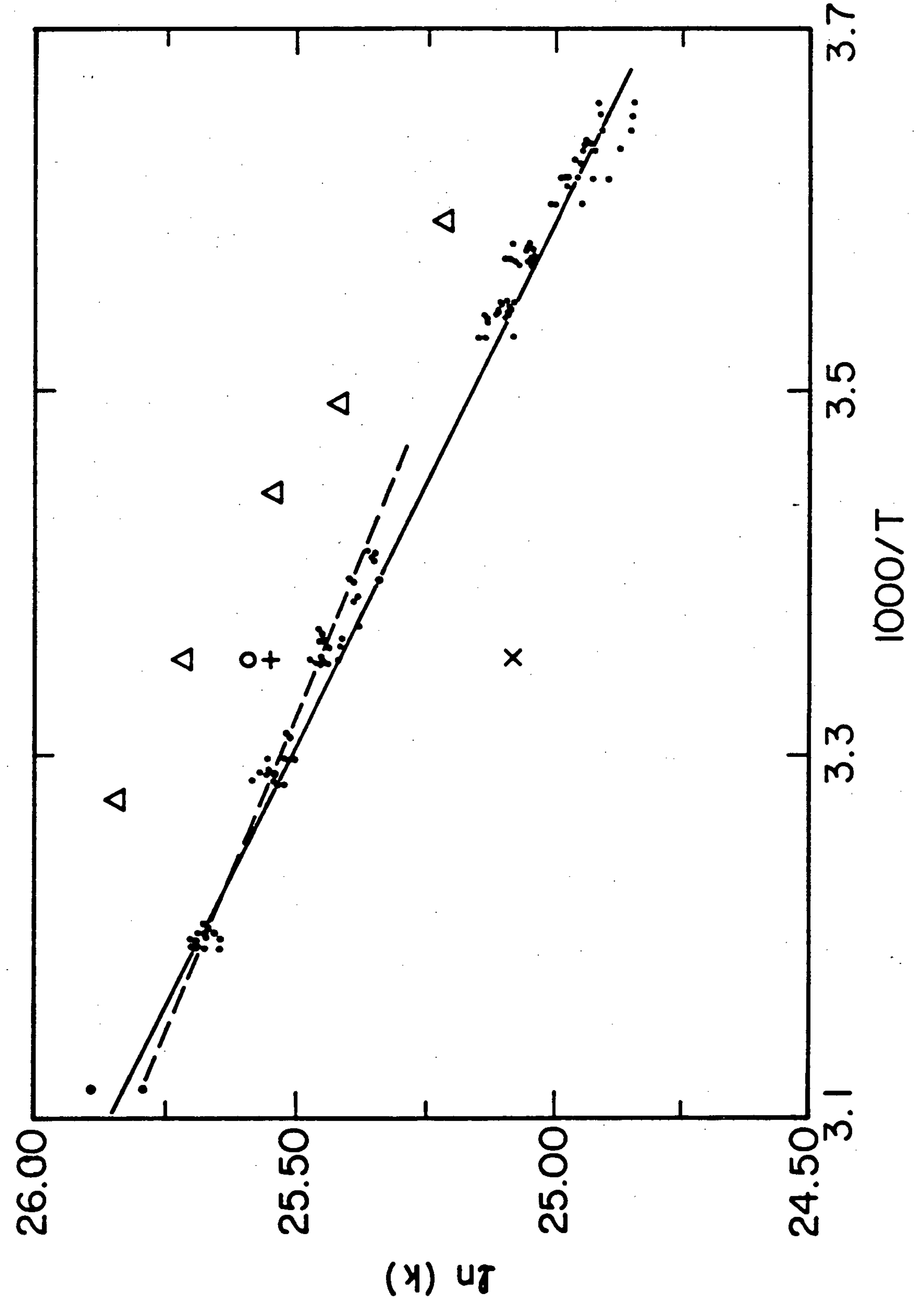
26.00
25.50
25.00
24.50
ln (k)
3.1
3.3
3.5
3.7
1000/T

Table IV-1

Table of recombination rate, relaxation time, and recombination distances in H_2O and D_2O

	recombination rate (L/mol s)	relaxation time (μs)	recombination distance (Å)
H_2O			
Ertl and Gerischer[a]	1.46×10^{11}	34	9.2
Eigen and DeMaeyer[b]	1.3×10^{11}	37	8.03
Barker *et al.*[c]	1.12×10^{11}	44	5.85
This work[d]	1.12×10^{11}	44	5.85
Knight *et al.*[e]	1.25×10^{11}	-	-
Briere and Gaspard[f]	7.83×10^{10}	63.5	~ 0
D_2O			
Ertl and Gerischer[a]	8.9×10^{10}	150	8.1
This work[d]	7.5×10^{10}	178	6

Recombination distances are recalculated from the relaxation times given by other workers using the ionic conductivity given in the analysis section and the dielectric constants given in the Discussion.

[a] Recalculated data of V.G. Ertl and H. Gerischer, Z. Elektrochem. 66, 560 (1962)

[b] Recalculated data of M. Eigen and L. De Maeyer, Z. Elektrochem. 59, 986 (1955)

[c] Recalculated data of G.C. Barker, P. Fowles, D.C. Sammon, and B. Stringer, Trans. Faraday Soc. 66, 1498 (1970)

[d] D_2O result is estimated from extrapolation of mole fraction dependence to pure D_2O. H_2O result is not from an Arrhenius fit, it is an average of points near 25°C.

[e] B. Knight, D.M. Goodall, and R.C. Greenhow, J. Chem Soc. Faraday 2, 75, 841 (1979)

[f] Recalculated data of G. Briere and F. Gaspard, J. Chim. Phys. 64, 1071 (1967)

shows a comparison with previous results from both H_2O and D_2O at 25°C. Our results for H_2O show closer agreement with Barker _et_ _al_.[9] than with the other results[10-12].

Figure IV-13 shows the recombination rate as a function of hydrogen mole fraction. There is a monotonic increase from pure D_2O to H_2O.

Figure IV-13

Thermal recombination rate as a function of hydrogen mole fraction. Error bars show the range of at least four values in a weighted least squares average.

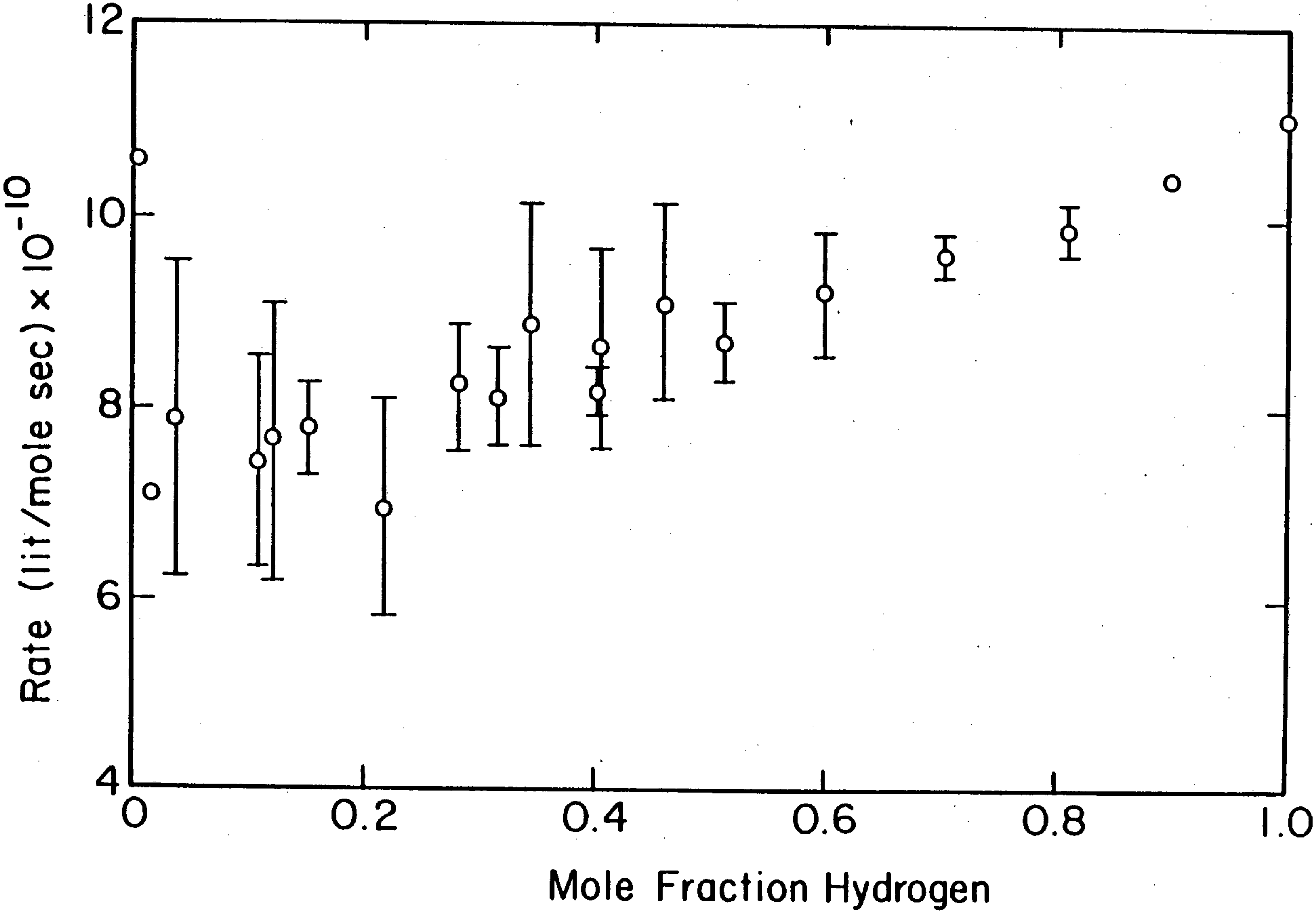
Rate (lit/mole sec) × 10^{-10}
12
10
8
6
4
0
0.2
0.4
0.6
0.8
1.0
Mole Fraction Hydrogen

XBL 831-7733

1. B. Knight, D.M. Goodall, and R. Greenhow, J. Chem. Soc. Faraday Trans. 2, 75, 841 (1979)
2. C.K.N. Patel and A.C. Tam, Nature (London) 280, 302 (1979)
3. W.A.P. Luck, "Structure of Water and Aqueous Solutions", Verlag Chemie (1974) p 251.
4. G.M. Hale and M.R. Querry, Appl. Opt. 12, 3 (1973)
5. W.A.P. Luck and W. Ditter, J. Mol. Struct. 1, 261 (1967/68)
6. W.A.P. Luck and W. Ditter, Z. Naturforsch. B24, 482 (1969)
7. D. Eisenberg and W. Kauzmann, "The Structure and Properties of Water" (Oxford University Press, New York (1969), p 188
8. A.C. Tam and C.K.N. Patel, Applied Optics 18, 3348 (1979)
9. G.C. Barker, P. Fowles, D.C. Sammon, and B. Stringer, Trans. Faraday Soc. 66, 1498 (1970)
10. G. Ertl and H. Gerischer, Z. Elektrochem. 66, 560 (1962)
11. M. Eigen and L. De Maeyer, Z. Elektrochem. 59, 986 (1955)
12. G. Briere and F. Gaspard, J. Chim. Phys. 64, 1071 (1967)

CHAPTER V. DISCUSSION

This section is broken into two parts. First, the thermal recombination rate, then the laser-induced reaction will be examined.

I. Thermal Recombination Reaction

The recombination reaction was first modeled by Eigen[1,2] as a diffusion-controlled approach of hydronium and hydroxide ions followed by a rapid neutralization by proton transfer. Ionic diffusion coefficients are combined with recombination rates to yield a recombination distance.

Following Holzwarth *et al.*[3]

$$k_{-1} = 4\pi N D_{AB}\, \sigma\, \delta/(e^{\delta} - 1) \qquad (1)$$

where k_{-1} is the recombination rate, N is Avogadro's number, D_{AB} is the sum of the diffusion coefficients for reacting ions A and B, σ is the reaction distance and δ is given by

$$\delta = Z_A\, Z_B\, e^2/\sigma\varepsilon kT. \qquad (2)$$

Z_Ae and Z_Be are ionic charges, ε is the H_2O dielectric constant, T is the temperature and k is Boltzmann's constant. Physically, δ is the ratio of the Coulomb energy at the recombination distance to the thermal energy. Ionic diffusion coefficients are given by the Nernst-Einstein relation

$$D_i = RTZ_i\, \lambda_i/F^2 \qquad (3)$$

where F is the Faraday constant and λ_i is the single ion equivalent conductivity. The dielectric constant for

H_2O and D_2O is given by Vidulich et al.[4]. A linear interpolation was used for intermediate mole fractions. Expressions used for ionic conductivities and recombination rates were given in the analysis section.

The reaction distance calculated from equations (1-3) for H_2O at 25°C is 5.85 ± 0.5 Å. A comparison with previous results is given in Table IV-1. The dependence of reaction distance on temperature and mole fraction of hydrogen is given in Figure V-1. Both Ertl and Gerischer[5] and Barker et al.[6] report results at temperatures other than 25°C. The results reported by Ertl and Gerischer show considerable scatter, varying from 5.9 Å to 8.5 Å for five temperatures between 5°C and 32°C with perhaps a slight increase in distance with increasing temperature. Barker et al.[6] report a 0.6 Å decrease in distance with a temperature increase from 25°C to 50°C. However, it is not clear what values were used for ionic diffusion coefficients and dielectric constants. The constant reaction distance of 5.8 ± 0.5 Å with temperature and isotopic composition observed here is physically more pleasing than the variation suggested previously[5,6]. The extensive hydrogen bonding in liquid water produces local structure with tetrahedral arrays of H_2O oxygens having O ··· O atom distances in neutral water of about 2.8 Å[7,8]. This distance is nearly independent of temperature and isotopic composition of the liquid. Structure need not be broken for transport of hydronium and hydroxide ions through the solution. Approximately 80% of the proton conductivity is caused by an ionic hopping mechanism where the proton jumps from an H_3O^+ to the O atom of a neighboring H_2O molecule[9]. A similar mechanism can account for high hydroxide mobility. The potential energy a proton hopping towards a hydroxide ion feels can be thought of as a superposition of a symmetric barrier midway between equilibrium positions of the oxygen atoms with an attractive Coulomb potential. The potential is shown schematically in one dimension in Figure V-2. Thus, the possible ionic recombination distances should be "quantized", with the allowed distances determined by the location of successive O atom wells. Neutron diffraction studies show that the distance is considerably compressed in the hydronium and hydroxide ion relative to neutral water[10] with an O ••• O distance of about 2.52 Å[11] for hydronium in either H_2O or D_2O. Bond distances in crystals containing hydronium ion hydrates[12-15] and theoretical studies of hydrated hydronium ions[16] also show a similar O ••• O atom distance. Theoretical studies of hydroxide ions[16] with a successively increasing number of water molecules of hydration show an O ••• O distance between 2.45 Å and 2.61 Å. This distance is somewhat larger than for the corresponding hydronium ion but still greatly compresssed relative to the neutral water distance. Crystal structures containing hydroxide ion hydrates[17,18] also

Figure V-1

Recombination distance as a function of temperatue (X) in H_2O and mole fraction hydrogen (O) at 25°C. The recombination distance is constant within experimental error with temperature and mole fraction hydrogen. The solid line is a recombination distance of 5.8 Å.

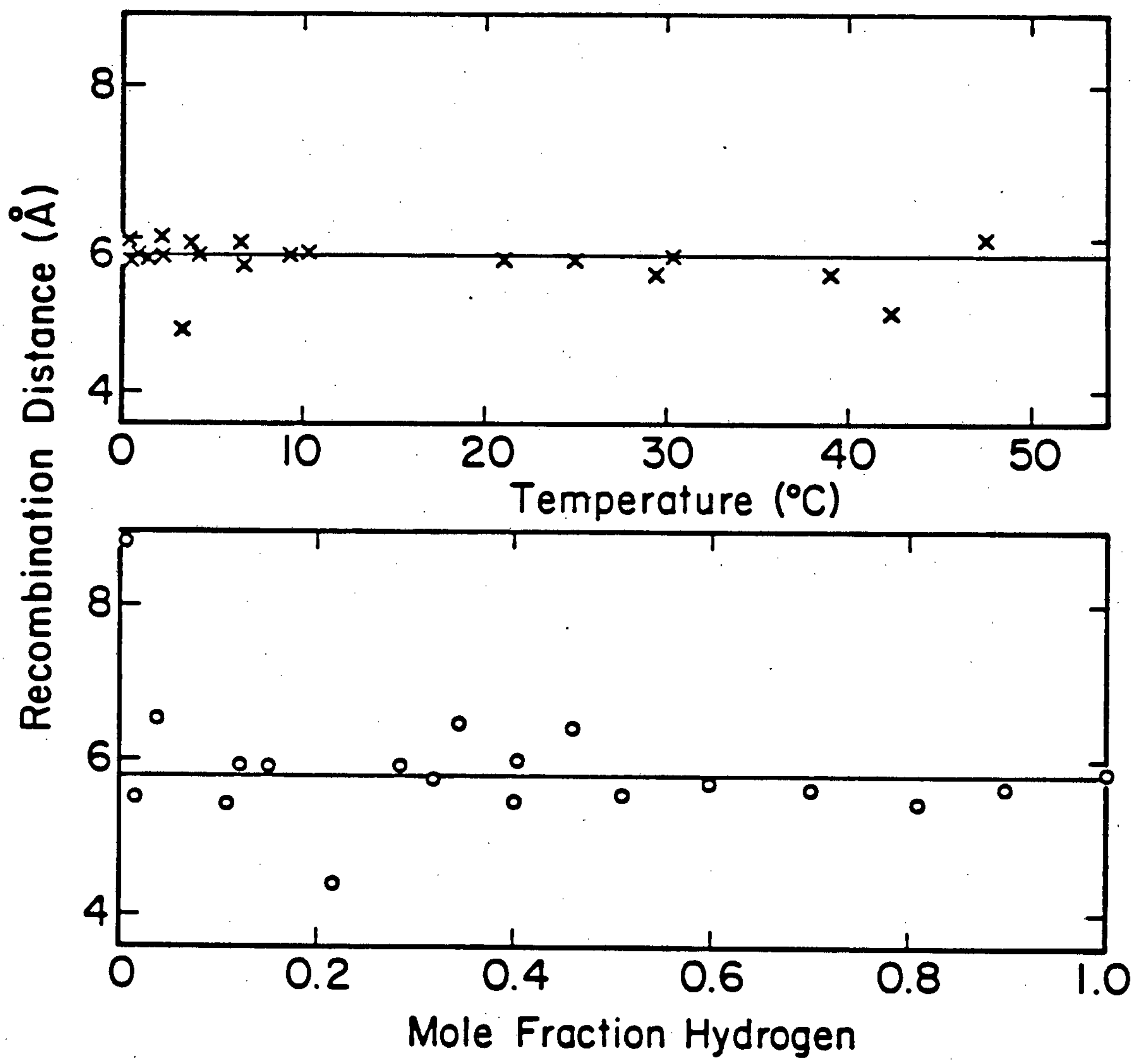

Recombination Distance (Å)
8
6
4
0
10
20
30
40
50
Temperature (°C)
8
6
4
0
0.2
0.4
0.6
0.8
1.0
Mole Fraction Hydrogen

XBL 831-7709

Figure V-2.

One-dimensional schematic diagram of the potential of a proton in a linear chain of hydrogen bonded oxygen atoms (A); the Coulomb attraction of a proton to a hydroxide ion (B); and (C), the superposition of potentials (A) and (B).

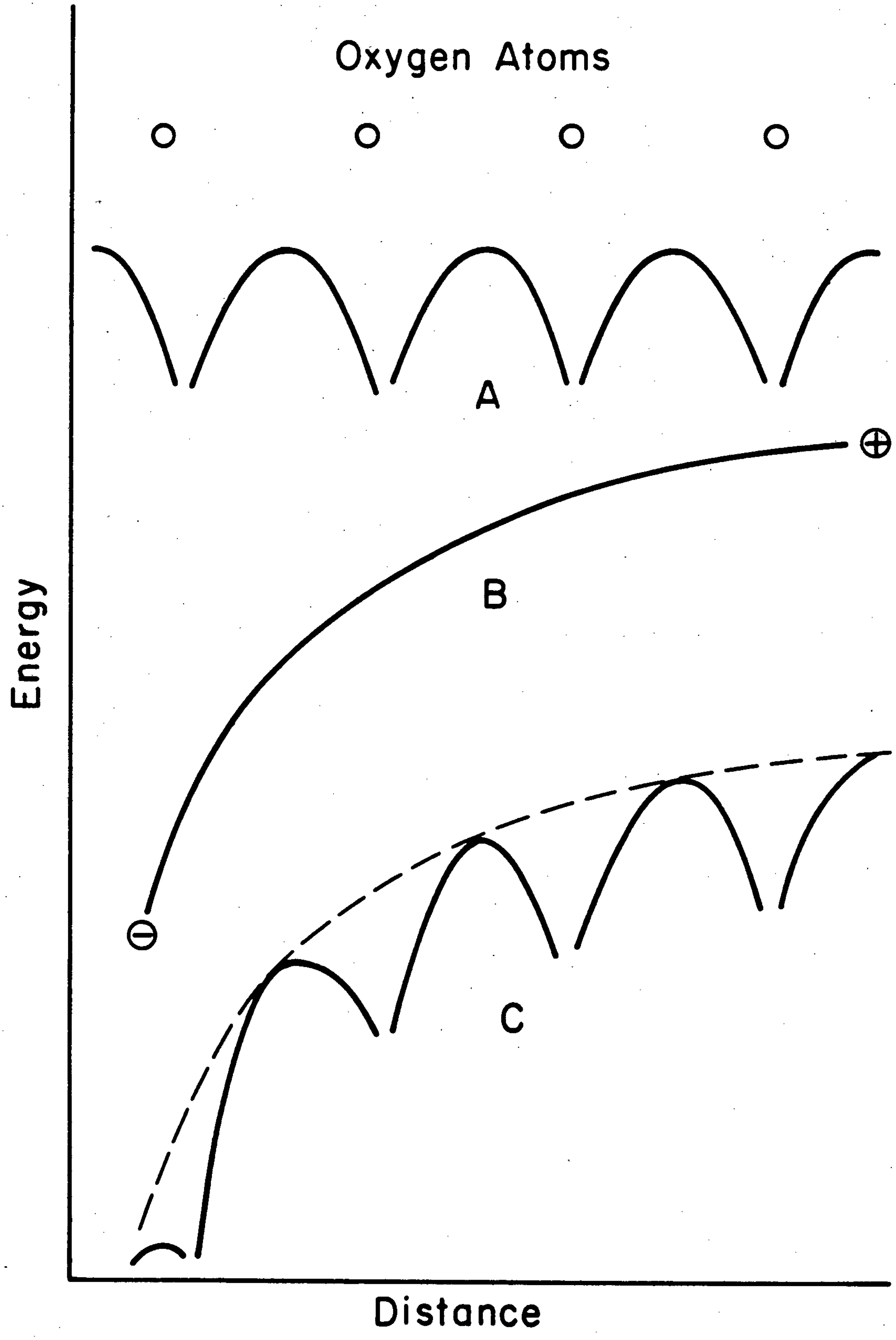
Oxygen Atoms
A
⊕
B
Energy
⊖
C
Distance

XBL 831-7705

show a slightly longer O ••• O distance than for the corresponding hydronium ions.

Eigen[1,2] first proposed a linearly bound, four oxygen, ion pair chain intermediate for the ionic recombination. This intermediate will have a configuration-dependent "allowed" distance for the ionic ends of between 6.3 Å and 4.2 Å. This assumes a 2.52 Å nearest neighbor oxygen atom separation similar to ions rather than the 2.8 Å for neutral water. The ion pair H-O ••• H bond angle is 109°. The measured recombination distance is between these two extremes. The distance is not expected to vary strongly with temperature or isotopic composition because the O-O atom separation does not change markedly. Figure V-3 shows the geometry for the two extreme configurations.

In conclusion, the observed recombination distance and lack of temperature and isotopic dependence is consistent with the linear four-molecule chain intermediate.

II. Laser Reaction

One goal of the Discussion is to give a physically meaningful interpretation of the results. The discussion of the laser-induced reaction consists of two parts. The first part is a physical interpretation that is independent of the model used to describe the quantum yield kinetics. The second part is a formulation and application of a quantum yield model. Many of the quantum yield results cannot be given a physically meaningful interpretation without development of a model.

Figure V-3

The minimum and maximum distance geometry for a linear chain of four hydrogen-bonded water molecules.

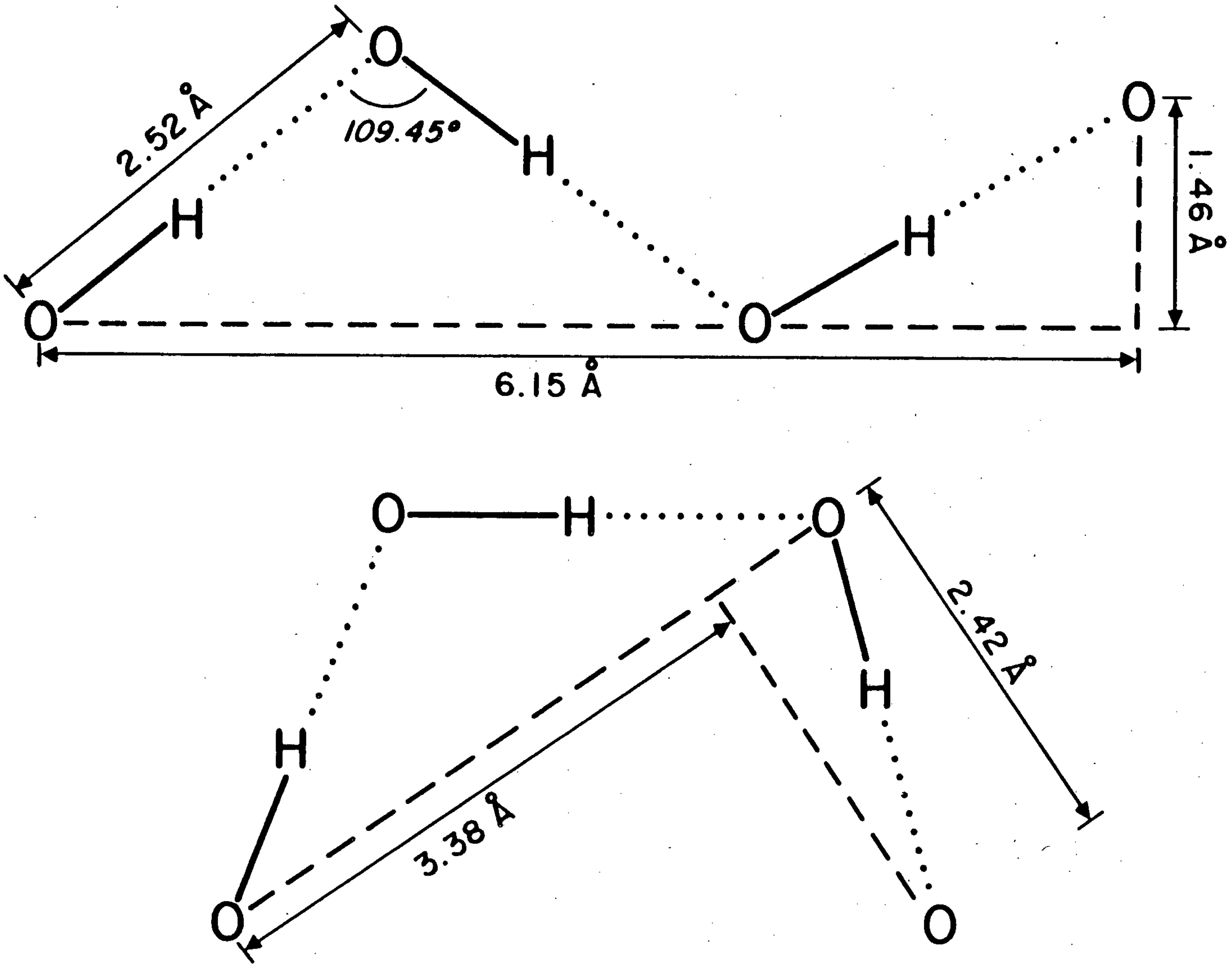
2.52 Å
O
109.45°
H
H
O
1.46 Å
O
H
O
6.15 Å
O
H
O
2.42 Å
H
H
3.38 Å
O
O

XBL 831-7727

A. Model Independent Interpretation

1. Nature of the laser-induced reaction.

The experimental results demonstrate that the laser reaction is induced by vibrational overtone absorption of a single photon in liquid water to produce H_3O^+ and OH^- ions. The evidence is as follows: The linearity and unit slope of the conductivity peak vs. pulse energy plots of Figures IV-1 and IV-2 denote a single photon process. Agreement of the measured relaxation rate with previous measurements of the H_3O^+ and OH^- equilibrium relaxation rate (Table IV-1) is consistent with H_3O^+ and OH^- final products. Signal from an impurity absorption would not correlate with the H_2O overtone absorption spectrum, contrary to data shown in Figures IV-3, IV-4, and IV-5. Additional evidence that an impurity does not produce the conductivity signal is provided by the absolute magnitude and the relative magnitude of the conductivity peak in H_2O and D_2O. An impurity would absorb photons by making either an overtone transition or an electronic transition. Estimates of the magnitude of the peak conductivity in each case follow.

The first possibility is overtone absorption into an A-H stretch of an impurity molecule, A-H. If the absorption strength of the A-H bond were the same as the O-H stretch of an H_2O and the reaction quantum yield were 1, then the impurity level would have to be about 40 ppm to produce the observed quantum yield of 4×10^{-5} at 18,140 cm^{-1}. A more realistic, lower estimate of the quantum yield would require a > 40 ppm impurity concentration. No impurities were observed in a GCMS at a sensitivity of 5 ppm. Therefore, a vibrational transition by an impurity could not produce the conductivity signal.

The second possibility is electronic absorption of an impurity to produce an excited electronic state with lower pK than the ground state. The absorption strength would be considerably larger for an electronic absorption than for an overtone absorption. An impurity could be present at a level < 5 ppm and still produce the observed signal. However, the relative conductivity peak magnitude observed upon changing the solvent from H_2O to D_2O eliminates the possibility that electronic absorption by an impurity caused the transient conductivity. Solvent change does not affect the electronic absorption strength of the impurity, but could cause a signal decrease due to both ionic mobility and reaction rate or equilibrium isotope effects. The maximum peak conductivity can be estimated. Kinetic and equilibrium isotope effects lie in a range from 1.5-11[19]. An isotope effect of 11 coupled with the mobility decrease upon a solvent change from D_2O to H_2O produces at most a factor of 16.5 reduction in the conductivity peak height. The measured peak height reduction is by a factor of 60-70.

2. Wavelength dependence of the quantum yield in H_2O

Interpretation of the constancy of quantum yield with wavelength within an absorption band requires knowledge of the main source of band broadening. Two broadening mechanisms for O-H or O-D stretch fundamentals and first overtones in the solid or liquid water will be discussed. The mechanisms are (1) inhomogeneous broadening caused by a random, slowly-changing distribution of O ••• O distances of neighboring H-bonded molecules; and (2) a combination overtone series caused by strong coupling of O-H stretch motions with O ••• O stretch vibrations.

Rice and Sceats[20] have developed a model for liquid water based mainly on spectroscopic measurements of the liquid and of the crystalline, or amorphous solid. The model was used by Sceats and Belsley[21] to interpret the overtone OH stretching spectrum. First, the fundamental O-H stretch was examined. A total width caused by a temperature-dependent homogeneous and a temperature-independent inhomogeneous portion is calculated for the ice I O-H stretch spectrum of HOD in D_2O. The local structure and spectral features caused by librational and translational motions in the liquid are similar to ice. Since these motions are responsible for the homogeneous spectral width in ice, the same temperature-dependent width was assumed for the liquid. A root mean square homogeneous width increasing from 28 cm^{-1} to 42 cm^{-1} between 10°C and 90°C was found for the liquid. The calculated homogeneous width is much smaller than the measured spectral widths; consistent with their hypothesis that the dominant contribution to the O-H stretch lineshape arises from inhomogeneous broadening. Sceats and Belsley conclude that the homogeneous component of the overtone O-H stretch should be only slightly larger than for the fundamental. The Sceats and Belsley model assumes the O-H stretch absorption band is a "pure" band, not in combination with other liquid motions.

The second broadening mechanism involving a combination of O-H stretch with the O-H ··· O stretch of hydrogen-bonded oxygens has recent experimental support[22-27]. This mechanism has been used successfully for interpretation of spectra of other hydrogen-bonded systems. References 24 through 27 describe experimental and theoretical work on the gas phase $Me_2O \cdots HCl$ and $Me_2O \cdots HF$ systems. The spectra are adequately described in a model using a Born-Oppenheimer type separation of the rapid X-H stretch motion from the slower X-H ··· Y hydrogen bond motion. The XH ··· Y bond wavefunctions are determined by an effective potential, that is dependent upon the quantum state of the X-H oscillator. When a spectroscopic transition is induced in the X-H oscillator, the quantum state of the XH ··· Y oscillator will change simultaneously if a shift in the effective potential minimum causes a favorable "Franck-Condon" factor.

A similar model can be invoked to explain the infrared spectrum of hydrogen-bonded clusters of gas phase water molecules[22]. There are several peaks in the fundamental O-H stretching region separated by 150-200 cm^{-1}, the approximate OH ••• O stretching frequency. The same pattern is observed in the depolarization CARS spectrum of liquid water[23]. This technique enables resolution of the underlying spectral features which compose the fundamental O-H stretch absorption, in contrast to normal infrared or Raman spectroscopy where the fundamental has a single broad unresolved peak.

There is a generally accepted precedent in a different condensed phase system for using combination bands of an intramolecular vibration with lattice motions to explain infrared spectral lineshapes[28]. The infrared lineshapes of impurity molecules embedded in rare gas matrices typically show a sharp "fundamental" zero phonon line accompanied by a broad, blue shifted, phonon sideband. The sideband is composed of a combination of the "fundamental" motion with latice phonons. If the lattice phonons are strongly coupled to the fundamental, then the zero phonon line is weak and the phonon sideband dominates the spectrum. The broad absorption lines in water could be analogous to the phonon sideband of a matrix isolated molecule strongly-coupled to lattice motions.

Armed with two possible spectral broadening mechanisms, we can use each model to interpret the constant quantum yield within water absorption bands. If the bulk of the broadening is inhomogeneous, as suggested by the Sceats-Rice-Belsley[20,21] model, then the quantum yield, ϕ, is independent of the differences in regional structure which cause the spectral broadening. Since $\phi \approx k_{react}/k_{relax}$, either the ratio k_{react}/k_{relax} is independent of regional structure, or the system remains activated long enough to thermally sample the average regional structure. Rice and Sceats[20] mention a 10^{-11} second order of magnitude time for the thermal diffusion processes that alter regional structures.

If broadening comes from combination of OH ••• O lattice motion with the O-H stretch, then excitation of the low frequency lattice mode does not produce reaction products as efficiently as an equivalent energy of OH stretch. Either, the low frequency OH ••• O stretch is not strongly coupled to the reaction coordinate (k_{react} is nearly constant with increasing excitation of the OH ••• O) stretch; or energy in the OH ••• O stretch is rapidly delocalized and thermalized by strong coupling to surrounding H_2O molecules (k_{relax} is greater for excitation of the OH ••• O stretch).

It is reasonable to expect OH ••• O stretch lattice vibrations to be delocalized rapidly relative to O-H stretch vibrations. The lattice vibrations come from an oxygen atom moving with respect to its neighbors, whereas the OH stretch is predominantly an intramolecular motion.

3. Quantum yield temperature dependence.

A temperature increase raises the quantum yield by increasing the rate of ion pair formation and/or the rate of ionic separation from the ion pair.

Results at several photon energies show that a temperature increase is less effective in promoting the laser reaction as the photon energy goes up. The thermal fraction of the total energy is smaller as the photon energy increases.

4. Hydrogen mole fraction dependence of the quantum yield and the wavelength dependence in nearly pure D_2O.

A hypothesis that the quantum yield for HOD is small compared to the quantum yield for D_2O in a predominantly D_2O solution is consistent with the experimental results shown in Figures IV-8 and IV-5. First, the quantum yield dependence with mole fraction of hydrogen of Figure IV-8 is considered.

As the mole fraction of added hydrogen increases, the composition and the concentration of each excited species changes. The absorption strength of an O-H stretch is more than an order of magnitude greater than an OD stretch for wavelengths between 9400 cm^{-1} and 15,380 cm^{-1}. Upon addition of H_2O to D_2O, the major excited species in the solution rapidly switches from D_2O to HOD, the predominant hydrogenated species present at small hydrogen mole fraction. There is an equal absorption into OH and OD stretches at 0.06, at 0.04, and between 0.01 and 0.06 mole fraction hydrogen for excitation at 9400 cm^{-1}, 11800 cm^{-1}, and 15380 cm^{-1}, respectively. Figure V-4 shows the relative absorbance of H_2O, D_2O, and HOD as a function of hydrogen mole fraction for excitation at 9400 cm^{-1}. The dips in the quantum yield vs. mole fraction hydrogen curves of Figure IV-8 are in regions where the absorption is shifting from D_2O to HOD. Figure IV-8 includes a fit of the quantum yield vs. mole fraction hydrogen to the form

$$\phi = \frac{\sum_i \varepsilon_i \phi_i}{\sum_i \varepsilon_i} . \qquad (4)$$

Species "i" represents H_2O, D_2O, or HOD. The base 10 absorbance of species i in the isotopic mixture is ε_i. For excitation at 9400 cm^{-1}, the fit corresponds to a linear combination of the curves in Figure V-4. The best fit at both 11800 cm^{-1} and 9400 cm^{-1} is with an

HOD quantum yield less than either H_2O or D_2O. The curve from equation (4) has the correct qualitative shape, with a better fit at 11,800 cm^{-1} than at 9400 cm^{-1}. However, the curve for greater than 0.5 mole fraction hydrogen does not have as much upward curvature as the experimental points.

Assumption of a smaller quantum yield for HOD than for D_2O can also reproduce the quantum yield dip on the blue side of the absorption band shown in Figure IV-5. The absorption maximum for HOD peaks on the blue side of the D_2O band. A 0.017 mole fraction hydrogen mixture will have 50% OD stretch absorption and 50% OH absorption at the OH stretch maximum. On the red side of the band, the OD stretch is dominant with 75% absorption and the OH stretch contributes 25%. Thus, as the excitation source is tuned from the red to the blue side of the band, increasing amounts of HOD relative to D_2O are excited. Equation (4) can predict the quantum yield behavior. If a relatively small HOD quantum yield of 1.8×10^{-8} is assumed, then a D_2O quantum yield of 1.8×10^{-7} is required to match the observed 1.38×10^{-7} quantum yield for excitation on the red side of the band at 9450 cm^{-1}. The predicted quantum yield on the blue side where the OH stretch has maximum absorbance is 9×10^{-8}. This agrees quite well with the measured 8.4×10^{-8}.

Figure V-4

The relative absorbance of H_2O (-----), D_2O (———), and HOD (-·-·-·-·) as a function of mole fraction hydrogen for excitation at 9400 cm^{-1}.

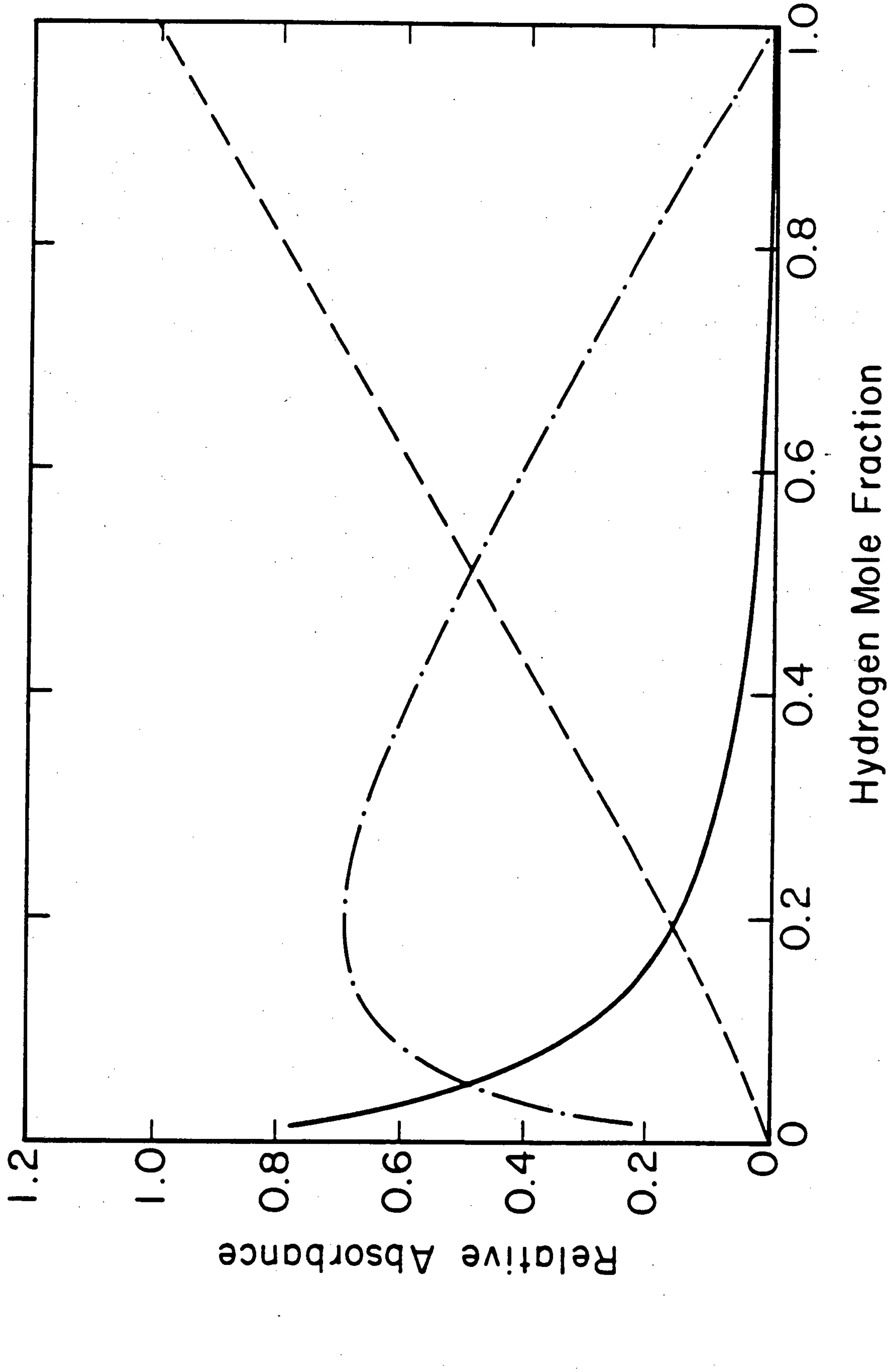
Relative Absorbance
1.2
1.0
0.8
0.6
0.4
0.2
0
Hydrogen Mole Fraction
0
0.2
0.4
0.6
0.8
1.0

XBL 831-7732

The question of why the quantum yield for HOD is less than for H_2O arises. Isotope effects in chemical reactions of isolated gas phase systems are well characterized[29]. Substitution of D for H atoms in a reacting system lowers the zero point energy of both the reactant and the transition state. The usual result is an increase in activation energy and a decrease in reaction rate. The experimental measurement of isotope effects in thermal proton transfer reaction rates and equilibria in condensed phase have gained increasing interest[30].

Typically, rates are not linear, but are monotonically increasing with hydrogen mole fraction, in contrast to the quantum yield results. There are two qualitative differences between the isotopic dependence of a quantum yield and of a reaction rate. The non-monotonic behavior of the water ionization dissociative quantum yield must have its origin in these differences. First, the overall quantum yield isotope effect depends on the individual isotope effects for several elementary processes including (a) the diffusive separation of ions from the ion pair, (b) the ion pair formation, and (c) the pathway and rate of energy relaxation. Secondly, the activated system is not in equilibrium. Its energy is much greater than the typical thermal energy and is not statistically distributed immediately following photon absorption. The O-L stretch motion of bonds containing hydrogen are preferentially excited in isotopic mixtures. Finding the source of the quantum yield mole fraction dependence requires development of a model for the individual elementary processes.

B. Quantum yield model

This section develops a model for the ion formation mechanism. The goal is to provide a qualitative interpretation of the experimental results. So far, the discussion is independent of the model chosen for the reaction and relaxation processes taking place following overtone excitation. The quantum yield described in the analysis section will be discussed here as arising from two consecutive processes. The first process is (a) formation of an ion pair in competition with deactivation of the excited molecule or group of molecules involved in the transition state. This is followed by the second process, (b) diffusive separation of the ion pair to form free ions in competition with recombination.

The modeling approach is to divide the ionization processes into two parts with one part dependent on only bulk properties of the solvent and another part dependent on only the local properties of an activated reactant.

The function of the division is to remove the contribution from bulk diffusion which has been established and well characterized by thermal recombination work from the local rate process that could not be observed in the previous work. Thus, new information about the local rate processes will be obtained. Thermal recombination studies provide no kinetic information for the local ion pair recombination because diffusion to form the ion pair is rate determining. Large changes in ion pair recombination rates will not affect the observed thermal relaxation rate. In contrast, the quantum yield of the laser-induced reaction is dependent on both the efficiency of ion pair separation and the local relaxation, ion pair formation and recombination rates.

Thus, the quantum yield is described by

$$\phi = P_{IP} P_{IS}. \tag{5}$$

The probability of ion pair formation, P_{IP}, is given by the competition of ion pair formation with relaxation, $P_{IP} = k_{1a}/(k_{1a} + k_2)$. (See the analysis section for a definition of the rates.) P_{IP} is dependent only upon local reaction and relaxation rates of the activated reactant. The probability of ion pair separation, P_{IS}, is composed of a bulk and a local contribution.

1. Probability of ion pair separation.

The overall energetics for ion pair formation and separation is shown in Figure V-5. In order to contribute to the conductivity signal, an ion pair resulting from the laser-induced reaction must diffuse apart; out of the attractive Coulomb well.

The standard treatment for diffusive encounters in the recombination of reactive species was first described by Smoluchowski[31,32] and solved for a Coulomb potential by Onsager[33]. The solution, assuming an infinite recombination velocity at the recombination distance was applied to the thermal recombination as described in the first discussion section. The assumption is a reasonable approximation for the diffusion controlled thermal recombination, but not for the ionic separation following the laser-induced reaction. An infinite recombination velocity gives a quantum yield of zero. More recently, a solution with finite recombination velocity was provided by Hong and Noolandi[34]. They give an expression for the ionic survival probability of an isolated ion pair as a function of (i) time following the initial ion formation, (ii) recombination distance, and (iii) formation distance. The conductivity a microsecond or two following excitation is related to the survival probability at long time for an ion pair formed at the recombination distance. The geminate recombination, or recombination of the ion pair, is fast on the timescale of the Hong and Noolandi survival probability and only the ions that permanently escape geminate recombination contribute to the conductivity peak. Then, the quantity of interest for modeling the quantum yield is the survival probability at infinite time given initial formation at a radius equal to the recombination distance.

Figure V-5

Energetics of ion pair formation and ion pair separation to form free ions. The photon energy is greater than the net endothermicity. The species present in the solution at each energy is shown at the right. A linear four-molecule hydrogen-bonded chain, the ion pair, and free ions are shown. Approximate energies are for H_2O near 5°C. The 5.8 Å distance denotes the distance between oxygen centers in the ion pair.

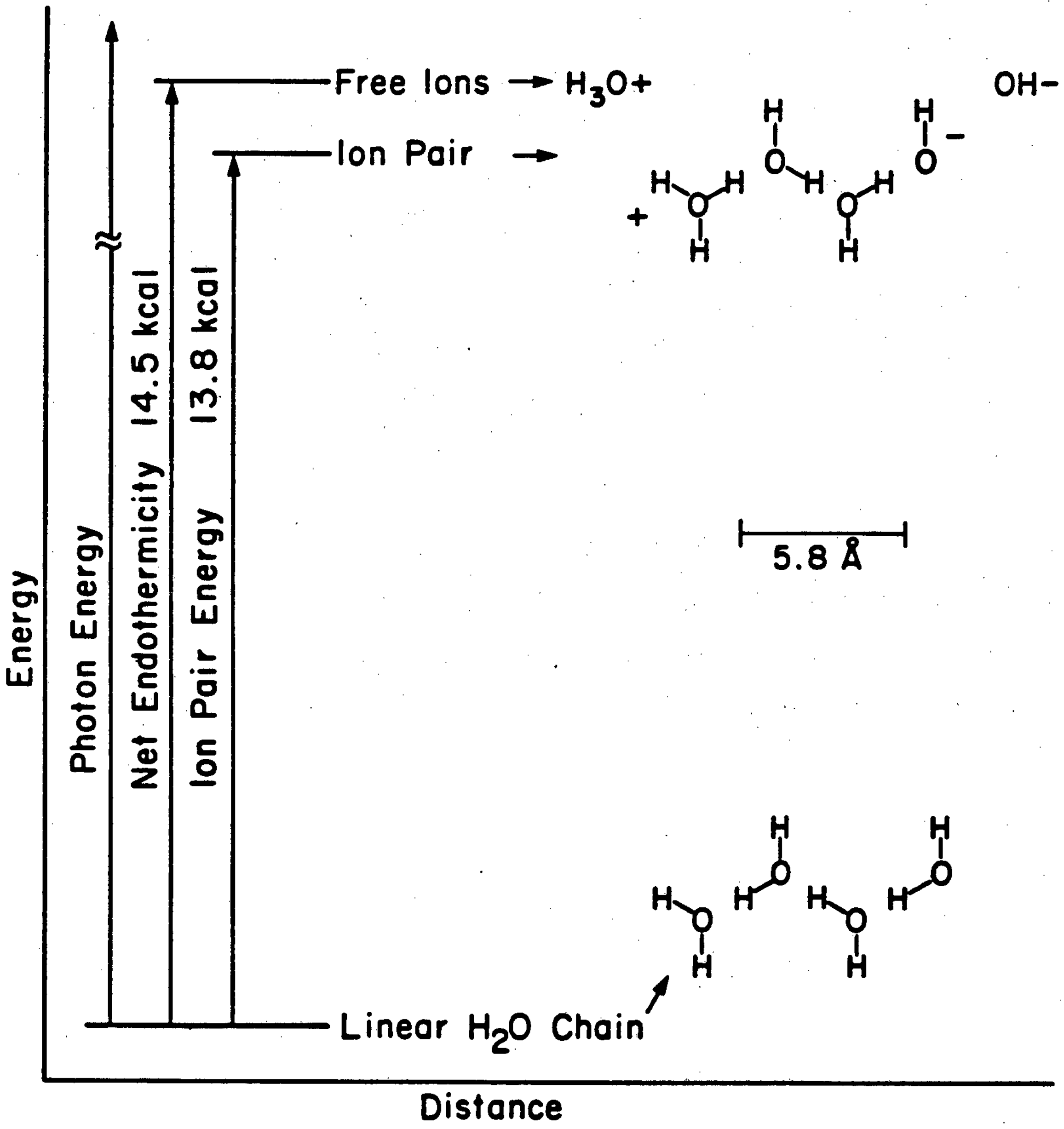
Energy
Photon Energy
Net Endothermicity 14.5 kcal
Ion Pair Energy 13.8 kcal
Free Ions → H3O+ OH-
Ion Pair →
5.8 Å
Linear H2O Chain
Distance

XBL 831-7707

From Hong and Noolandi, the survival probability at time t given initial ion pair formation at radius r_o is

$$P_{IS}(t) = \frac{U(r_o)}{U(\infty)}\left[1 + \frac{r_c}{U(\infty)(\pi D t)^{1/2}}\right] \qquad (6)$$

where $r_c = e^2/\varepsilon kT$ and D is the ionic diffusion coefficient. U(r) is given by

$$U(r) = e^{-(r_c/r)} + \left(\frac{Dr_c}{\kappa a^2} - 1\right) e^{-(r_c/a)} \qquad (7)$$

Where a is the recombination radius and κ is the recombination velocity. At infinite time the survival probability becomes

$$P_{IS}(\infty) = \frac{U(r_o)}{U(\infty)} \qquad (8)$$

From microscopic reversibility, the ion pair formation distance for the thermal reaction, r_o, is identical to the recombination distance, a. Assuming the same formation distance for the laser reaction,

$$P_{IS}(\infty) = \frac{Dr_c}{\kappa a^2}\left[\frac{1}{e^{r_c/a} + [(Dr_c/\kappa a^2) - 1]}\right] \qquad (9)$$

This equation can be simplified by considering the first multiplicative term. Substituting $\kappa = k_{-1a}\ell$ and $D = 1/2\ k_{diff}\ \ell^2$,[36]

$$\frac{Dr_c}{\kappa a^2} = \frac{k_{diff}\ \ell^2 r_c}{2k_{-1a}\ \ell a^2} \qquad (10)$$

where ℓ is the average ionic jump distance during diffusion, k_{-1a} is the recombination rate constant of the ion pair [see equation (1) of the analysis section], and k_{diff} is the rate constant for diffusive jumps.

A much larger numerator than denominator is obtained from the following: from thermal recombination studies, the distance r_c is a factor of 1.2 larger than a = 5.80 Å and the 2.8 Å of ℓ is about two times smaller than a. Therefore, $\frac{r_c\ \ell^2}{a^2\ \ell} < 1$. From thermal recombination studies, the recombination rate, k_{-1a} >> the diffusion rate, k_{diff}. Or,

$$1 \gg \frac{k_{diff}\ \ell^2 r_c}{2k_{-1a}\ \ell a^2} = \frac{Dr_c}{\kappa a^2} \qquad (11)$$

Equation 9 becomes

$$P_{IS}(\infty) = \frac{Dr_c}{k_{-1a}\ell a^2}\ \frac{1}{e^{r_c/a} - 1} \qquad (12)$$

The absolute magnitude of this equation cannot be determined because k_{-1a} is unknown. However, the temperature and isotopic composition dependence can be estimated. The thermal recombination rate studies already described show the recombination distance is approximately constant with temperature and isotopic composition, varying by less than 10% in H_2O for a temperature change from 0°C to 45°C and by less than 15% at 25°C for an isotopic change from H_2O to D_2O. The temperature dependence of $r_c = e^2/\varepsilon kT$ is a weak T^{-1} dependence, varying by about 15% from 0°C to 45°C. Use of a constant $e^{r_c/a}$ and a^2 and replacing D/kT with μ yields[35]

$$P_{IS}(\infty) \propto \mu/k_{-1a}$$

where μ is the ionic mobility. Thus, the probability of separation from the ion pair, P_{IS}, is composed of μ, which is dependent upon bulk properties of the solvent and $1/k_{-1a}$, which is a local property of the solution.

Now the full quantum yield expression can be grouped into a local and a bulk term. [See equations (1) and (2) of the analysis section for a definition of the rates.] Physically, $1/(k_{1a} + k_2)$ is the length of time a reactant remains activated, k_{1a} is the rate of laser induced ion pair formation, $1/k_{-1a}$ is the length of time an ion pair remains before recombination, and μ, the ionic mobility, is a measure of the ion pair separation efficiency.

$$P_{IP}\, P_{IS} = \phi \propto \underbrace{\left[\frac{k_{1a}}{k_{-1a}\,(k_{1a} + k_2)} \right]}_{[\text{local}]} \quad \underbrace{\left[\mu \right]}_{[\text{bulk}]} \tag{14}$$

The remainder of this section examines each term of Equation 14 in more depth. Only the ionic mobility, μ, is known quantitatively. Not enough information is known about vibrationally activated processes in a liquid to formulate a quantitative model for the other "local" terms. The goal is to obtain a qualitative idea how each term behaves as the temperature, excitation energy, and isotopic composition are changed.

2. k_{1a}/k_{-1a}

The energetics of the forward and reverse thermal reaction are known from thermal measurements. The barrier to recombination should be $\leq$ the 3.5 kcal/mole activation energy measured by an Arrhenius plot of the diffusion-controlled thermal recombination rate. Since ΔH in H_2O at 25°C is 13.5 kcal/mole, the forward barrier is $\leq$ 17 kcal/mole. Photons with enough energy to induce observable ionization (> 25.7 kcal/mole) can produce activated reactants with 8.7 kcal/mole of energy above the forward barrier or activated products with 8.7 kcal/mole above the reverse barrier.

Since the excitation energy is high and the reverse barrier is low, a local equilibrium is assumed. The model for k_{1a}/k_{-1a} will be taken to be the density of states ratio of product to reactant, at the excitation energy. The semiclassical Marcus-Rice[37] expression is used for the density of states.

$$N(E) = \frac{(E + E_z)^{s-1}}{(s - 1)! \prod_i h\nu_i} \tag{15}$$

where E is the total non-fixed energy, s is the number of strongly-coupled modes sharing the energy, $h\nu_i$ is the energy per quantum of mode i excitation and E_z is the zero point energy. The non-fixed energy of the product is $E_{ph} + E_{zr} - E_{zp} - E_o$ (see Figure V-6). The non-fixed energy of the reactant is E_{ph}. The density of states ratio of product over reactant is then

$$\frac{k_{1a}}{k_{-1a}} = \left(\frac{E_{ph} - \Delta E_o + E_{zr}}{E_{ph} + E_{zr}}\right)^{s-1} \frac{\prod_i \nu_r}{\prod_i \nu_p} \tag{16}$$

where the subscript r or p represents the reactant or product, respectively. E_{ph} represents the photon energy, and ΔE_o is the energy difference from product to reactant potential well minima.

This expression is exact if the ion pair yield is dominated by the yield a picosecond or two following excitation and if the reactant and product ion pair are in equilibrium at the excitation energy. Equilibrium will be achieved if the forward and reverse reaction rates

Figure V-6

One-dimensional potential energy surface for the water ionization reaction. The solid line shows the surface for the thermal reaction. The dotted potential surface is described near the end of section C3 of the discussion. This potential is for the laser reaction when no strongly-coupled excited modes undergo a frequency change upon going from reactants to products. E_0 for this potential is approximately equal to ΔH, the thermal reaction endothermicity.

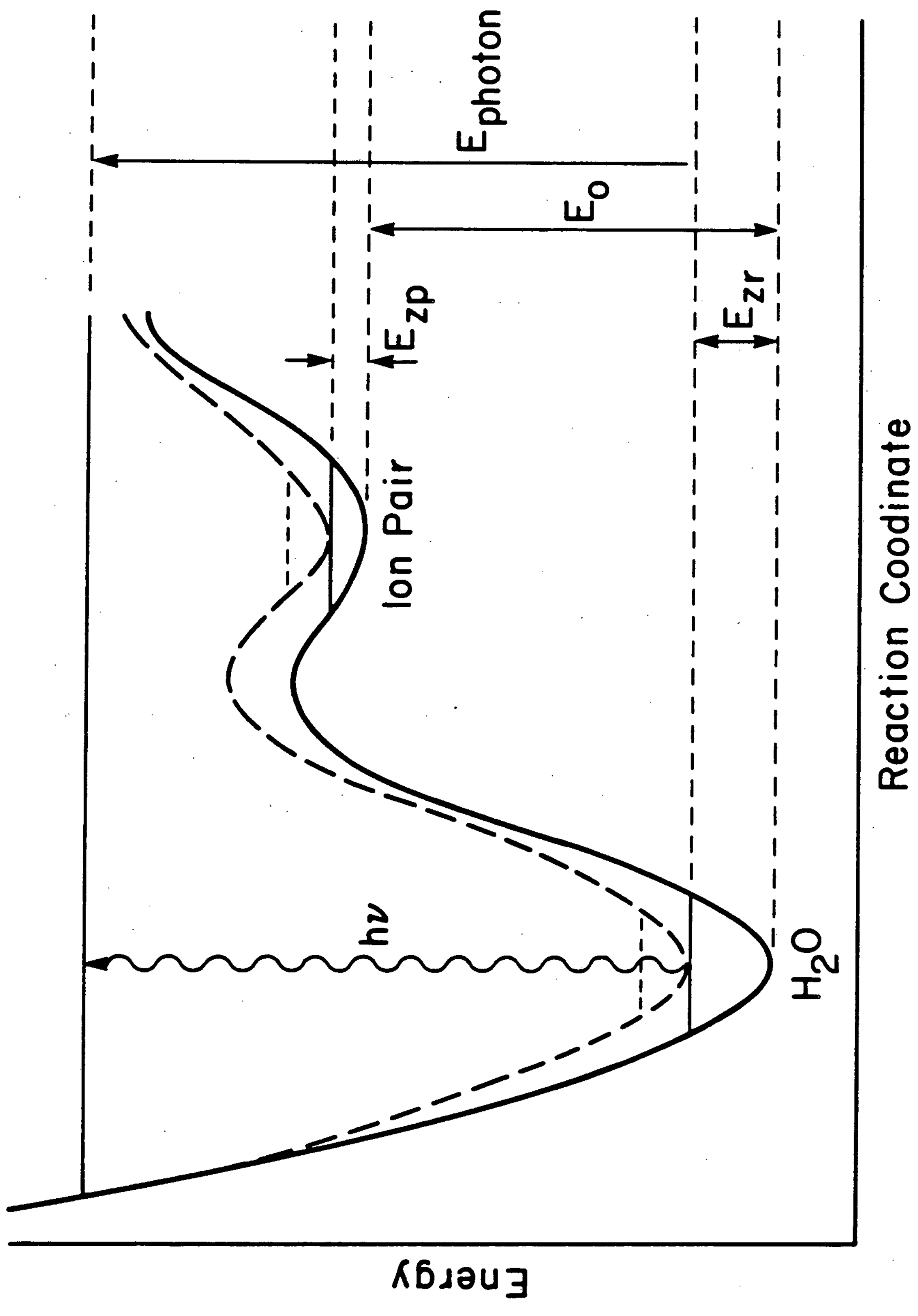
E_{photon}
E_o
E_{zp}
E_{zr}
Ion Pair
$h\nu$
H_2O
Energy
Reaction Coodinate

XBL 831-7718

are rapid compared to the relaxation rate. In the opposite extreme where relaxation is rapid compared to the reaction rates, an RRKM type expression is more appropriate for the forward rate and the reverse rate is the thermal rate. An RRKM forward rate expression is nearly proportional to Equation (16) with the non-fixed energy for the transition state being shifted by the few kcal reverse barrier, E_b, and the power, s, increasing by one in the numerator.

$$k_{1a} = \frac{(E_{ph} - E_o + E_{zr} - E_b)^s (s-1)! \prod_i h\nu_r}{(E_{ph} + E_{zr})^{s-1} s! \prod_i h\nu_{TS}} \qquad (16b)$$

This expression will have the same qualitative dependence on isotopic composition, and photon energy, as equation (16). The subscript, TS, represents the transition state,

3. $1/(k_{1a} + k_2)$

The remaining term in the quantum yield contains the relaxation rate of activated reactants, $1/(k_{1a} + k_2)$. In the limit of large vibrational relaxation rate, k_2, this term becomes $1/k_2$. No direct measurement of the vibrational relaxation rate of excited O-H stretch motions in liquid water is available. However, relaxation measurements performed on several hydrocarbons and chlorinated hydrocarbons support some general conclusions about how vibrationally excited molecules relax in a room-temperature liquid.[38-42] Both solvents interacting and solvents not interacting with the solute have been studied. H_2O excited in H_2O, or D_2O excited in D_2O are expected to be more strongly interacting than HOD in D_2O.

In non-interacting solvents, results are explained by rapid intramolecular equilibration of energy among levels energetically near and coupled to the excited level, followed by slower transfer to the solvent. For CH stretch excitation, other CH stretch modes and Fermi resonant bend overtones can couple efficiently with the excited CH stretch. In an interacting solvent, intermolecular relaxation to neighboring molecules can compete with intramolecular relaxation.

In water, Fermi resonant bends and intermolecular transfer are expected to influence the OH stretch relaxation. Figure V-7 shows an energy level diagram for liquid H_2O and liquid D_2O. Fermi resonant bend overtones are expected to contribute to relaxation of OH or OD stretch excitation in H_2O or D_2O. Nearly resonant intermolecular transfer may be important for pure H_2O or pure D_2O because broad absorption lines maintain near resonance by compensating for the anharmonicity of the overtone $v \rightarrow v - 1$ transition. Intermolecular transfer should be reduced for excitation of an OH stretch in predominantly D_2O solution where neighboring

Figure V-7

Energy level diagram for H_2O, HDO, and D_2O. Center frequencies are shown. Typical real widths are several hundred wavenumbers. Energy levels shown use fundamental frequencies. The diagram is similar for excitation of an O-H stretch overtone. Letters s, b, b + L, L, and T correspond to stretch, bend, bend plus libration combination, libration, and hindered translational or phonon modes, respectively. The average librational energy is shown for greater than three quanta of libration of H_2O and for greater than two quanta of libration for HOD and D_2O.

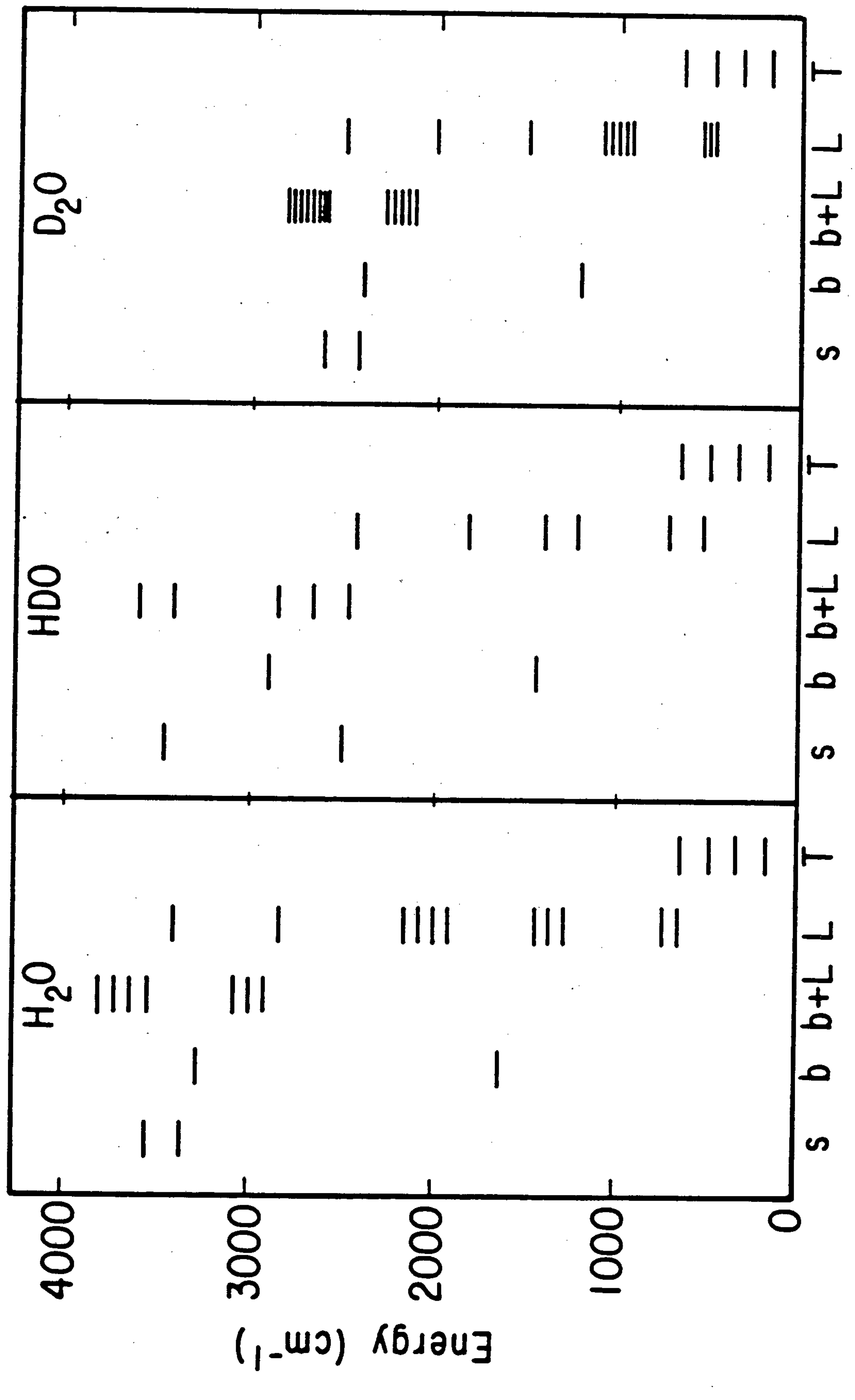

XBL 831-7734

D_2O molecules have no resonant transition. Spectroscopic studies show that at least for the fundamental, features in the O-H stretching region of ice Ih and the amorphous solid are dominated by effects of intermolecular coupling of the oscillators[43-46]. A radical change in the importance of intermolecular coupling is not expected for the liquid[43].

C. Application of the quantum yield model to results.

The following section applies the quantum yield model developed in the previous section to the hydrogen mole fraction, wavelength, and temperature dependence of the quantum yield. The approach taken in each case is as follows:

(i) The ionic mobility is known as a function of mole fraction hydrogen and temperature. The effect this term has on the quantum yield can be removed from the results.

(ii) The form of the k_{1a}/k_{-1a} term and therefore the shape of k_{1a}/k_{-1a} versus hydrogen mole fraction, temperature and excitation wavelength can be obtained from equation (16).

(iii) Some energy relaxation pathways that may be important were mentioned. However, the influence which the relaxation pathway has upon the quantum yield is not known.

1. ϕ vs. X_H

Now we return to the question of why the quantum yield for HDO excitation in predominantly D_2O solution is less than the quantum yield for D_2O. Each term which contributes to the quantum yield will be examined in turn to see if it can account for the non-monotonic dependence of the quantum yield on hydrogen mole fraction.

(i) Ionic mobility

The ionic mobility, μ, as a function of hydrogen mole fraction is known quantitatively from the ionic conductivity of H^+ and OH^- in isotopically mixed water. It increases monotonically with hydrogen mole fraction and therefore cannot account for the quantum yield dip for HOD in D_2O. The contribution of the mobility term to the quantum yield is removed and shown in Figure V-8.

(ii) k_{1a}/k_{-1a}

Consider the k_{1a}/k_{-1a} contribution to the quantum yield ratio $\phi(X_H)/\phi(D_2O)$, where X_H is the hydrogen mole fraction. From equation (16),

Figure V-8

Quantum yield divided by ionic mobility. The points represent $(k_{1a}/k_{-1a})[1/(k_{1a} + k_2)]$.

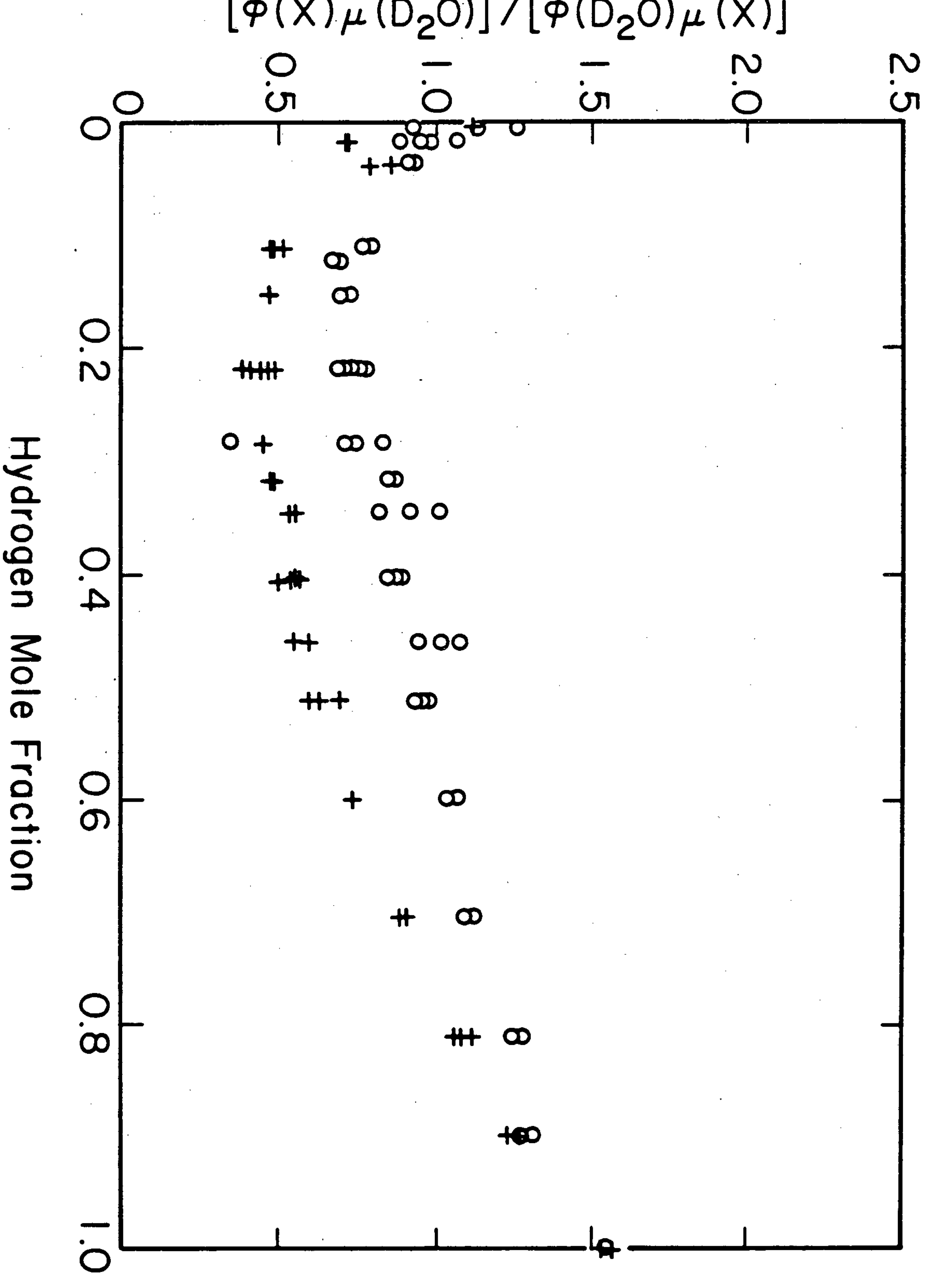
[φ(X)μ(D2O)]/[φ(D2O)μ(X)]
0
0.5
1.0
1.5
2.0
2.5
Hydrogen Mole Fraction
0
0.2
0.4
0.6
0.8
1.0

XBL 831-7723

$$\frac{\dfrac{k_{1a}}{k_{-1a}}(X_H)}{\dfrac{k_{1a}}{k_{-1a}}(D_2O)} = \frac{\sum\limits_i P_i(X_H)\,\dfrac{\prod\limits_i \nu_{ri}\left(1 + \dfrac{E_{zri}}{E_{ph} - \Delta E_o}\right)^{s-1}}{\prod\limits_i \nu_{pi}\left(1 + \dfrac{E_{zri}}{E_{ph}}\right)^{s-1}}}{\dfrac{\prod\limits_i \nu_r(D_2O)\left(1 + \dfrac{E_{zr}(D_2O)}{E_{ph} - \Delta E_o}\right)^{s-1}}{\prod\limits_i \nu_p(D_2O)\left(1 + \dfrac{E_{zr}(D_2O)}{E_{ph}}\right)^{s-1}}} \tag{17}$$

Index, i, is a label for each possible isotopically substituted reactant, and $P_i(X_H)$ is the probability of species i in a mixture with a hydrogen mole fraction of X_H. Rearranging the term involving frequencies, and using the Teller-Redlich product rule[47],

$$\frac{\Pi\nu_r(X_H) \quad \Pi\nu_p(D_2O)}{\Pi\nu_r(D_2O) \quad \Pi\nu_p(X_H)} = 1 \tag{18}$$

will eliminate all terms involving frequencies. Also, since the denominator is a constant, D, with hydrogen mole fraction, equation (17) can be simplified

$$\frac{\dfrac{k_{1a}}{k_{-1a}}(X_H)}{\dfrac{k_{1a}}{k_{-1a}}(D_2O)} = \sum_i \frac{P_i(X_H)}{D} \left\{\frac{1 + \dfrac{E_{zri}}{E_{ph} - \Delta E_o}}{1 + \dfrac{E_{zri}}{E_{phi}}}\right\}^{s-1} \tag{18b}$$

As the hydrogen mole fraction of a mixture increases, species with more hydrogens substituted for deuterium become increasingly probable and have a greater relative contribution to equation (18b). A higher zero point energy for these species implies a monotonic increase of equation (18b) with hydrogen mole fraction.

(iii) $1/(k_{1a} + k_2)$

The final term, the relaxation, must account for the non-monotonic dependence of ϕ with X_H. For the discussion, it is helpful to divide the vibrational modes of the system into reactive and unreactive modes. Then excitation of HOD in D_2O changes the energy flow relative to excitation of H_2O in H_2O or excitation of D_2O in D_2O by either (a) increasing the transfer rate to unreactive modes or (b) decreasing the transfer rate to reactive modes. Either the presence of an OD in a molecule with excited OH or presence of OD (lack of OH) bonds in the surrounding molecules causes the change of energy flow. This section demonstrates that the experimental data cannot distinguish between the two possible causes of change in energy flow. Nearly any model which has (1) a lower ϕ for HDO excitation than for H_2O or D_2O excitation or (2) a lower ϕ for OH excitation in the presence of surrounding OD bonds is in qualitative agreement with the data.

Curve A of Figure V-9 shows a fit to the experimental data for excitation at 9400 cm^{-1}. The dependence of ϕ upon ionic mobility is removed. The form for the quantum yield is the same as Equation (4). This corresponds to a lower quantum yield for HDO excitation, condition (1) above. Compared to D_2O, one potential difference in intramolecular energy flow is that transfer of energy from the excited OH to the OD bond of an HOD molecule should be slower than the nearly resonant transfer from an excited OD to the other OD of a D_2O molecule. If excitation of both OL bonds of an L_2O molecule promotes reaction, then the quantum yield for HOD compared to D_2O or H_2O will be reduced.

Curve A qualitatively fits the data, but as in the previous fit of Equation (4) to the quantum yield, there is insufficient upward curvature in the high hydrogen mole fraction region. A better fit is obtained with a model having a greater dependence of quantum yield on the fraction of neighboring bonds with the same isotopic identity as the excited bond. Figures V-9 and V-10, curves B, C, D, and E show results from such a model. The model assumes a form for the quantum yield.

$$\frac{\phi\ (X_H)}{\mu} = \sum_{ij} \frac{\phi_{ij}}{\mu}\ \varepsilon_i C_i(X_H)\ell\ P_j(X_H) \Big/ \sum_{i}\ \varepsilon_i C_i(X_H)\ell \qquad (19)$$

Figure V-9

Empirical curve (—) for three different empirical fits of ϕ/μ and experimental points (+) for 9400 cm^{-1} excitation at 25 ± 1°C. The curves are described in the text. The line (---) represents contribution from H_2O excitation, (•—•—) from HOD excitation, and (— - —) from D_2O excitation.

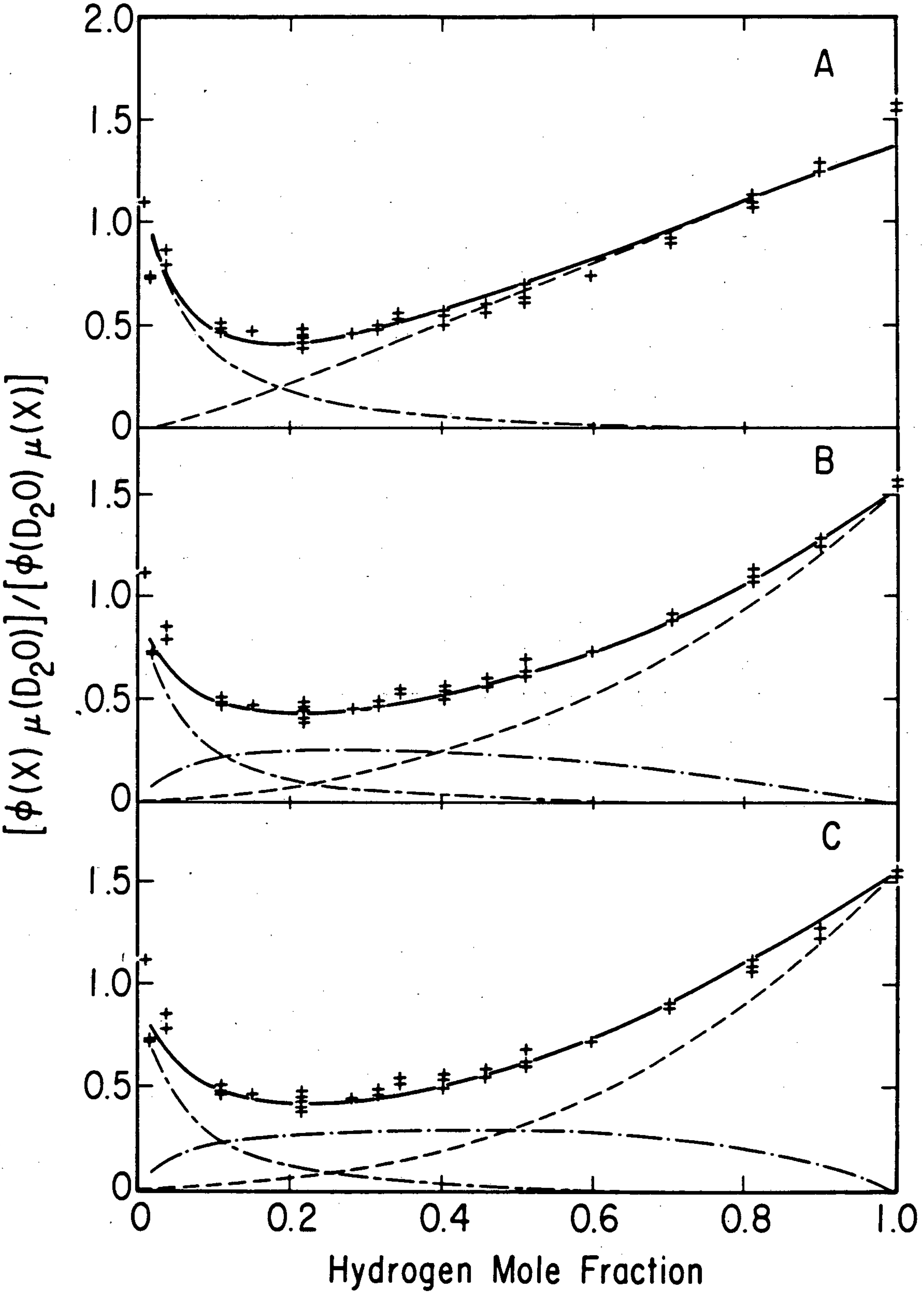
2.0
1.5
1.0
0.5
0
A
B
C
0
0.2
0.4
0.6
0.8
1.0
[φ(X) μ(D2O)]/[φ(D2O) μ(X)]
Hydrogen Mole Fraction

XBL 831-7711

Figure V-10

Empirical curve (——) for three different empirical fits of ϕ/μ, and experimental points (+) for 9400 cm^{-1} excitation at 25 ± 1°C. The curves are described in the text. The line (---) represents contribution from H_2O excitation, (•—•—) from HOD excitation and (—-—) from D_2O excitation.

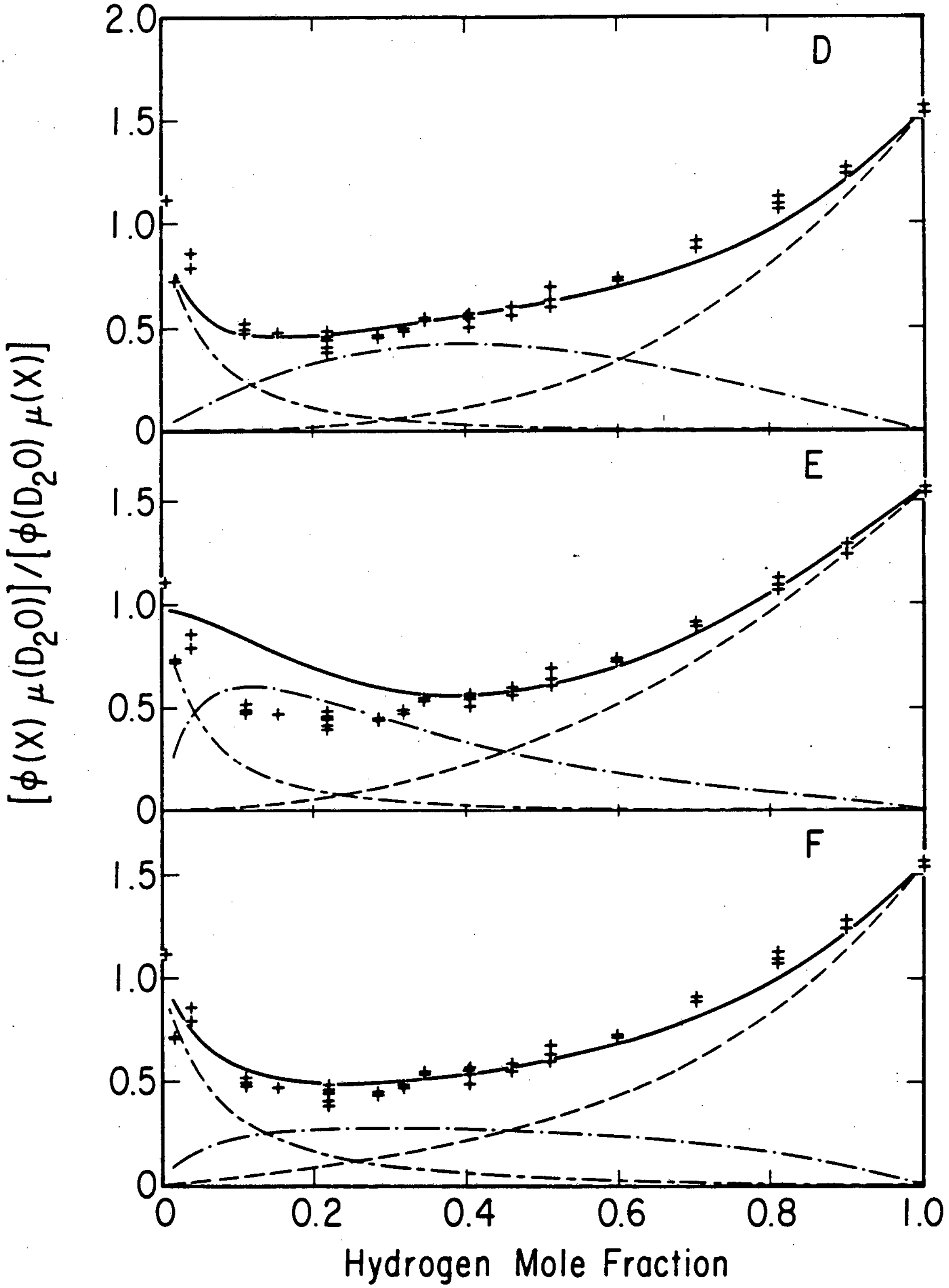
2.0
1.5
1.0
0.5
0
D
E
F
[φ(X) μ(D₂O)]/[φ(D₂O) μ(X)]
0
0.2
0.4
0.6
0.8
1.0
Hydrogen Mole Fraction

XBL 831-7712

where i represents an initially excited H_2O, D_2O, or HDO, $\varepsilon_i C_i(X_H)\ell$ is the absorbance of species i in pathlength ℓ at concentration C_i in a mixture of hydrogen mole fraction, X_H. Thus, species i absorbs a photon with a probability $\varepsilon_i C_i(X_H)\ell / \sum_i \varepsilon_i C_i(X_H)\ell$. Index j represents the isotopic configuration of two additional OL bonds, the possibilities being OH, OH; OH, OD; or OD, OD. The location of these bonds relative to the excited molecule is not specified. $P_j(X_H)$ is the probability of configuration j. Then ϕ/μ in equation (19) represents the sum of the probabilities of excitation of configuration ij times ϕ_{ij}/μ, the quantum yield/ionic mobility for excitation of species ij. The experimental points were fitted with four different sets of constraints on the coefficients ϕ_{ij}/μ. In each case, ϕ_{ij}/μ for the entirely hydrogenated species is constrained to the experimental value in pure H_2O, and ϕ_{ij}/μ for the entirely deuterated case is constrained to the experimental value in pure D_2O. The additional constraints on coefficients ϕ_{ij}/μ that were tested and the possible physical interpretations are:

(1) ϕ_{ij}/μ for i = HOD and j = any possible isotopic configuration are approximately equal to each other but not to ϕ_{ij}/μ for i = H_2O, j = OH, OH or to i = D_2O, j = OD, OD. Other coefficients are not constrained. A possible interpretation of these constraints is if the presence of both OH and OD in the excited HOD molecules

causes the quantum yield to be independent of the isotopic structure of the surrounding liquid, whereas with H_2O or D_2O excitation, the quantum yield depends on the surrounding concentration of bonds with the same isotope as that excited. Curve B of Figure V-9 shows close agreement of this model with experimental results.

(2) ϕ_{ij}/μ for i = HOD and j = OH, OH is approximately equal to ϕ_{ij}/μ for the pure solvents, i = H_2O and j = OH, OH or i = D_2O and j = OD, OD. A possible physical interpretation of this constraint is that the quanta of the excited OL bond must hop to two other OL bonds of the same isotopic species to produce a laser reaction. Then coefficients ϕ_{ij}/μ will be large for i = H_2O, j = OH, OH; i = D_2O, j = OD, OD, and, since the OH bond absorbs most of the light in an HOD molecule, ϕ_{ij}/μ will be large for i = HOD, j = OH, OH. The model does not specify the location of the two OL bonds represented by index j. They could be OL bonds of a neighboring molecule or of a linear hydrogen bonded chain. Curve C of Figure V-9 shows close agreement of this model with experimental results.

(3) ϕ_{ij}/μ for i = HOD and j = OH, OD is approximately equal to ϕ_{ij}/μ for i = H_2O and j = OH, OH or for i = D_2O and j = OD, OD. A possible physical interpretation of this constraint is that an excited molecule must have one particular adjoining molecule of the same isotopic identity to produce a laser reaction. For this model, j denotes the isotopic identity of the molecule. Curve D

of Figure V-9 shows a less acceptable fit than models (1) and (2).

(4) ϕ_{ij}/μ for i = HOD and j = OD, OD is approximately equal to ϕ_{ij}/μ for i = D_2O and j = OD, OD. If the exothermic intramolecular relaxation from the excited OH stretch to the OD stretch of an HOD molecule dominates the initial relaxation, then the system might behave similarly to when D_2O is the initially excited molecule. Curve E of Figure V-10 shows a less acceptable fit than models (1) and (2).

Final coefficients for each model are shown in Table V-1.

A model in which nearby OD quenches activated OH was also tested to see if it could fit the non-monotonic dependence of ϕ on X_H. Curve F of Figure V-10 shows a fit of

$$\frac{\phi}{\mu} = \frac{\varepsilon_{OD}C_{OD}(X_H)^{\ell}\ \phi_{D_2O} + \sum_K P_K \dfrac{1}{A(1 + n_K B)}\ \varepsilon_{OH}C_{OH}(X_H)^{\ell}\ \phi_{H_2O}}{\varepsilon_{OD}C_{OD}(X_H)^{\ell} + \varepsilon_{OH}C_{OH}(X_H)^{\ell}} \qquad (20)$$

to the experimental data. The model corresponds to a relaxation rate, k_2, for excited OH equal to $A + Bn_KA$. This is the pure H_2O rate, A, plus a term proportional to the number of nearest neighbor OD bonds, n_K, in the excited molecule and in the six OL bonds in the nearest neighbor sphere of the excited molecule. The quantum

Table V-1

Coefficients, $\phi_{ij}/(\lambda_{H^+} + \lambda_{OH^-})^a$, for empirical ϕ/μ vs. X_H curves.

coefficient (x 10^{10}) mol ohm cm^{-2}

curve	H_2O(i)			HDO(i)			D_2O(i)		
	OH, OH(j)	OH, OD(j)	OD, OD(j)	OH, OH(j)	OH,OD(j)	OD, OD(j)	OH, OH(j)	OH, OD(j)	OD, OD(j)
B	8.28	3.2	1.95	3.36	2.48	1.56	0.82	2.18	5.06
C	8.28	2.06	1.14	7.07	1.66	1.82	1.11	2.21	5.06
D	8.28	0.3	0.42	4.0	5.97	0.748	1.8	2.05	5.06
E	8.28	3.5	0.274	3.0	0.667	6.0	0.667	0.2	5.06

---

[a] $\phi_{ij}/(\lambda_{H^+} + \lambda_{OH^-})$ is proportional to ϕ/μ. $\lambda = F(\mu)$ where F is Faraday's constant. Index i denotes the initially excited species. Index j represents the isotopic identity of two additional OL bonds.

yield for D_2O excitation is independent of the isotopic composition of the nearest neighbor OL bonds. B is a proportionality constant. P_K is the probability of configuration K. A satisfactory fit of the experimental data is obtained with B = 0.55. Thus, when two of the seven O-L bonds nearest to an excited O-H are O-D bonds, the relaxation is 2.1 times as fast as for pure H_2O.

The success of model (1) in fitting the experimental data suggests a model involving resonant transfers of OH stretch excitation may be involved in the laser reaction. A physically reasonable model requiring resonant transfer of OH stretch quanta in a linear hydrogen-bonded chain of four water molecules can be devised. The ion pair intermediate of the model to be described is identical to that postulated for the thermal reaction. Motion of the three hydrogen-bonded hydrogens of a four-molecule linear chain intermediate is required to form an ion pair. The three molecules could be activated by a minimum of two hops of OL stretch quanta from the excited molecule to neighboring molecules. Assume atom nine of molecule C of Figure V-11 is excited. A hop of one quantum to a molecule above C along with the hop of a second quantum to one molecule below C will form an "activated" three-molecule linear chain.

The model has no adjustable parameters, other than that the results are constrained to pass through experimental points for pure H_2O and pure D_2O. The following assumptions are made:

Figure V-11

A tetrahedral cluster of hydrogen-bonded water molecules is shown.

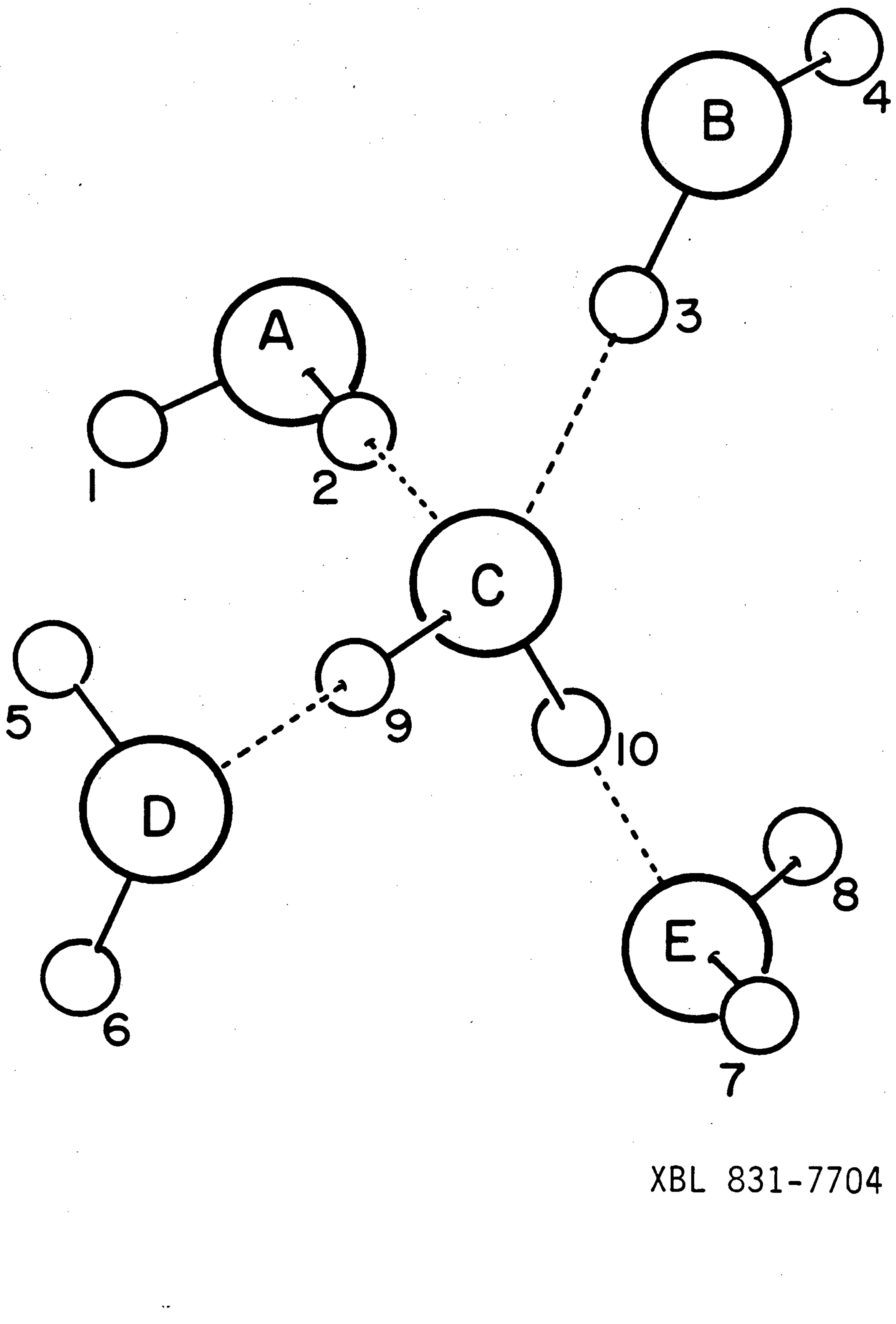

4
B
3
A
1
2
C
5
9
10
D
8
E
6
7

XBL 831-7704

(A) In order for reaction to occur, at least one quantum must be in each of three molecules in a linear chain. In other words, in molecules A, C, and E; A, C, and D; B, C, and E; or B, C, and D.

(B) An excited H_2O or an excited D_2O shares excitation among both bonds in the molecule. An excited HOD does not. This means that if an OH in HOD with the hydrogen represented by atom 9 in Figure V-11 is excited, then quanta cannot hop to molecule E because atom 10 is a deuterium.

(C) The rate of OL stretch transfer, k_{hop}, from H_2O^* or D_2O^* to bonds 2, 3, 5, 6, 7, and 8 is proportional to the number with the same isotope as the excited OL stretch. The * represents the initially excited molecule.

(D) Since HOD* does not share excitation between the OD and OH, the rate of transfer from HOD* is proportional to the number of bonds, 2, 3, 5, and 6 with isotopes identical to the excited bond.

The dependence of ϕ on the rate of energy transfer out of the initially excited bond depends on the relative rate of thermalization. If thermalization is fast compared to the hop rate, then the two hops necessary to activate the three-molecule chain before thermalization occur with probability proportional to $(k^i{}_{hop})^2 P_{i2}$. P_{i2} is the probability that for isotopic configuration, i, two quanta that randomly jump will form an activated three-molecule linear chain. The rate $k^i{}_{hop}$ is the hop rate for isotopic configuration, i. If the hop rate is fast compared to the relaxation rate, then ϕ is independent of the hopping rate and is proportional to P_{i2}.

Let the probability of isotopic configuration i be $P_{i1}(X_H)$. Let

$$P_{i2} = \frac{\text{No. of activated configurations for a hop of 2 quanta}}{\text{Total number of configurations for 2 quanta}} \tag{21}$$

and

$$k^{i}_{hop} = An_H \tag{22}$$

where n_H is the number of hydrogens on bonds 2, 3, 5, 6, 7, and 8 when an H_2O is excited, or the number on 2, 3, 5, and 6 for OH stretch excitation of an HOD molecule. A is a proportionality constant. Then the quantum yield for excitation of an OH or OD bond is

$$\phi_{OD}(1 - X_H) \propto \phi_{OH}(X_H) \propto \sum_i P_{i1}(k^{i}_{hop})^2 P_{i2} \tag{23}$$

if the hop rate is slow compared to the relaxation rate or

$$\phi_{OD}(1 - X_H) \propto \phi_{OH}(X_H) \propto \sum_i P_{i1}P_{i2} \tag{24}$$

if the hop rate is fast compared to the relaxation rate. The proportionality constants for OH or OD excitation are found by constraining values in pure H_2O and D_2O to the experimental result.

In addition, two other conditions were tested for the model providing the best fit of the data [Equation (23)].

(1) What if the quanta must remain in the OH bonds in the linear chain for reaction to occur? For instance, with molecules A, C, and D activated, if atom 1 or atom 10 of Figure V-11 is the same isotope as the initially excited bond, then reaction occurs with one-half the probability that it does when the atom is the opposite isotope. The reason is that if either of these atoms is the same isotope as that initially excited, then a quantum of stretch is shared equally between the two identical molecular O-L bonds and only one of these bonds is in the activated linear chain.

(2) What if the quanta need not remain in the linear bonded OH bonds but can be in any mode of the linearly bonded molecules?

Figure V-12, curves G and H show the results for excitation at 9400 cm^{-1} (three OH stretch or four OD) assuming an activated three-molecule chain is formed with probability $(k^{i}_{hop})^{2}P_{i}$. This is the model where thermalization competes effectively with the OH stretch hop. Curve G assumes the quanta must remain in the OH bonds of the linear chain, and curve H assumes that the energy need not remain in the OH stretch. The best fit is for curve H. The shape of the curve is correct, with the minimum at approximately the correct mole fraction, but the minimum is lower than the experimental points. The discrepancy is not severe for a model with no adjustable parameters. A greater quantum yield for HOD excitation relative to H_2O or D_2O would produce a better fit. This could arise from several sources which the model does not include:

(i) There could be a contribution from a thermal component, not requiring resonant transfer, which is approximately constant with hydrogen mole fraction.

(ii) A possible contribution from the next sphere of hydrogen-bonded water molecules was not included. Second sphere reactions favor H_2O, D_2O mixtures relative to the pure isotope because in order to form an activated reactant involving a second nearest neighbor molecule, both quanta that hop must leave the excited molecule through the same nearest neighbor H_2O. If an excited OH is surrounded by other OH's, then there is a $<$ one-third chance that the second quantum will leave the excited molecule by entering the same molecule the first quantum entered. If surrounded by only one OH and many other OD, the second quantum must leave through the single available OH.

(iii) HOD may not relax as rapidly as H_2O or D_2O because the bend overtone in HOD is not nearly as resonant with the OH stretch as is the case for H_2O or D_2O. This would raise the quantum yield for HOD relative to H_2O or D_2O and would raise the empirical curve closer to the experimental points.

The curve assuming a rapid hop rate compared to the thermalization rate, equation (24), with activation not constrained to the linearly bonded OH bonds, does not produce a satisfactory fit of the experimental data (Figure V-12b).

2. ϕ vs. T

If the contribution of the "bulk" mobility term is divided out of the quantum yield, the remainder, ϕ/μ decreases with increasing temperature. In other words, ϕ increases more slowly with T than does μ, the mobility. The k_{1a}/k_{-1a} term of Equation (16) will increase with increasing temperature. Therefore, either (1) the relaxation rate increases with temperature, or (2) the ion pair separation occurs at an effective temperature higher than ambient or both. The photon energy is greater than the endothermicity for the ion pair formation reaction. The excess energy could raise the effective temperature seen by the diffusing ion above the ambient temperature. Ten kcal of excess energy distributed over 100 modes, about 16 molecules, increases the temperature by about 50°C.

If the ions diffuse faster than the excess energy does, then the use of the ambient temperature is correct. If energy diffusion is faster than ionic diffusion, the excess photon energy can raise the temperature in

Figure V-12

Empirical curve (——) and experimental points (+) for ϕ/μ. Experimental points are for 9400 cm^{-1} excitation at 25 ± 1°C. Activation of the water ionization is by hopping of OH stretch quanta to neighboring molecules. The line (----) represents contribution from H_2O excitation, (—•—) from HOD excitation, and (—-—) from D_2O excitation.

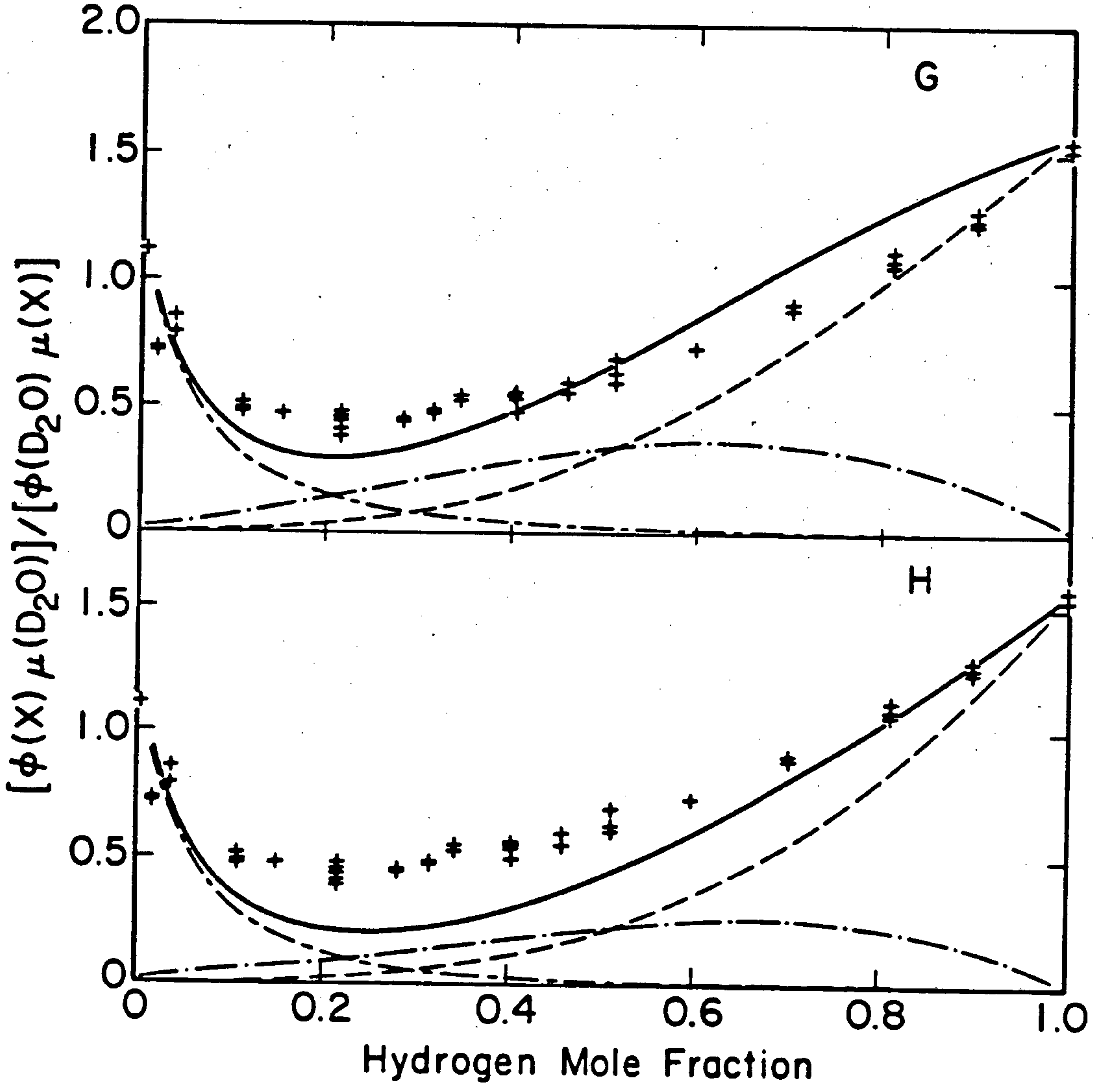
G
H
2.0
1.5
1.0
0.5
0
1.5
1.0
0.5
0
0
0.2
0.4
0.6
0.8
1.0
Hydrogen Mole Fraction
[φ(X) μ(D₂O)]/[φ(D₂O) μ(X)]

XBL 831-7710

Figure V-12b

Empirical curve (——) and experimental points (+) for ϕ/μ. Experimental points are for 9400 cm^{-1} excitation at 25 ± 1°C. Activation of the water ionization is by hopping of OH stretch quanta to neighboring molecules with a hop rate fast compared to the energy thermalization rate. The line (----) represents contribution from H_2O excitation, (—•—) from HOD excitation, and (—-—) from D_2O excitation.

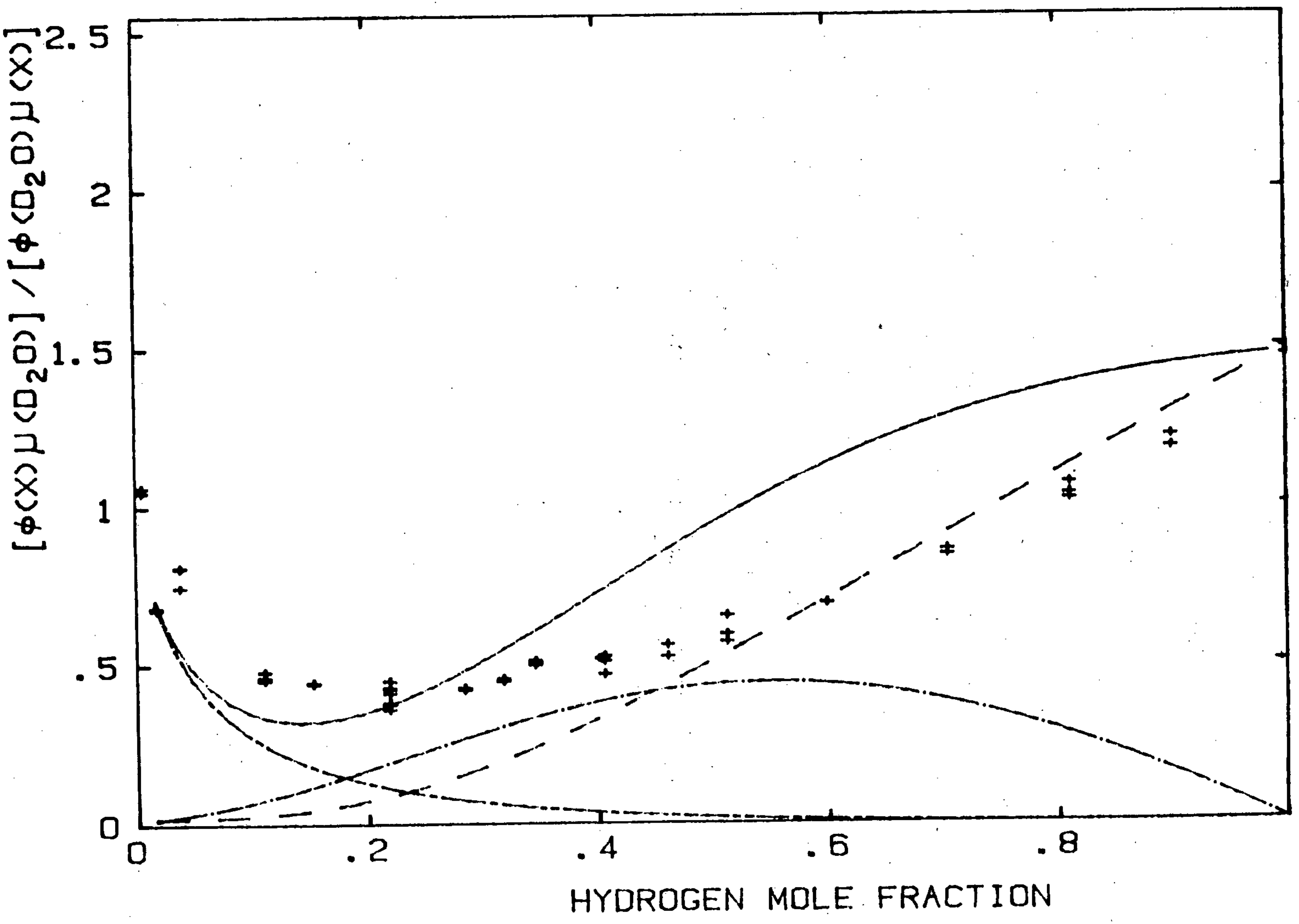
[ϕ(X)μ(D2O)]/[ϕ(D2O)μ(X)]
2.5
2
1.5
1
.5
0
0
.2
.4
.6
.8
HYDROGEN MOLE FRACTION

Figure V-13

The quantum yield divided by ionic mobility at a higher than ambient temperature as a function of temperature for excitation of liquid water near v = 3 OH stretch (●,+) and near v = 4 OH stretch (X,Δ,o). The mobility used is for 14°C higher than ambient for excitation near v = 3 and is 60°C higher than ambient for excitation near v = 4.

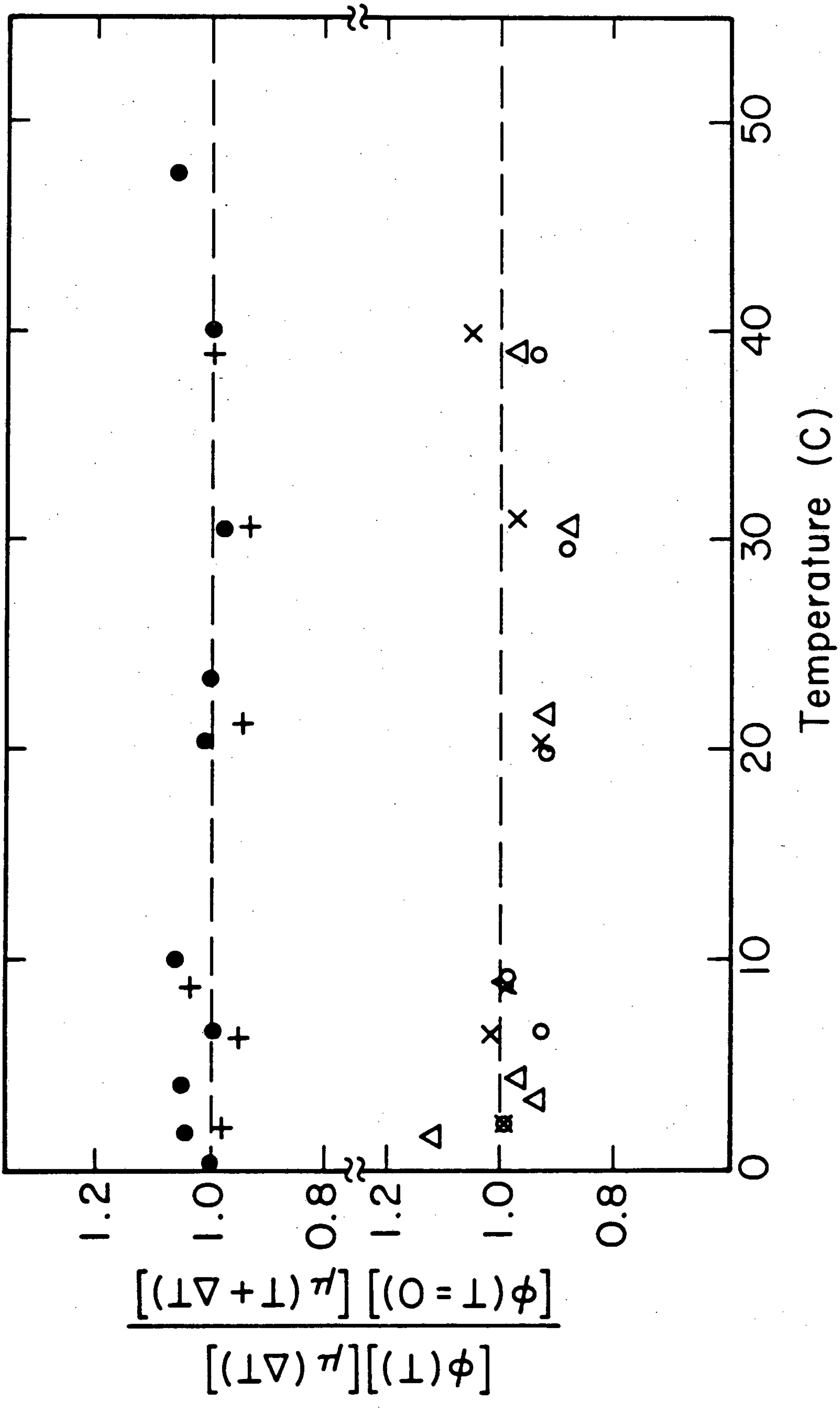
$\frac{[\phi(T)][\mu(\Delta T)]}{[\phi(T=0)][\mu(T+\Delta T)]}$
1.2
1.0
0.8
1.2
1.0
0.8
0
10
20
30
40
50
Temperature (C)

XBL 831-7715

the neighborhood of the diffusing ions above ambient. A thermal conductivity for water of 6.4 MW/cm K[48] yields a thermal diffusivity of 1.5×10^{-3} cm^2/sec, one order of magnitude greater than the 1.46×10^{-4} cm^2/sec diffusion coefficient for H^+ and OH^- ions. Figure V-13 shows that the temperatue dependence of the quantum yield could be attributed to ion pair separation at a temperature 14 degrees above ambient for excitation near $v = 3$ of the OH stretch or at a temperature 60 degrees above ambient for excitation near $v = 4$. More excess energy is available for excitation near $v = 4$ than for excitation near $v = 3$ ($\approx$ 7900 cm^{-1} versus 5000 cm^{-1}). Therefore, the effective temperature should be greater than for excitation near $v = 3$.

3. ϕ vs λ

The goal of this section is to characterize the experimental results. It is assumed that the ϕ vs λ dependence is dominated by the k_{1a}/k_{-1a} term described by equation (16). The actual dependence of the relaxation term, $1/(k_{1a} + k_2)$, on excitation energy is not known but is assumed to be negligible. The mobility term does not contribute. The previous section showed the effective temperature of the ion pair separation could be affected by the amount of excess photon energy. However, a change in effective temperature from 24.0°C to 70.0°C produces less than a factor of two increase in the ionic mobility compared to approximately two orders of magnitude increase in quantum yield over the 9400 cm^{-1} to ≈ 12,625 cm^{-1} wavelength range required to produce the corresponding effective temperature.

Equation (16) should be considered an empirical equation. Equation (16) is exact for a gas phase reaction where E_{zr}, ΔE_o, ν_i, and s have a well defined exact physical definition. In a liquid, these parameters are not physically well defined. They are dependent upon an unknown number of coupled vibrational modes of undetermined frequency. The approach will be (1) to define E_{zr}, ΔE_o, ν_i, and s for a hypothetical gas phase system, (2) to compare a gas phase system to a liquid phase system, and (3) to estimate reasonable relationships between E_{zr}, ΔE_o, and s for the liquid water system. Values are then inferred from the experimental data. E_{zr} is the reactant zero point energy, ΔE_o is energy from reactant to product well bottom, and s is the number of coupled modes. Thus, the equation must be considered empirical until experimental results from other systems confirm or deny any physical meaning for the parameters of the equation. Some concepts developed here may be applicable to unimolecular reactions of other large systems following non-statistical activation.

Consider a unimolecular gas phase isomerization system with two stable wells separated by a barrier. If a single molecule in the mixture is excited above the barrier, the fraction of excited population in each well is determined by the density of states ratio of Equation 16. The system is closed on the timescale of molecule collisions, with E_{zr} and s determined by the modes of the excited molecule. There are other modes present in the unexcited molecules of the system. These modes are not included in E_{zr} or s because they are not coupled to the excited molecule until a collision occurs.

Contrast this situation with the open system of the liquid water dissociative ionization reaction. The excited OH bond is coupled not only to the intramolecular modes, the local phonon (hindered translational), and local librational (hindered rotational) modes of the excited molecule, but also to most other H_2O molecules in the solution through an extensive network of strong hydrogen bonds. The number of modes, the mode frequencies, and the magnitude of ΔE_o is not obvious.

It is useful to break the system into two parts, one part being modes "strongly coupled" to the excited OH stretch, and one part being "weakly coupled". The system is then identical to the gas phase system in the limit of infinitesimal "weak coupling" and of "strong coupling" large enough to ensure energy randomization among strongly coupled modes at a rate rapid compared to

Figure V-14

Experimental points for the quantum yield versus excitation wavelength (o) along with several fits to $\phi = A(E_{ph} - E_o + E_{zr}/E_{ph} + E_{zr})^{s-1}$. The parameters used are $s = 9$, $E_{zr} = 1200\ \text{cm}^{-1}$, $E_o = 7041\ \text{cm}^{-1}$, and $A = 1.70 \times 10^{-3}$ (——); $s = 12$, $E_{zr} = 1000\ \text{cm}^{-1}$, $e_o = 5900\ \text{cm}^{-1}$, and $A = 1.60 \times 10^{-3}$ (---); and $s = 16$, $E_{zr} = 650\ \text{cm}^{-1}$, $E_o = 4734\ \text{cm}^{-1}$, and $A = 3.89 \times 10^{-3}$ (••••).

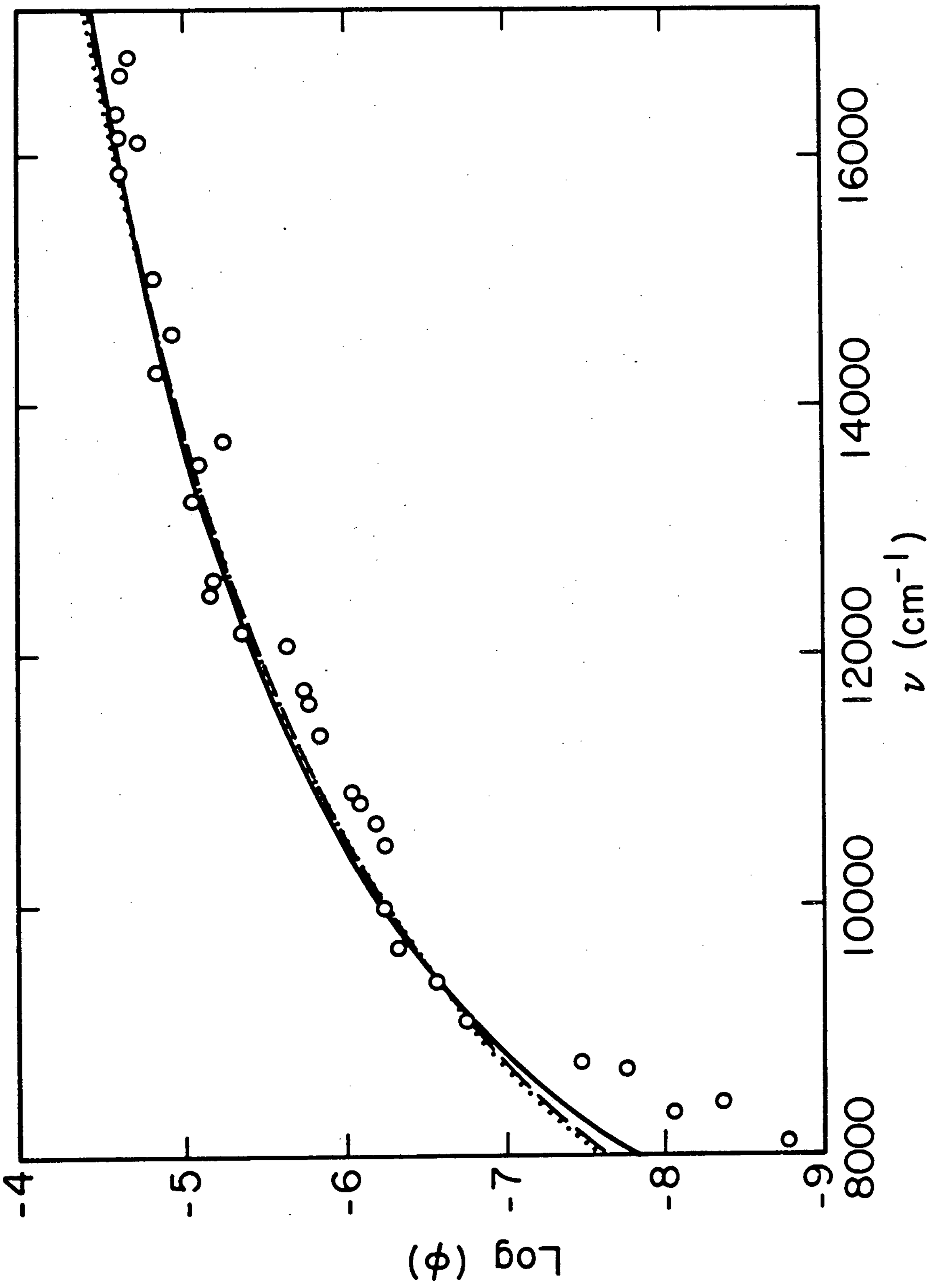

XBL 831-7717

the reaction rate. The identity of the strongly coupled modes depends on the details of the energy flow. The modes physically close to the excited molecule or with fundamental or overtones close in energy to the excited bond are expected to be strongly coupled. Since details of the energy flow are not known, the approach taken is to fit a curve with the form of Equation (16) to the data. The larger s is, the more modes involved. The larger E_z is for a given s, the higher the average mode frequency.

To determine ΔE_o, the laser reaction is compared to the thermal reaction (see Figure V-6). For a thermal reaction, ΔE_o is estimated from the ΔH for the thermal reaction and the zero point energies of reactants and products. If it is assumed that the thermal vibrational energy of reactant is equal to the vibrational energy of products, then ΔH is the same as the energy between reactant and product zero point, and

$$\Delta E_o = \Delta H + E_{zr} - E_{zp}. \qquad (25)$$

The quantity ΔE_o is unambiguous. Every mode which has an energy change upon going from reactant to product will contribute to ΔE_o. If modes are included in calculation of the zero point energies which do not experience a frequency change upon going from reactant to product, then there is no contribution to ΔE_o because $E_{zr} - E_{zp}$ is zero.

For the laser reaction, the modes which are coupled strongly are not necessarily the same modes which experience a frequency shift upon product formation. Only the modes strongly coupled to the excited bond should be included in the density of states calculation and should be included in calculation of ΔE_o. Thus, ΔE_o can range between ΔE_o(thermal) to ΔH depending on how many modes with a frequency shift are strongly coupled to the excited OH bond. If every mode with a frequency shift is strongly coupled to the excited O-H bond, then ΔE_o(laser) = ΔE_o(thermal). If no modes with a frequency shift are strongly coupled, then ΔE_o(laser) = ΔH.

The thermal value for ΔE_o is estimated from mode frequencies given by More O'Ferrall et al. for H_2O, H_3O^+ [49,50] and $OH^-(H_2O)_3$[51]. The frequencies are calculated from a molecular force field with force constants adjusted to match known experimental frequencies for H_2O, H_3O^+ [52-57], and $OH^-(H_2O)_3$[58-63]. Degeneracies and frequencies used in the zero point energy calculation are given in Table V-2. In H_2O, the zero point energy for ionic products is 25,480 cm^{-1} and 27,787.5 cm^{-1} for the reactant water. ΔE_o(laser) can range between $\Delta H = 4734\ cm^{-1}$ and ΔE_o(thermal) = 7041.5 cm^{-1}. The irregular dependence of ϕ with excitation energy requires a fit of quantum yields with excitation at equivalent points in successive OH stretch bands. Quantum yields at 6700 cm^{-1}, 9983 cm^{-1}, 13,240 cm^{-1}, and 16,500 cm^{-1}, corresponding to excitation

Table V-2

Frequencies[a] used in zero point energy calculation

H_3O^+		$(H_2O)_3OH^-$	
degeneracy	frequency (cm^{-1})	degeneracy	frequency (cm^{-1})
1	2840	1	3670
2	2540	2	1025
1	1140	3	2790
2	1630	3	3440
1	580	3	1560
2	610	1	750
3	200	2	585
		1	450
		2	440
		3	500
		12	200

[a] Most frequencies are given by Kresge _et_ _al_. Phonon frequencies are taken to be 200 cm^{-1}.

Three librational frequencies of 500 cm^{-1} are assumed for the hydroxide ion.

of v = 2, 3, 4, and 5, respectively, are used. Figure V-14 shows a best fit of the experimental points to Equation (16) for values of ΔE_o (laser) equal to 4734 cm^{-1}, 5900 cm^{-1}, and 7041.5 cm^{-1}. Satisfactory fits (within about 20%) were obtained for s ranging between 8 and 16, and E_z ranging between 650 cm^{-1} (the lowest allowed E_z) and 2000 cm^{-1}.

If the values of s and E_{zr} obtained from the fit have physical significance, then in the limit of a large distinction between strongly- and weakly-coupled modes, 8 to 16 modes are strongly coupled and the average energy of the modes is between 160 cm^{-1} and a few hundred cm^{-1}. The number of strongly-coupled modes is about one-third to one-half the total number of modes in a three or four molecule linear chain.

Knight *et al.*[64] used an expression of the form

$$\phi = A[(E - E_a)/E]^s \tag{26}$$

to fit the temperature and wavelength dependence of the quantum yield, where E is the photon energy, E_a is the barrier, s is the number of coupled modes, and A is a proportionality constant. The temperature dependence in this model comes from the temperature dependence of E_a. Additional temperature dependence expected from the ion pair separation step is not included in the Knight model.

There are several important differences between the Knight model, and the model reported here. Knight assumes an RRK reaction rate with an exponential energy relaxation.

The activation energy is given by ΔH, the reaction endothermicity. They assume recombination in the ion pair is negligible. The high level of excitation and low reverse barrier for geminate recombination suggest that recombination may be important. The model reported here assumes recombination in the ion pair is rapid enough to produce local equilibrium. Also, the relaxation rate is assumed to be constant or weakly dependent on the level of excitation.

In spite of the differences between the model reported here and Knight's model, the resulting expressions are similar. The value Knight found for of s, the number of coupled modes, is 8.4; within the 8-16 range determined here.

The fit of the experimental data to equation (16) can be used to estimate if bend excitation is as efficient as stretch excitation in producing the vibrationally activated reaction. Between 50% and 80% of the absorption at the stretch and bend combination band near 11,800 cm^{-1} is from underlying v = 3 O-H stretch excitation. Equation 16 predicts a quantum yield of 5.7×10^{-7} for excitation of pure v = 3 OH stretch and 2.7×10^{-6} for pure excitation of the 3 stretch + 1 bend combination. Thus, the predicted quantum yield at 11,800 cm^{-1} is between 1.64×10^{-6} and 1.0×10^{-6}. This compares to a measured quantum yield of 1.75×10^{-6}. Within experimental error, excitation of the bend is as efficient as excitation of the stretch.

One additional model for the photon energy dependence of the quantum yield was tested. If the vibrationally activated laser reaction comes about from a small locally hot region near the initially absorbed photon, then one might expect a Boltzmann quantum yield dependence,

$$\phi = A \exp\left(-\Delta H n / E_{\lambda}\right), \tag{27}$$

where E_{λ} is the available energy imparted by the photon, ΔH is the enthalpy change for the ionization reactions, and n is the number of modes sharing the energy. The energy available for the ion pair formation reaction is the full photon energy, E_{ph} plus thermal energy, nRT. If the recombination reaction is rapid enough to achieve equilibrium, the energy available for recombination is the photon energy plus thermal energy minus the endothermicity, $E_{ph} - \Delta H + nRT$. Thus, the correct energy to use in equation (27) is between $E_{ph} + nRT$ and $E_{ph} - \Delta H + nRT$. Figure V-15 shows the photon energy dependence predicted by equation (27) for $E_{\lambda} = E_{ph} + nRT$ and $E_{\lambda} = E_{ph} - \Delta H + nRT$ along with the experimental points. The prediction is made by constraining equation (27) to match experimental values at 16,500 cm^{-1} and 13240 or 9983 cm^{-1}. With the curve constrained to go through the 13240 cm^{-1} point, the best fit is with $A = 6.91 \times 10^{-3}$ and $n = 23.5$ for $\Delta H = 5075$ cm^{-1} (14.5 kcal) when $E_{\lambda} = E_{ph} + nRT$. The best fit is $A = 5.27 \times 10^{-4}$ and $n = 7.85$ for $\Delta H = 5075$ cm^{-1} when $E_{\lambda} = E_{ph} - \Delta H + nRT$. When the curve is constrained to match experimental points at 9983 cm^{-1}, no real solution exists with $E_{\lambda} = E_{ph} + nRT$.

For $E_\lambda = E_{ph} - \Delta H + nRT$, the best fit is with $A = 1.38 \times 10^{-3}$ and $n = 10.76$. The small value for n in each case supports the hypothesis that a small number of water molecules is involved as was found in the other wavelength dependence models. The curve with $E_\lambda = E_{ph} - \Delta H + nRT$ matches the experimental points more closely than $E_\lambda = E_{ph} + nRT$.

Figure V-15

Experimental points at 10 ± 1°C for the quantum yield versus excitation wavelength, (o), along with three fits to $\phi = A \exp(-\Delta H n/E_\lambda)$, where $\Delta H = 5075\ cm^{-1}$ (14.5 kcal). The parameters used are $A = 6.91 \times 10^{-3}$ and $n = 23.5$ (——) for $E_\lambda = E_{ph} + nRT$. The parameters are $A = 5.27 \times 10^{-4}$ and $n = 7.85$ for $E_\lambda = E_{ph} - \Delta H + nRT$, (---). The curve (—-- —) is $A = 1.38 \times 10^{-3}$ and $n = 10.76$, with $E_\lambda = E_{ph} - \Delta H + nRT$.

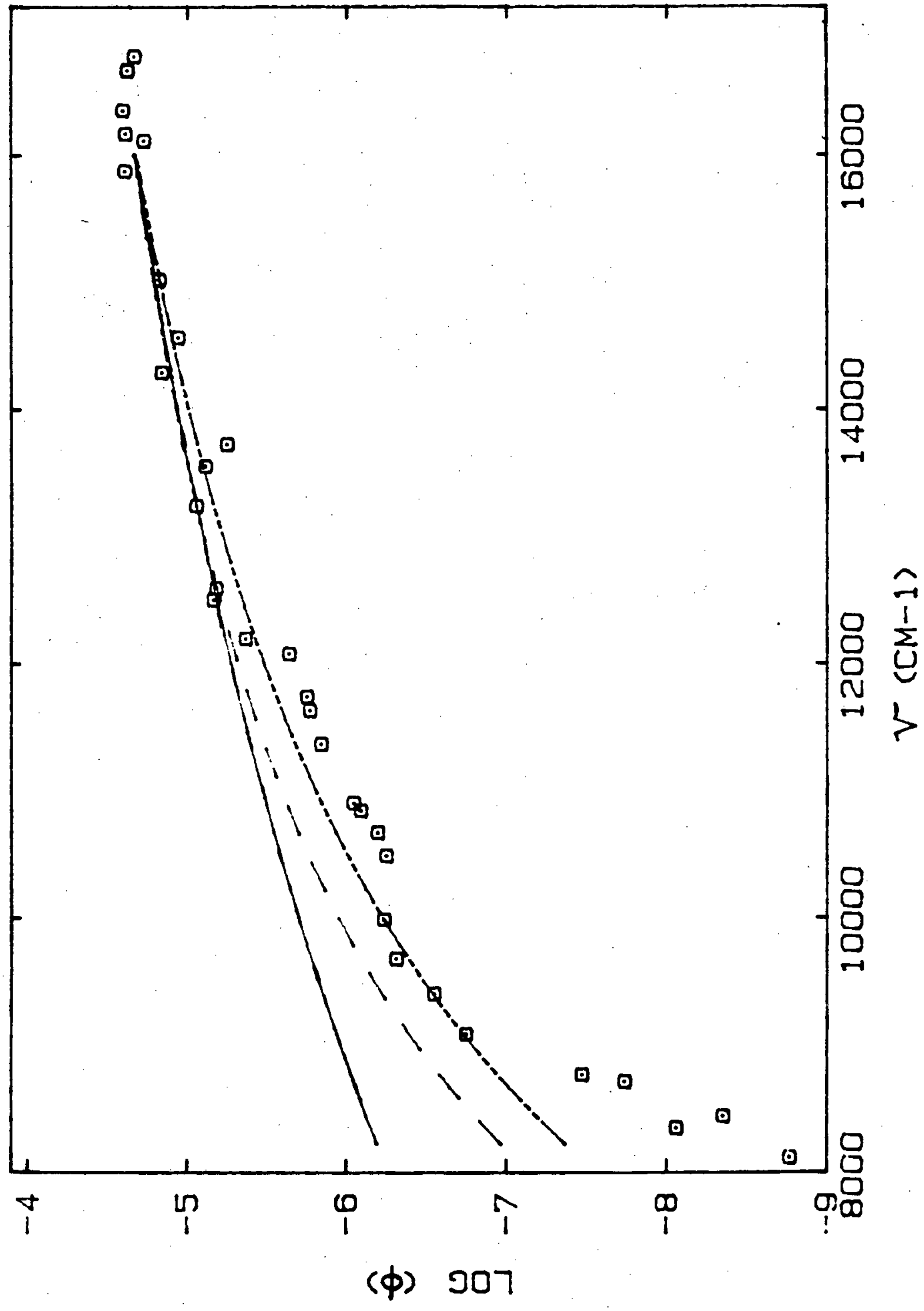
LOG (Φ)
-4
-5
-6
-7
-8
-9
8000
10000
12000
14000
16000
ν (CM-1)

1. M. Eigen and L. De Maeyer, Z. Elektrochem. 59, 986 (1955)
2. M. Eigen and L. De Maeyer, Proc. Roy. Soc. (London), Ser. A 247, 505 (1958)
3. J.F. Holzwarth, W. Frisch, A.J. Kresge and D.M. Goodall, to be published
4. G.A. Vidulich, D.F. Evans, and R.L. Kay, J. Phys. Chem. 71, 656 (1967)
5. V.G. Ertl and H. Gerischer, Z. Elektrochem., 66 560 (1962)
6. G.C. Barker, P. Fowles, D.C. Sammon, and B. Stringer, Trans. Faraday Soc. 66, 1498 (1970)
7. A.H. Narten, M.D. Danford, and H.A. Levy, Disc. Faraday Soc. 43, 97 (1967)
8. D. Hankins, J.W. Moskowitz, and F.H. Stillinger, J. Chem. Phys. 53, 4544 (1970); Erratum, 59, 995 (1973)
9. J. O'M. Bockris and A.K.N. Reddy, "Modern Electrochemistry" v. 1, Plenum, New York (1979) Chapter 5
10. F.H. Stillinger in "Theoretical Chemistry; Advances and Perspectives", v. 3, Academic Press, New York (1978)
11. R. Triolo and A.H. Narten, J. Chem. Phys 63, 3624 (1975)
12. I. Olovsson, J. Chem. Phys. 49, 1063 (1968)
13. J.-O. Lundgren and I. Olovsson, Acta Crystallogr. 23, 966, 971 (1967)

14. J.-O. Lundgren and I. Olovsson, J. Chem. Phys. 49, 1068 (1968)

15. R.A. Bell, G.G. Christoph, F.R. Fronczek, and R.E. Marsh, Science 190, 151 (1975)

16. M.D. Newton and S. Ehrenson, J. Am. Chem. Soc. 93, 4971 (1971)

17. G. Beurskens and G.A. Jeffrey, J. Chem. Phys. 41, 924 (1964)

18. R.K. McMullan, T.C.W. Mak, and G.A. Jeffrey, J. Chem. Phys. 44, 2338 (1966)

19. R.A. More O-Ferrall in "Proton Transfer Reactions" E.F. Caldin and V. Gold eds., Chapman and Hall, London (1975) pp. 218, 320

20. S.A. Rice and M.G. Sceats, J. Phys. Chem. 85, 1108 (1981)

21. M.G. Sceats and K. Belsley, Mol. Phys. 40, 1389 (1980)

22. M.F. Vernon, D.J. Krajnovich, H.S. Kwok, J.M. Lisy, Y.R. Shen, and Y.T. Lee, J. Chem. Phys., submitted

23. N. Koroteev, M. Endemann, and R. Byer, Phys. Rev. Lett. 43, 398 (1979)

24. J. Arnold and D.J. Millen, J. Chem. Soc., 503 (1965)

25. J.E. Bertie and D.J. Millen, J. Chem. Soc., 497 (1965)

26. C.A. Coulson and G.N. Robertson, Proc. R. Soc. Lond. A 342, 289 (1975)

27. Y. Bouteiller and Y. Guissani, Mol. Phys. 38, 617, (1979)

28. L.E. Brus and V.E. Bondybey in "Radiationless Transitions", Academic Press, S.H. Lin, ed. (1980)

29. B.S. Rabinovitch and D.W. Setser, Advan. Photochem. 3, 1 (1964)

30. W.J. Albery in "Proton Transfer Reactions", Chapman and Hall, E.F. Caldin and V. Gold, eds. (1975)

31. M. von Smoluchowski, Phys. Z. 17, 557, 585 (1916)

32. M. von Smoluchowski, Z. Physik. Chem. (Leipzig) 92, 129 (1917)

33. L. Onsager, J. Chem. Phys. 2, 599 (1934)

34. K.M. Hong and J. Noolandi, J. Chem. Phys. 68, 5163 (1978)

35. reference 9, chapter 4, equation 4.169.

36. reference 9

37 P.J. Robinson and K.A. Holbrook, "Unimolecular Reactions" Wiley-Interscience, London, (1972), section 5

38. David W. Oxtoby in "Photoselective Chemistry", Adv. Chem. Phys., v. XLVII pt. 2, p. 487

39. R.R. Alfano and S.L. Shapiro, Phys. Rev. Lett. 29, 1655 (1972)

40. A. Fendt, S.F. Fischer, and W. Kaiser, Chem. Phys. 57, 55 (1981)

41. A. Fendt, S.F. Fischer, and W. Kaiser, Chem. Phys. Lett. 82, 350 (1981)

42. A. Laubereau, S.F. Fischer, K. Spanner, and W. Kaiser, Chem. Phys. 31, 335 (1978)

43. S.A. Rice and M.G. Sceats, J. Phys. Chem. 85, 1108 (1981)

44. R. McGraw, W.G. Madden, M.S. Bergren, S.A. Rice, and M.G. Sceats, J. Chem. Phys. 69, 3483 (1978)

45. W.G. Madden, M.S. Bergren, R. McGraw, S.A. Rice, and M.G. Sceats, J. Chem. Phys. 69, 3497 (1978)

46. M.S. Bergren and S.A. Rice, J. Chem. Phys. 77, 583 (1982)

47. E.B. Wilson, J.C. Decius, and P.C. Cross, "Molecular Vibrations", McGraw Hill, New York (1955) section 8.5

48. Handbook of Chemistry and Physics, 53rd Edition p. E-11

49. R.A. More O'Ferrall, G.W. Koeppl, and A.J. Kresge, J. Am. Chem. Soc. 93, 1 (1971)

50. R.A. More O'Ferrall, G.W. Koeppl, and A.J. Kresge, J. Am. Chem. Soc. 93, 9 (1971)

51. R.A. More O'Ferrall and A.J. Kresge, J.C.S. Perkin II, 1840 (1980)

52. G.E. Walrafen, J. Chem. Phys. 47, 114 (1967)

53. G.E. Walrafen, J. Chem. Phys. 48, 244 (1968)

54. G.E. Walrafen in "Hydrogen-Bonded Solvent Systems", A.K. Covington and P. Jones, eds., Taylor and Francis, London, (1968), p. 9

55. R.E. Weston, Jr., Spectrochim. Acta 18, 1257 (1962)

56. P.A. Giguere, Rev. Chim. Miner. 3, 627 (1966)

57. K. Heinzineger and R.E. Weston, Jr., J. Phys. Chem. 68, 744 (1964)

58. L.H. Jones, J. Chem. Phys 22, 217 (1954)

59. I. Gennick and K. Harmon, Inorg. Chem. 14, 2214 (1975)

60. E. Drouard, Compt. rend. 247, 68 (1958)

61. J.O. Clifford, J.A.S. Smith, and F.A. Temme, J.C.S. Faraday 11, 1352 (1975)

62. P. Rhine, D. Williams, G.M. Hale, and M.R. Querry, J. Phys. Chem. 78, 1405 (1974)

63. W.R. Busing and D.F. Hornig, ibid, 65, 284 (1961)

64. B. Knight, D.M. Goodall, and R.C. Greenhaow, J. Chem. Soc. Faraday 2 75, 841 (1979)

CHAPTER VI. CONCLUSIONS

The conclusions are divided into two parts: (A) major conclusions based on the thermal equilibrium relaxation rate; and (B) major and minor conclusions based on quantum yields for the vibrationally activated reaction.

I. Thermal Recombination Reaction

The recombination distance is constant with isotopic composition and temperature with a distance of 5.80 ± 0.5 Å. The activation energy for the recombination reaction is 3.5 kcal/mole.

II. Vibrationally Activated Reaction

First, the model independent conclusions will be given. The major model independent conclusion is that single photon overtone excitation can be used to vibrationally activate a liquid phase reaction. Excited liquid water transfers a proton to form H_3O^+ and OH^-. The quantum yield has the same general wavelength dependence for excitation of H_2O or D_2O, but is shifted to lower quantum yields in D_2O. The hydrogen mole fraction dependence of the quantum yield and the wavelength dependence for $v = 3$ OH stretch or $v = 4$ OD stretch excitation in 0.017 mole fraction hydrogen in D_2O is consistent with a lower quantum yield for HOD excitation in D_2O than for D_2O excitation in D_2O. A temperature increase causes a smaller fractional quantum yield increase for large excitation energies than for small excitation energies. The constancy of quantum yield with wavelength across an OH stretch absorption band results from one of two possibilities depending on the source of broadening in the absorption band. If the broadening comes from differences in liquid structure, then the quantum yield is independent of those structural differences. If the broadening comes from combination excitation of low frequency lattice motions, then excitation of lattice motions does not produce reaction products as efficiently as the equivalent energy in O-H stretch motions.

The major model dependent result is that the minimum in the quantum yield as a function of hydrogen mole fraction results from an increase in relaxation rate or from an unfavorable change in the relaxation pathway for HOD in D_2O. The two possibilities cannot be distinguished. In addition, the diffusive ion pair separation probably occurs at an effective temperature higher than ambient. An empirical fit of the quantum yield versus wavelength was given. In the limit of large distinction between strongly and weakly coupled modes, the fit shows about one-third to one-half of the modes in a 3-4 molecule linear chain are strongly coupled, and the zero point energy involves modes with low average frequency. The physical validity of the fit must be tested by experiments on other systems. Excitation of bend modes is as efficient in producing the vibrationally activated reaction as excitation of stretch.

APPENDIX A

This sections demonstrates that the absolute transient voltages are independent of the position and intensity distribution of the illuminated region for a uniform interelectrode electric field. Figure A-1 shows a schematic diagram of the interelectrode region and the equivalent electrical circuit. Region 2 is the illuminated region.

It is easy to show the relative signal magnitudes are independent of the position of the illuminated region. The following statements hold independent of position.

1. The temperature change in the illuminated region is constant.
2. The number of ions produced by the laser reaction is constant.
3. The change in ionic conductivities and equilibrium H^+ and OH^- concentrations produced by the temperature increase is constant.

Therefore, the changes in solution conductivity and the relative magnitude of the transient voltage peak and baseline step are independent of the position of the illuminated region.

The absolute transient voltage change is also independent of position, spot size, and intensity profile for a uniform interelectrode electric field. In all experiments, the illuminated region is ϕ, the central interelectrode region where the electric field is most

Figure A-1

A schematic diagram of the interelectrode region of the illuminated electrode pair, and the equivalent electrical circuit.

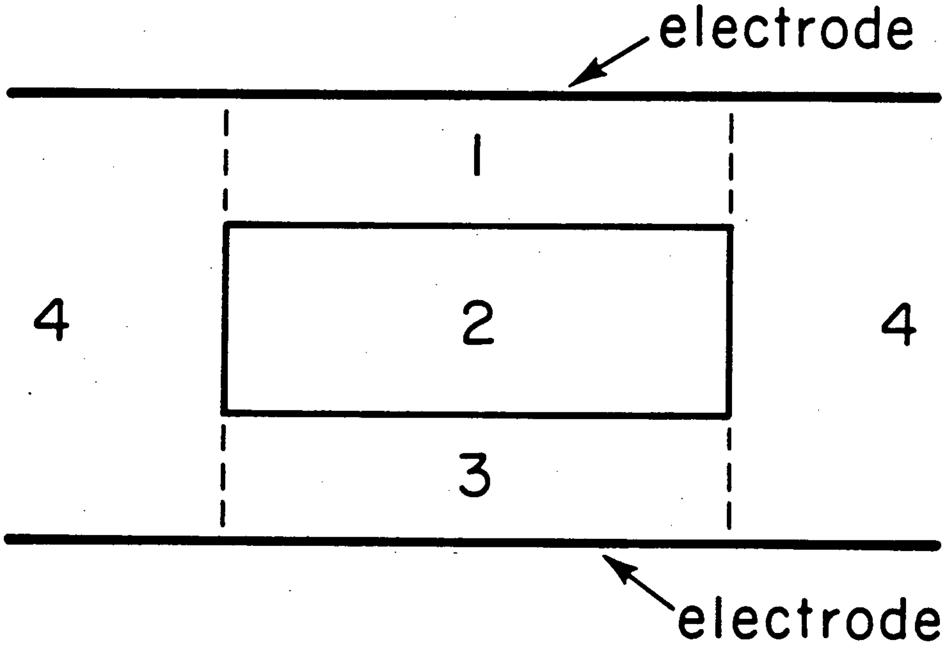
electrode
1
4
2
4
3
electrode

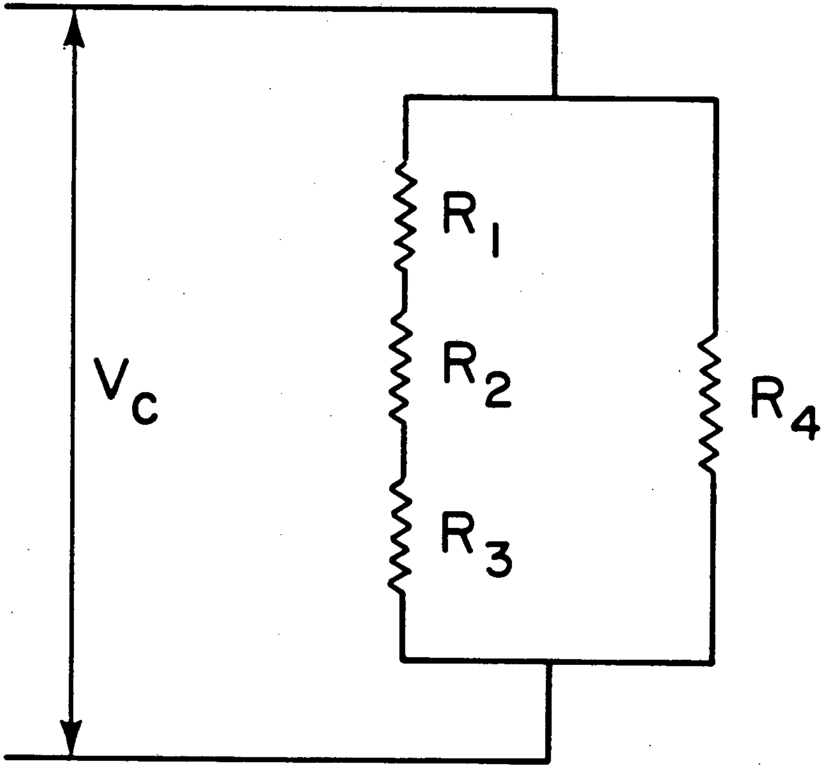
V_c
R_1
R_2
R_3
R_4

XBL 831-7708

uniform. Field uniformity means that resistances are dependent only upon geometry. The resistance, $R = \ell/AL$. L is the solution conductivity in the region of interest, A is the area of the face parallel to the electrode and ℓ is the thickness.

Referring to the circuit equivalent of the electrode pair shown in Figure A-1, the total resistance of the electrode is $RC2 = R_4(R_1 + R_2 + R_3)/R_1 + R_2 + R_3 + R_4$. The quantity of interest is the current change given a change in resistance of the illuminated region. Equation (32) of the analysis section gives

$$i_c = V_c/RC2 \tag{1}$$

where i_c is the current through the cell of resistance RC2 given an applied voltage of V_c. The current change is

$$\Delta i_c = \frac{d\ V_c/RC2}{d\ R_2} \Delta R_2 \tag{2}$$

Replacing RC2 and taking the derivative, (2) becomes

$$\Delta i_c = \frac{-V_c}{(R_1 + R_2 + R_3)^2} \quad \Delta R_2 \tag{3}$$

Replacing the resistances with $R = \ell/AL$, and using $1 - [1/(1 + X)] \cong X$ for small X,

$$\Delta i_c = \frac{-V_c\ \ell_2\ A}{(\ell_1 + \ell_2 + \ell_3)^2} \Delta L \tag{4}$$

Equation (4) shows the absolute signal magnitude is constant with constant interelectrode spacing,

$(\ell_1 + \ell_2 + \ell_3)$, and irradiated spot thickness, ℓ_2. The signal is independent of position, i.e., the relative value of ℓ_1 and ℓ_3.

If the temperature increase is linear in the absorbed energy density and if also, the ionic conductivity and K_w is linear in temperature, then the absolute signal magnitude is independent of spot size and beam profile because ΔL is then inversely proportional to the irradiated volume, $\ell_2 A$, or $\Delta L \propto \Delta E/\ell_2 A$ where ΔE is the total absorbed energy. Half the spot size implies twice the temperature increase, twice the transient ion concentration, and, therefore, twice the conductivity change, ΔL in the illuminated region. Equation (4) becomes

$$\Delta i \propto \frac{-V_c}{(\ell_1 + \ell_2 + \ell_3)^2} \quad \Delta E \tag{5}$$

Equation (5) is independent of spot size and therefore intensity profile. Since the absorbed energy density and resulting temperature increase is small, a linear tempertature, linear ionic conductivity, and linear K_w with absorbed energy density are excellent approximations.

Appendix B - ABQMHD.WES

Program to calculate the quantum yield for dissociative ionization of water in an arbitrary isotopic mixture.

This program calculates the quantum yield from both the measured transient voltage step and from the absorbance and transmitted laser energy. Comments for the program and subroutine functions, a definition of variables used in the program, and the program text are given.

A. Program comments

10	Open a file for hard copy output
15	Open an output file for results
50-450	Input data
460-480	Calculate quantum yields, and write the intermediate results to the hard copy output file
490	Form hardcopy and output files for final quantum yield results based on the transient voltage step and for quantum yield results based on the absorbance and transmitted energy.

B. Subroutine function

500	Calculate quantum yield
860-990	Initialize variables

1230 & 1810	Read raw data for analysis
1440	Input routine for the thermocouple voltage
1540	Input routine for the wavelength
1740	Input routine for the monitor voltage
1910	Open an output file
3400	Read data from a previously analyzed file for re-analysis

C. Definition of variables

A1	absorbance of water
A2	factor for calculating the baseline step from absorption spectra
A6	conductivity step from absorbance and transmitted laser energy
A8	conductivity step from transient voltage step
A9	conductivity jump
B7	total conductivity jump-thermal jump, or portion of jump caused by the laser induced reaction (based on the absorbance and transmitted laser energy)
B9	total conductivity jump-thermal jump, or portion of jump caused by the laser induced reaction (based on the transient voltage step)
D1	HDO mole fraction
D2	D_2O mole fraction

D3	density of water as a function of hydrogen mole fraction
D4	dK_w/dT for D_2O
D5	dK_w/dT for H_2O
D6	temperature jump from absorbance and transmitted laser energy
D7	dK_w/dT for an arbitrary isotopic mixture
D8	temperature jump from transient voltage step
D9	$d[L_3O]/dT$
G1	post cell amplifier gain
H0	parameter for H_3O^+ molar conductivity
H1	parameter for H_3O^+ molar conductivity
H2	parameter for H_3O^+ molar conductivity
H3	H_2O mole fraction
H4	ΔH_o for an arbitrary temperature and isotopic composition
Q	energy of 1 mole of photons/specific heat capacity
H	theoretical $[L_3O^+]$, hydronium ion concentration
K4	reference cell constant
K7	K_w for D_2O as a function of temperature
K8	K_w for H_2O as a function of temperature
K9	K_w for water as a function of temperature and isotopic composition
K	signal cell constant
L4	excitation wavelength
L5	laser setting

L	experimental conductivity of solution
M4	$d\lambda(L_3O^+ + OL^-)/dT$ in an arbitrary isotopic mixture
M5	$d\lambda(Na^+ + Cl^-)/dT$ in an arbitrary isotopic mixture
M6	mole fraction hydrogen
M7	ionic conductivity of $H_3O^+ + OH^-$ at 25°C as a function of hydrogen mole fraction
M8	ionic conductivity of $H_3O^+ + OH^-$ as a function of temperature and hydrogen mole fraction
M	relaxation rate of the thermal equilibrium
NO	parameter for NaCl molar conductivity
N1	parameter for NaCl molar conductivity
N2	parameter for NaCl molar conductivity
N3	D_2O viscosity
N9	experimental $[Na^+]$ and $[Cl^-]$ from excess conductivity above the theoretical $(L_3O^+ + OL^-)$ conductivity
P1	transmitted laser power
P4	mixture purity
Q7	quantum yield based on the absorbance and transmitted laser energy
Q9	quantum yield based on the transient voltage step
Q	energy of 1 mole of photons/specific heat capacity

R1	total resistance on the illuminated side of the conductivity bridge
R9	feedback resistance for the cell amplifier operational amplifier
R	cell resistance
S1	$d\lambda(Na^+ + Cl^-)/dT$ in H_2O
S2	ionic conductivity of $Na^+ + Cl^-$ in D_2O as a function of temperature
S3	ionic conductivity of Na^+ and Cl^- in H_2O as a function of temperature
S	ionic conductivity of Na^+ and Cl^- as a function of temperature and hydrogen mole fraction
T8	thermocouple voltage
T	temperature
V1	monitor voltage
V2	transient jump voltage
V3	transient step voltage
V4	recorded transient voltage step
V5	recorded transient voltage jump above the final baseline

Real voltages are one-half the recorded voltages because the recorded waveform is the waveform at positive polarity minus the waveform at negative polarity. Also, the real transient jump includes the baseline step.

V8	transient step voltage calculated from absorbance and transmitted laser energy

V	applied voltage
W0	parameter for ln K_w (H_2O) vs. temperature
W1	parameter for ln K_w (H_2O) vs. temperature
W2	parameter for ln K_w (H_2O) vs. temperature
X1	$d\lambda(H_3O^+)/dT$ in H_2O
Y0	parameter for OH^- molar conductivity
Y1	parameter for OH^- molar conductivity
Y2	hydroxide ionic conductivity in H_2O

D. Program listing (see pages 232-236)

```
10 OPEN #5 AS 'MULDEC.WES' FOR WRITE
15 GOSUB 1910
20 PRINT 'ENTER NO OF FILES'
30 INPUT J3
40 LET EM=1
50 DIM T(J3),V2(J3),V1(J3),L4(J3),V3(J3)
60 DIM A(511)
70 DIM V4(J3),V5(J3),D8(J3),P4(J3),H4(J3),Q9(J3)
80 DIM H5(J3),N5(J3),V8(J3),L5(J3)
90 DIM M6(J3),T8(J3),M(J3)
92 DIM D6(J3),Q7(J3)
95 DIM A1(J3),P1(J3),A2(J3)
96 A2=1.7E-03
100 LET T=0\LET V2=0\LET V1=0\LET V3=0\LET M=0\LET L4=0
110 LET V4=0\LET V5=0\LET D8=0\LET P4=0\LET H4=0\LET Q9=0
130 LET H5=0\LET N5=0\LET V8=0\LET T8=0\LET L5=0
132 PRINT 'IF REANALYZING A PREVIOUSLY ANALYZED FILE, TYPE 1'
134 INPUT Z3
136 IF Z3=1 THEN GOSUB 3400
137 IF Z3=1 THEN GOTO 155
138 GOSUB 1230
155 IF Z3=1 THEN GOTO 306
160 PRINT 'ENTER TC VOLTAGE IN UVOLTS  IF SEVERAL FILES HAVE THIS'
170 PRINT 'VOLTAGE ENTER NEG VOLTS'
180 FOR N4=1 TO J3
190 GOSUB 1420
200 NEXT N4
210 PRINT 'ENTER MONITOR VOLTAGE  IF SEVERAL FILES HAVE THIS'
220 PRINT 'VOLTAGE ENTER NEGATIVE MONITOR VOLTAGE'
230 FOR N4=1 TO J3
240 GOSUB 1720
250 NEXT N4
260 PRINT 'ENTER DYE LASER FREQ SETTING AND ENTER 0,1OR 2 FOR'
270 PRINT '1ST ,2ND OR 0 STOKES IN H2. -1 OR -2 FOR CH4'
280 FOR N4=1 TO J3
290 GOSUB 1520
300 NEXT N4
302 PRINT 'ENTER MOLE FRACTION HYDROGEN'
303 FOR N4 = 1 TO J3
304 INPUT M6(N4)
305 NEXT N4
306 PRINT 'ENTER ABS,I,A'
307 FOR N4=1 TO J3
308 PRINT 'FILE',N4,'ABS,I,A'
309 INPUT A1(N4),P1(N4)\A1(N4)=A1(N4)/10
310 NEXT N4
311 PRINT 'FILE','ABS','I','A'
312 FOR N4=1 TO J3
313 PRINT N4,A1(N4),P1(N4),A2(N4)
314 NEXT N4
315 WAIT
316 PRINT
320 PRINT 'TC VOLT    TEMP         MON         LASER SET   LAMBDA      FILE'
330 FOR N4=1 TO J3
340 PRINT T8(N4),T(N4),V1(N4),L5(N4),L4(N4),N4
350 NEXT N4
360 PRINT 'WHICH COLUMN DO YOU WANT TO CHANGE? 0 IS NO CHANGE'
370 PRINT 'CHOOSE 1, 3 OR 4'
380 INPUT Q5
390 PRINT 'WHICH FILE DO YOU WISH TOCHANGE?'
400 INPUT N4
410 IF Q5=1 THEN GOSUB 1440
420 IF Q5=3 THEN GOSUB 1740
430 IF Q5=4 THEN GOSUB 1540
440 IF Q5=0 THEN GOTO 460
```

```
450 GOTO 360
460 FOR J2=1 TO J3
470 GOSUB 500
471 PRINT\PRINT #5,'FILE',J2
472 PRINT #5,M6(J2),T(J2)
473 PRINT #5,X2,H3,D1,D2,M7,M8
474 PRINT #5,S3,N3,S2,S,K7,K8
475 PRINT #5,K9,D3,H6,Q,D4,D5
476 PRINT #5,D7,H,D9,X1,S1,M5
477 PRINT #5,M4,L,A8,A9,B9,A6
478 PRINT #5,B7
479 PRINT #5,
480 NEXT J2
485 T3=0
490 GOTO 1000
500 IF J2=1 THEN GOTO 860
510 LET X2=H0+H1*T(J2)+H2*T(J2)*T(J2)
515 DELETE R
517 H3=M6(J2)^2
518 D1=2*M6(J2)-2*H3
519 D2=1-H3-D1
520 M7=H3*548.9+D1*411.2+D2*363.4
530 LET Y2=Y0+Y1*T(J2)
535 T2=(X2+Y2)/547.48
536 M8=M7*T2
540 LET Z=Z0+Z1*T(J2)
550 LET S3=N0+N1*T(J2)+N2*T(J2)*T(J2)
552 N3=EXP(669.2/(T(J2)+273.16-133.98)-3.966)
553 S2=116.287/N3
554 S=S3*M6(J2)+S2*(1-M6(J2))
555 M9=1-M6(J2)
556 K7=EXP(-11272/(T(J2)+273.16)+17.374-.0462046*(T(J2)+273.16))
557 F2=M9*1.25893/(.69)^3
558 F1=(1-M9+M9*.69)^3/(1.25893^M9)
560 LET K8=EXP(W0+W1*(T(J2)+273.2)+W2/(T(J2)+273.2))
561 K9=K8*F1*(1-M9+F2*K7/K8)
563 D3=M6(J2)*.99704+(1-M6(J2))*1.10445
564 H6=M6(J2)*.998+(1-M6(J2))*1.004
565 Q=28591/D3/H6/L4(J2)
570 LET R=R1*(V*5093/V1(J2)/122850-1)
580 LET L=K/R
590 LET H=K9^.5/1000
600 LET N9=(L-(M8)*H)/S
620 LET P4(J2)=L/((M8)*H)
630 PRINT
690 LET A9=K*(R1+R)*V2(J2)/G1/R9/V/R
693 D4=K7*(-.0462046+11272/(T(J2)+273.16)^2)
694 D5=K8*(W1-W2/(T(J2)+273.16)^2)
695 D7=F1*(D5*(1-M9+F2*K7/K8)+F2*(D4-K7*D5/K8))
696 D9=D7/H/2000000
710 LET X1=H1+2*H2*T(J2)
720 LET S1=N1+2*N2*T(J2)
725 M5=S1*M6(J2)+(1-M6(J2))*116.287*669.2/N3/(T(J2)+273.16-133.98)^2
726 M4=M7*(X1+Y1)/547.48
727 A8=A2(J2)*(EXP(2.30259*A1(J2))-1)*P1(J2)/D3/H6*(H*M4+N9*M5+M8*D9)
728 A6=K*(R1+R)/G1/R9/V/R*V8(J2)
729 V3(J2)=A8*R*V*R9*G1/K/(R1+R)
730 D8(J2)=A8/(H*M4+N9*M5+M8*D9)
735 D6(J2)=A6/(H*M4+N9*M5+M8*D9)
740 B9=A9-(H*M4+N9*M5)*D8(J2)
745 B7=A9-(H*M4+N9*M5)*D6(J2)
750 Q9(J2)=Q*B9/(M8*D8(J2))
755 Q7(J2)=Q*B7/(M8*D6(J2))
760 Z8=F1*F2*K7*(-.0462046*(T(J2)+273.16)^2+11272)
770 H4(J2)=1.987/K9*((1-M9)*F1*K8*(W1*(T(J2)+273.16)^2-W2)+Z8)
780 H5(J2)=LOG(1-H4(J2)/Q)
```

```
810 PRINT
850 RETURN
860 OPEN #4 AS 'MULDAT.WCN' FOR WRITE
870 WRITE #4,.31915,.31897,304.8,122000,12.285,2149000
880 WRITE #4,224.33,5.305,-.0113,110.88,3.468
890 WRITE #4,22.97,.868,67.188,2.135,9.49E-03
900 WRITE #4,14.0896,-.03939,-10308
910 CLOSE #4
920 OPEN #4 AS 'MULDAT.WCN' FOR READ
930 READ #4,K,K4,V,R1,G1,R9
940 READ #4,H0,H1,H2,Y0,Y1
950 READ #4,Z0,Z1,N0,N1,N2
960 READ #4,W0,W1,W2
970 CLOSE #4
980 CANCEL 'MULDAT.WCN'
990 GOTO 510
1000 PRINT #5,'TEMP   LAMBDA   JUMP   STEP    TRUE JUMP TRUESTEP'
1001 PRINT #5,'ABQDKT.WES OF',D$
1010 FOR N4=1 TO J3
1020 PRINT #5,T(N4),L4(N4),V4(N4),V5(N4),V2(N4),V3(N4)
1030 NEXT N4
1040 PRINT
1050 PRINT #5,'TEMP  TC VOLT   MON VOLT  PURITY  LAMBDA   LASER SET'
1060 FOR N4=1 TO J3
1070 PRINT #5,T(N4),T8(N4),V1(N4),P4(N4),L4(N4),L5(N4)
1080 NEXT N4
1090 PRINT
1100 PRINT #5,'TEMP  LAMBDA   QUANT YIELD  LOG(QY)  DELTA H0 LOG(1-H0/E)'
1110 FOR N4=1 TO J3
1120 PRINT #5,T(N4),L4(N4),Q9(N4),LOG(Q9(N4))/2.303,H4(N4),H5(N4)/2.303
1130 NEXT N4
1140 PRINT #5,481
1150 PRINT #5,'TEMP    LAMBDA   T JUMP   SLOPE  MOL FR H    QUANT YIELD'
1160 FOR N4=1 TO J3
1170 PRINT #5,T(N4),L4(N4),D8(N4),M(N4),M6(N4),Q9(N4)
1180 NEXT N4
1183 PRINT #5,'FILE','ABS','TRAN POWER','NORMALIZATION'
1184 FOR N4=1 TO J3
1185 PRINT #5,N4,A1(N4),P1(N4),A2(N4)
1186 NEXT N4
1190 WRITE #3,LOG(Q9)/2.303,H5/2.303,M,D8,L4,T,H4,T8,V1,P4,L5,Q9,V4,V5,V2
1195 WRITE #3,V3,M6,A1,P1,A2
1197 IF T3=1 THEN GOTO 1215
1200 CLOSE #3
1201 T3=1
1202 V3=V8\D8=D6\Q9=Q7
1203 PRINT '2ND PASS'
1206 PRINT #5,'MHDDKT TO PRODUCE ',D$
1207 CANCEL D$
1209 OPEN #3 AS D$ FOR WRITE
1210 GOTO 1000
1215 CLOSE ALL
1216 CLOSE ALL
1220 STOP
1230 PRINT 'HOW MANY ELEMENTS IN THE ARRAYS?'
1240 INPUT J4
1250 DIM J6(J4),J7(3,J4),J8(3,J4),R(J4)
1260 READ #2,J6,J7,J8,R
1270 GOSUB 1810
1280 FOR I=1 TO J3
1290 LET V3(I)=J6(I)
1300 LET V2(I)=J7(1,I)
1310 LET M(I)=J8(1,I)
1320 NEXT I
1330 CLOSE #2
1340 RETURN
```

```
1350 PRINT 'WHICH FILES ALSO HAVE THIS VALUE?'
1360 PRINT 'AFTER LAST FILE, ENTER A NEGATIVE NUMBER'
1370 INPUT N6
1380 IF N6<0 THEN GOTO 1410
1390 LET N5(N6)=N5(N4)
1400 GOTO 1370
1410 RETURN
1420 PRINT 'FILE NO. ',N4
1430 IF T8(N4)>0 THEN GOTO 1500
1440 INPUT T8(N4)
1450 IF T8(N4)>0 THEN GOTO 1500
1460 LET T8(N4)=-T8(N4)
1470 LET N5=T8
1480 GOSUB 1350
1490 LET T8=N5
1500 LET T(N4)=(-38.6+SQR(38.6^2+.166*T8(N4)))/.083
1510 RETURN
1520 PRINT 'FILE NO. ',N4
1530 IF L5(N4)<>0 THEN GOTO 1710
1540 INPUT L5(N4)
1545 L4(N4)=0
1550 INPUT Q4
1560 IF L5(N4)>0 THEN GOTO 1610
1570 LET L5(N4)=-L5(N4)
1580 LET N5=L5
1590 GOSUB 1350
1600 LET L5=N5
1610 FOR I=N4 TO J3
1620 IF L5(I)=0 THEN GOTO 1700
1630 PRINT I
1640 IF L4(I)<>0 THEN GOTO 1700
1650 IF Q4<0 THEN GOTO 1680
1660 LET L4(I)=1/(40000/L5(I)-Q4*.4155)
1670 GOTO 1700
1680 LET L4(I)=1/(40000/L5(I)+Q4*.2914)
1690 IF N5(N4)=0 THEN LET I=J3
1700 NEXT I
1710 RETURN
1720 PRINT 'FILE NO. ',N4
1730 IF V1(N4)<>0 THEN GOTO 1800
1740 INPUT V1(N4)
1750 IF V1(N4)>0 THEN GOTO 1800
1760 LET V1(N4)=-V1(N4)
1770 LET N5=V1
1780 GOSUB 1350
1790 LET V1=N5
1800 RETURN
1810 PRINT 'FOR WHICH FILE DO YOU WISH TO CHANGE THE INITIAL CHANNEL?'
1820 INPUT P7
1830 IF P7=0 THEN GOTO 1900
1840 PRINT 'HOW MUCH DO YOU WISH TO SHIFT THE CHANNEL?'
1850 INPUT P6
1880 LET J7(1,P7)=EXP(LOG(J7(1,P7))+J8(1,P7)*P6*R(P7)/51.2)
1885 PRINT J7(1,P7),J8(1,P7),R(P7)
1890 GOTO 1810
1900 RETURN
1910 PRINT 'INPUT OUTPUT FILENAME'
1920 INPUT B$
1940 OPEN #3 AS B$ FOR WRITE
1950 RETURN
3400 PRINT 'WHAT FILE IS PREVIOUS OUTPUT IN?
3410 INPUT D$
3415 PRINT 'HOW MANY PTS/ARRAY IN PREVIOUS OUTPUT'
```

```
3416 DELETE L4,T,T8,V1,L5
3417 INPUT Z7
3418 DIM L4(Z7),T(Z7),T8(Z7),V1(Z7),L5(Z7)
3420 OPEN #1 AS D$ FOR READ
3430 READ #1,L4,L4,M,L4,L4,T,T8,T8,V1,L5,L5,V4,V4,V5,V2,V3,M6
3435 V8=V5/2
3440 CLOSE #1
3450 RETURN
```

APPENDIX C - RECDIS.WES

Program to calculate the recombination distance of $H_3O^+ + OH^-$ from the equilibrium relaxation rate.

A. Program comments

10	Open an output file for results
20-140	Input raw data
305	Open a file for hard copy output
460-480	Calculate the recombination distance
490	Form hard copy and output files for recombination distance results

B. Subroutine comments

500	calculate the recombination distance
860-	Initialize variables
1910	Open an output file
3400	Input raw data from a file previously created. The hydrogen mole fraction, relaxation rate, and temperature are needed for this program.

C. Definition of variables

D1	HDO mole fraction
D2	D_2O mole fraction
E1	dielectric constant, ε, for isotopic mixture
E2	dielectric constant for D_2O
E3	dielectric constant for H_2O
H3	H_2O mole fraction
H	theoretical concentration of L_3O^+, $[L_3O^+]$
K1	recombination rate
K7	K_w for D_2O as a function of temperature
K8	K_w for H_2O as a function of temperature
K9	K_w for water as a function of temperature and isotopic composition
M6	hydrogen mole fraction
M7	ionic conductivity of $H_3O^+ + OH^-$ at 25°C as a function of hydrogen mole fraction
M8	ionic conductivity of $H_3O^+ + OH^-$ as a function of temperature and hydrogen mole fraction
M9	deuterium mole fraction
S2	delta times sigma, $\Delta\sigma$ (see discussion)
S3	delta, $\Delta = Z_+ Z_- e^2/4\pi\varepsilon_o\varepsilon\sigma kT$
S4	recombination distance = σ, sigma
T2	temperature dependence of the ionic conductivity of $H_3O^+ + OH^-$ in H_2O
U1	diffusion coefficient of $H^+ + OH^-$

X2	hydronium ionic conductivity in H_2O
Y2	hydroxide ionic conductivity in H_2O

D. Program listing (see pages 240-241)

```
10 GOSUB 1910
20 PRINT 'ENTER NO OF FILES'
30 INPUT J3
40 DIM S4(J3),S3(J3),S2(J3),E1(J3),M8(J3),T(J3),M(J3)
50 DIM U1(J3),H(J3),M6(J3),K1(J3)
100 LET T=0\LET V2=0\LET V1=0\LET V3=0\LET M=0\LET L4=0
110 LET V4=0\LET V5=0\LET D8=0\LET P4=0\LET H4=0\LET Q9=0
130 LET H5=0\LET N5=0\LET V8=0\LET T8=0\LET L5=0
132 PRINT 'IF REANALYZING A PREVIOUSLY ANALYZED FILE, TYPE 1'
134 INPUT Z3
136 IF Z3=1 THEN GOSUB 3400
137 IF Z3=1 THEN GOTO 140
~~138 GOSUB 1230~~
140 PRINT
305 OPEN #5 AS 'MULDEC.WES' FOR WRITE
310 PRINT
460 FOR J2=1 TO J3
470 GOSUB 500
480 NEXT J2
490 GOTO 1000
500 IF J2=1 THEN GOTO 860
510 LET X2=H0+H1*T(J2)+H2*T(J2)*T(J2)
515 DELETE R
517 H3=M6(J2)^2
518 D1=2*M6(J2)-2*H3
519 D2=1-H3-D1
520 M7=H3*548.9+D1*411.2+D2*363.4
530 LET Y2=Y0+Y1*T(J2)
535 T2=(X2+Y2)/547.48
536 M8(J2)=M7*T2
555 M9=1-M6(J2)
556 K7=EXP(-11272/(T(J2)+273.16)+17.374-.0462046*(T(J2)+273.16))
557 F2=M9*1.25893/(.69)^3
558 F1=(1-M9+M9*.69)^3/(1.25893^M9)
560 LET K8=EXP(W0+W1*(T(J2)+273.2)+W2/(T(J2)+273.2))
561 K9=K8*F1*(1-M9+F2*K7/K8)
590 LET H(J2)=K9^.5/1000
600 K1(J2)=-1000000*M(J2)/2/H(J2)
610 U1(J2)=M8(J2)*8.930397E-10*(T(J2)+273.16)
620 E2=EXP(4.47335-4.6351E-03*T(J2))
630 E3=EXP(4.47632-4.58445E-C3*T(J2))
640 E1(J2)=M9*E2+(1-M9)*E3
650 S2(J2)=-1.6711E-03/(T(J2)+273.16)/E1(J2)
660 S3(J2)=LOG(S2(J2)*7.566698E+24*U1(J2)/K1(J2)+1)
670 S4(J2)=S2(J2)/S3(J2)
850 RETURN
860 OPEN #4 AS 'MULDAT.WCN' FOR WRITE
870 WRITE #4,.31915,.31897,304.8,122000,12.285,2149000
880 WRITE #4,224.33,5.305,-.0113,110.88,3.468
890 WRITE #4,22.97,.868,67.188,2.135,9.49E-03
900 WRITE #4,14.0896,-.03939,-10308
910 CLOSE #4
920 OPEN #4 AS 'MULDAT.WCN' FOR READ
930 READ #4,K,K4,V,R1,G1,R9
940 READ #4,H0,H1,H2,Y0,Y1
950 READ #4,Z0,Z1,N0,N1,N2
960 READ #4,W0,W1,W2
970 CLOSE #4
980 CANCEL 'MULDAT.WCN'
990 GOTO 510
1000 PRINT #5,'DIFF','MOLE','RECOMB','RELAX','K RECOMB','TEMP'
1010 PRINT #5,'COEFF','FRACTION H','DISTANCE','TIME','CM3/MOL',''
1020 PRINT #5
1025 FOR N4=1 TO J3
1030 PRINT #5,U1(N4),M6(N4),S4(N4),-1/M(N4),K1(N4),T(N4)
1040 NEXT N4
```

```
1050 PRINT #5,'DELTA =Z(H+)Z(OH-)E^2/4PIEPSILON(O)EPSILON K*T'
1060 PRINT #5,'SIGMA = REACTION DISTANCE'
1065 PRINT #5,'DELTA','DELTA SIGMA','EPSILON','MOB H2O','CONC H+'
1070 FOR N4=1 TO J3
1080 PRINT #5,S3(N4),S2(N4),E1(N4),M8(N4),H(N4)
1090 NEXT N4
1100 WRITE #3,U1,M6,S4,M,K1,T,S3,S2,E1,M8,H
1200 CLOSE ALL
1210 CLOSE ALL
1220 STOP
~~1230 READ #2,[illegible]~~
~~1240 CLOSE #2~~
~~1340 RETURN~~
1910 PRINT 'INPUT ~~INPUT AND~~ OUTPUT FILENAMES'
1920 INPUT ~~A$~~,B$
~~1930 OPEN #2 AS A$ FOR READ~~
1940 OPEN #3 AS B$ FOR WRITE
1950 RETURN
3400 PRINT 'WHAT FILE IS PREVIOUS OUTPUT IN?
3410 INPUT D$
3415 PRINT 'HOW MANY PTS/ARRAY IN PREVIOUS OUTPUT'
3416 DELETE M6,M,T
3417 INPUT Z7
3418 DIM M6(Z7),M(Z7),T(Z7)
3420 OPEN #1 AS D$ FOR READ
3430 READ #1,M6,M6,M,M,T,T
3440 CLOSE #1
3450 RETURN
```

APPENDIX D - Comments on non-statistical effects in overtone photochemistry

The introduction discusses several attempts to find non-statistical effects in gas phase overtone chemistry. However, a complete unified attempt to demonstrate non-statistical effects following overtone excitation has not been made. For the purposes of the discussion it is important to have a description of the process of overtone absorption (see McDonald).[1] Assume ϕ_s is a zero order anharmonic XH oscillator, local mode state and ϕ_ℓ are all the orthogonal molecular basis functions. In this basis set, ϕ_s has nearly all the overtone oscillator strength. These basis functions are not molecular eigenstates, but the molecular eigenstates, ϕ_n, can be expressed in terms of these basis functions. Or alternatively, ϕ_s can be expressed in terms of the molecular eigenstates. The oscillator strength of an eigenstate is approximately proportional to the square of the ϕ_s component of that eigenstate. The width of the eigenstate is given by the rate of collisions, radiation, dissociation and any other processes that remove population from the ϕ_s level.

It is possible that adjoining eigenstates have differing reaction rates. Classical trajectory studies of model potentials show that it is possible to have both stable, repetitive and random, stochastic trajectories in the same energy region.[2,3] If the same behavior exists for eigenstates of real molecules above the dissociation energy barrier, such qualitatively different trajectories may have qualitatively different dissociation rates and spectroscopic properties. Recent work by Heller[4] on Raman spectra gives a relationship between classical trajectories and spectroscopic properties. If the molecular state density is low enough, The precision of C.W. dye laser overtone excitation allows excitation of single eigenstates. So far all overtone chemistry experiments use broadband C.W. excitation. Thus, several eigenstates are probably excited simultaneously. As the laser is tuned, only the "average" behavior of the excited eigenstates in a spectral region is observed. If only a few eigenstates are not stochastic, then only narrow band excitation will detect non-stochastic behavior.

A second possible way to detect non-statistical behavior is a way first suggested by Moore and Smith.[5] They suggested that coherent picosecond excitation of vibrational overtones of reactants in a condensed phase might show non-statistical effects. This suggestion can be given a slightly more quantitative foundation in McDonald's "molecular eigenstates" framework. Assume the reaction rate of the excited state is proportional to the probability that it looks like a local X-H stretch. One might imagine this to be true if the projection of the excited X-H stretch on the reaction coordinate is large. McDonald shows us that if more than one eigenstate is coherently excited, an interference effect is present. The shorter the excitation pulse, the larger the bandwidth of coherently excited eigenstates. The initial constructive interference produces a larger initial X-H stretch probability and therefore a larger initial reaction rate. Thus, the rate at high pressure, where the initial reaction will dominate the total yield, will be higher than the low pressure rate where dissociation of the relaxed species dominates the yield. This could be the quantum mechanical explanation of the Chandler[6] overtone experiments,[7] and an analogous description almost certainly is the explanation fo the Rabinovitch[8] cyclopropane experiments.

1. J.D. McDonald, Ann. Rev. Phys. Chem. 30, 29 (1979)
2. S.A. Rice, Adv. Chem. Phys. 47, part 1, 117 (1981)
3. P. Brumer, Adv. Chem. Phys. 47, part 1, 201 (1981)
4. D.J. Tannor and E.J. Heller, J. Chem. Phys. 77, 202 (1982)
5. C.B. Moore and I.W.M. Smith, Faraday Disc. Chem. Soc. 67, 146 (1979)
6. D.W. Chandler, W.E. Farneth, and R.N. Zare, J. Chem. Phys. 77, 4447 (1982)
7. This assumes a C.W. dye laser can coherently excite more than one eigenstate. If the dye laser cannot, then the experimental result is surprising indeed. If eigenstates are incoherently, individually excited, there can be not time dependence in the dissociation rate.
8. J.D. Rynbrandt and B.S. Rabinovitch, J. Chem. Phys. 54, 2275 (19)

APPENDIX E - FURTHER WORK

This section suggests further work on aqueous systems, outlines how data from these systems can be analyzed, and suggests some completely new but related systems.

Aqueous Systems

Measuring quantum yields for liquid mixtures other than H_2O/D_2O mixtures could provide useful information. Potentially helpful references include 1 through 5. A mixture of H_2O and H_2O_2 can produce a "broken" link in a linear chain of H_2O molecules without too great a disruption of physical or of vibrational structure. A mixture of H_2O and alcohol, ROH, will alter mixture conductivities and perhaps provide an efficient relaxation path through the R group. Also, several solutes which do not hydrogen bond to the water can be tried, such as acetonitrile, acetone, or CBr_2F_2. The CBr_2F_2 has no high frequency modes that can couple to the OH stretch of the excited water.

Analysis of data from these systems cannot be done by the same method used for pure H_2O. Insufficient information is available in the literature. The number of photons absorbed by H_2O can be determined from the spectroscopy of the water/solute mixture and the transmitted laser intensity. If product ion conductivities are known, the number of reactive events can be determined from the portion the transient conductivity peak resulting from laser induced reaction. Product ion conductivities for a particular mixture can be determined with adequate accuracy from a conductivity bridge and solutions of KOH, HCl, and KCl. The portion of the conductivity peak caused by the laser induced reaction can be determined by subtracting a multiple of the thermal curve obtained by tuning the laser to a wavelength longer than about 1.3 μ where there is no laser induced reaction. The multiple is chosen so that the thermal baseline step is eliminated. Absolute yields can be determined by calibrating with pure H_2O.

Non-aqueous systems

Two non-aqueous systems would be interesting to try. The first is neat liquid ammonia. Liquid ammonia is a weakly dissociating, hydrogen bonded liquid similar to water. It would be interesting to know if liquid water is the only system which shows a laser induced reaction. (Preliminary experiments on neat MeOH showed no discernable conductivity peak.)

The other non-aqueous system is an entirely different class of condensed phase system that may avoid some of the disadvantages of the H_2O system. Proton transfer in acid-base pairs isolated in a Shpolskii matrix of n-paraffins[7] could be activated by overtone absorption.

Electronic spectra of dye molecules in an n-paraffin matrix at 20°K often show a sharp line spectra with about 1 cm^{-1} width instead of the usual braod band structure present in a liquid. Spectral analysis shows that a Shpolskii matrix possess a few inequivalent sites which do not interact strongly with the guest molecule. Since the fluorescence excitation spectra are sharp, both the ground and excited state must be sharp,[8,9] and it is reasonable to expect the overtone spectra to be sharp as well. Ideally, if a Shpolskii type of matrix can be made of per-halogenated oils, then any potential interference from host overtone absorption can be eliminated.

If acidic dye molecules are introduced with an excess of base, or if basic dye molecules are introduced with an excess of acid, it should be possible to form acid-base pairs in the low dielectric constant paraffins.[10] Thus, there will be two potential wells for the proton; one on the acid and one on the base. As the temperature is lowered, the proton should lie in the lowest well. Alternatively, a molecule such as methyl salicylate, with an intramolecule proton transfer, can be used. Many strongly fluorescing dye molecules show wavelength differences in an acidic versus a basic form.[9,10-13] These should be unambiguously resolved in the Shpolskii matrix and can thus serve as a probe of the relative concentration of the acidic and basic form of the dye.

The experiment is carried out by using a C.W. dye laser to probe the concentration of the highest enthalpy form of the dye molecule. Upon initial formation of the matrix, the low temperature ensures that most of the dye molecules are in the low enthalpy form. Very few high enthalpy molecules will be thermally excited and fluorescence will be weak or non-existant. A pulsed dye laser is used to excite overtones of the matrix isolated dye molecule. A fraction of the excited acid-base pairs can transfer a proton to produce the high enthalpy form if the photon energy of the pulsed dye laser is above the energy barrier. These molecules will absorb C.W. dye laser photons and fluoresce. The rise and fall of the fluorescence signal serves as a monitor of the time dependent concentration of the high enthalpy dye molecules.

The same sensitivity advantages obtained in the liquid water reaction by making a transient rather than a C.W. measurement are obtained, but fewer disadvantages are present.

The spectroscopy is unambiguous, absorption lines should be relatively sharp and assignable to specific hydrogens of the acid base pair just as in gas phase spectra. The lines should be narrower than in the gas phase because there is no rotational structure. Hydrogens in the acid, in the base, nearby, or far from the reactive proton may be selectively activated.

The system is closed in the sense that the reactive solute is a well defined entity separate from the weakly interacting solvent, in contrast to the water system. The number of modes present in both the acidic solute and basic solute are known. The number of modes in the non-dye molecule can be varied systematically.

The concentration of acid-base pairs or of other species added to quench the excitation can be varied and is known. The barrier height can be varied by changing the acidic or basic strength of the non-dye molecule.

The system potentially has very rapid time resolution. If two picosecond sources are used, a picosecond resolution, pulse-probe experiment can be performed. The time behavior is obtained simply by measuring total fluorescence as the time delay between the excitation pulse and probe pulse is changed. No expensive streak cameras are needed.

1. Covington and Dickinson, "Physical Chemistry of Organic Solvent Systems", London.
2. I.M. Kolthoff, Pure and Applied Chemistry 25, 305 (1971).
3. Hayd, Weidermann, and Zundel, J. Chem. Phys. 70, 86 (1979).
4. H.P. Fritz and W. Kornrumpf, J. Electroanal. Chem. 100, 217 (1979).
5. Modern Aspects of Electrochemistry, B.E. Conway and J. O'M. Bockris, eds., including V.3, p. 137
6. E. Grunwald and D. Eustace in "Proton Transfer Reactions", V. Gold and E.F. Caldin, eds., Chapman and Hall, London (1975).
7. E.V. Shpol'skii, Sov. Phys. Uspekhi 6, 411 (1963).
8. R.I. Personov and V.V. Solochmov, Opt. Spectrosc. 23, 317 (1967).
9. F.P. Schafer in "Dye Lasers", Topics in Applied Physics, v. 1, F.P. Schafer, ed., Springer-Verlag, New York (1973)
10. B.H. Robinson in reference 6.
11. K.H. Drexhage in reference 9.
12. D. Huppert, M. Gutman, and K.J. Kaufmann, Adv. Chem. Phys. 47, 643 (1981).
13. J.E. Crooks in "Comprehensive Chemical Kinetics", v. 8, C.H. Bamford and C.F.H. Tipper, eds., Elsevier (1977).

This report was done with support from the Department of Energy. Any conclusions or opinions expressed in this report represent solely those of the author(s) and not necessarily those of The Regents of the University of California, the Lawrence Berkeley Laboratory or the Department of Energy.

Reference to a company or product name does not imply approval or recommendation of the product by the University of California or the U.S. Department of Energy to the exclusion of others that may be suitable.

TECHNICAL INFORMATION DEPARTMENT
LAWRENCE BERKELEY LABORATORY
UNIVERSITY OF CALIFORNIA
BERKELEY, CALIFORNIA 94720